RIGA TECHNICAL UNIVERSITY

Sergejs Beļuns

BIO-INSPIRED WOOD MIMIC MATERIALS CREATED BY RECOMBINING CELLULOSE, HEMICELLULOSE AND LIGNIN

Doctoral Thesis

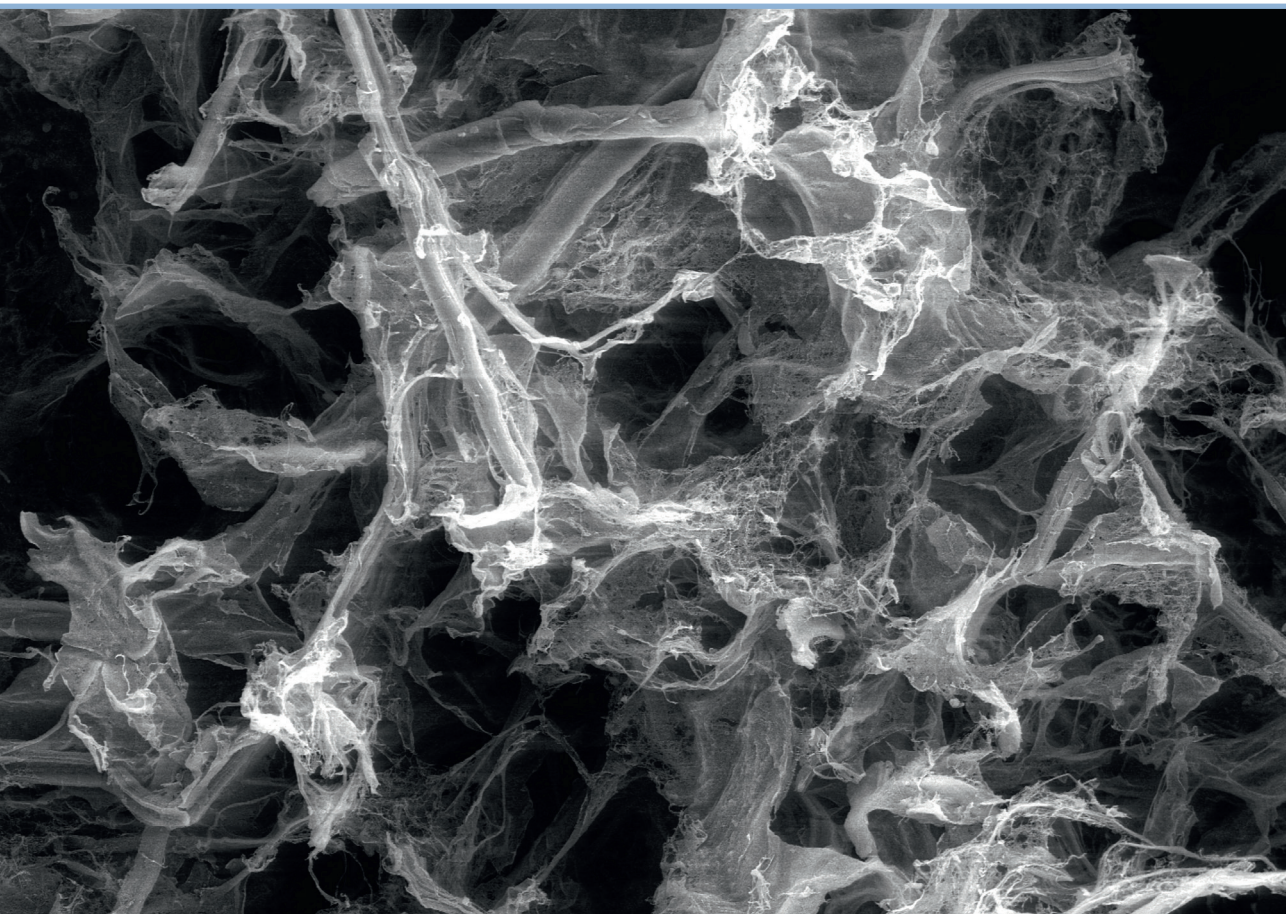

RTU Press
Riga 2024

RIGA TECHNICAL UNIVERSITY
Faculty of Natural Sciences and Technology
Institute of Chemistry and Chemical Technology

Sergejs Beļuns
Doctoral Student of the Study Programme "Chemistry, Materials Science and Engineering"

BIO-INSPIRED WOOD MIMIC MATERIALS CREATED BY RECOMBINING CELLULOSE, HEMICELLULOSE AND LIGNIN

Doctoral Thesis

Scientific supervisors
Professor Dr. sc. ing.
SERGEJS GAIDUKOVS
Professor Ph. D.
VIJAY KUMAR THAKUR

Riga 2024

Beļuns, S. Bio-inspired wood mimic materials created by recombining cellulose, hemicellulose and lignin. Doctoral Thesis. Riga: RTU Press, 2024. 139 p.

Published in accordance with the decision of the Promotion Council "P-02" of 19 February 2024, Minutes No. 04030-9.2.2/2.

Investigation, preparation, and testing of the materials was performed in the Institute of Chemistry and Chemical Technology of Riga Technical University.

This research was carried out within the scope of project roject RealHLC No. lzp-2019/1-0390, funded by the Latvian Council of Science.

This research has been supported by Riga Technical university doctoral grant programme.

This research has been supported by the European Social Fund within the Project No 8.2.2.0/20/I/008 Strengthening of PhD students and academic personnel of Riga Technical University and BA School of Business and Finance in the strategic fields of specialization of the Specific Objective 8.2.2 To Strengthen Academic Staff of Higher Education Institutions in Strategic Specialization Areas of the Operational Programme «Growth and Employment».

ACKNOWLEDGEMENTS

I wish to convey my heartfelt thanks to my family, whose constant love, support, and patience have been the bedrock of my journey.

My profound appreciation goes out to my supervisor, Sergejs Gaidukovs, for his unwavering guidance, encouragement, and patience he provided throughout this process. I also extend my genuine gratitude to all my colleagues, whose involvement and contributions have been invaluable. My special thanks and gratitude to my dear friend Oskars Platnieks for moral support and guidance. Additionally, I extend my thanks to the reviewers for their insightful critiques, recommendations, and direction.

I am deeply grateful to the Institute of Chemistry and Chemical Technology (Polymer Materials) at Riga Technical University, as well as the Latvian Council of Science and the European Social Fund, for all the opportunities provided to me during my doctoral studies.

"Pain was a fascinating horror."
/Aldous Huxley/

DOCTORAL THESIS PROPOSED TO RIGA TECHNICAL UNIVERSITY FOR THE PROMOTION TO THE SCIENTIFIC DEGREE OF DOCTOR OF SCIENCE

To be granted the scientific degree of Doctor of Science (Ph. D.), the present Doctoral Thesis has been submitted for the defence at the open meeting of RTU Promotion Council on 10 June 2024, at 10.00 at the Faculty of Natural Sciences and Technology of Riga Technical University, Paula Valdena iela 7, Room 272.

SCIENTIFIC SUPERVISORS

Professor Dr. sc. ing. Sergejs Gaidukovs
Faculty of Materials Science and Applied Chemistry, Riga Technical University, Latvia
Professor Ph. D. Vijay Kumar Thakur
Biorefining and Advanced Materials Research Center, SRUC, Barony Campus, Parkgate, United Kingdom

OFFICIAL REVIEWERS

Dr. sc. ing. Jānis Rižikovs
Latvian State Institute of Wood Chemistry, Latvia

Associate Professor Dr. Eero Kontturi
Aalto University, Finland

Associate Professor Dr. Darshil U.Shah
University of Cambridge, United Kingdom

DECLARATION OF ACADEMIC INTEGRITY

I hereby declare that the Doctoral Thesis submitted for the review to Riga Technical University for the promotion to the scientific degree of Doctor of Science (Ph. D.) is my own. I confirm that this Doctoral Thesis had not been submitted to any other university for the promotion to a scientific degree.

Sergejs Beļuns ……. (signature)
Date: ……

The Doctoral Thesis has been written in English. It consists of an Introduction; Literature review; Materials and methods; Results and discussion; Conclusions; 52 figures; 15 tables and the total number of pages is 139. The Bibliography contains 240 titles.

ANNOTATION

Keywords: nanocellulose, lignin, hemicellulose, biocomposites, sustainable materials, tensile properties.

This Doctoral thesis explores the creation of sustainable, lignocellulose-based materials from biomass fibers, focusing on the eco-friendly potential of cellulose in composite materials. Research concentrates on developing versatile nanocomposites and biomimetic materials, particularly wood-like composites made from lignocellulose, hemicellulose, and lignin, derived from various biomass sources, including wood and hemp byproducts.

Central to the thesis is the process of extracting and refining lignocellulose from various biomass sources like wood pulp, wood dust, and agricultural residues, notably hemp stalks. This lignocellulose is then combined with added hemicellulose and lignin in specific proportions to replicate the structural and mechanical properties of natural wood, exploring two main material preparation pathways: cellulose nanopapers and lightweight foams, using advanced techniques such as chemical modification and nanofibrillation.

Advancements within the thesis include the development of hemp-based bioplastics with modifiable properties through thermal crosslinking, as well as an evaluation of their water resistance capabilities. The research culminates in the assessment of nanocellulose foams derived from wood and hemp, focusing on their mechanical, thermal and absorption properties for potential application in industrial contexts.

Overall, the dissertation contributes to sustainable materials science, demonstrating the advantageous performance and environmental benefits associated with using cellulosic nanomaterials and bioplastics produced from naturally occurring waste products.

The Doctoral Theses has been written in English; it consists of 139 pages, 52 figures, 15 tables and 240 reference sources.

ANOTĀCIJA

BIOIEDVESMOTI KOKSNI ATDARINOŠI MATERIĀLI, REKOMBINĒJOT CELULOZI, HEMICELULOZI UN LIGNĪNU

Atslēgas vārdi: nanoceluloze, lignīns, hemiceluloze, biokompozīti, ilgtspējīgi materiāli, stiepes īpašības.

Promocijas darbs izpēta ilgtspējīgu lignocelulozes bāzes kompozītmateriālu izveidi no biomasas šķiedrām, koncentrējoties uz celulozes videi draudzīgo potenciālu kompozītmateriālos. Pētījums koncentrējas uz daudzpusīgu nanokompozītu un biomimētisku materiālu izstrādi, īpaši kokam līdzīgu kompozītu izveidi no lignocelulozes, hemicelulozes un lignīna, kas iegūti no dažādiem biomasas avotiem, tostarp koka un kaņepju blakusproduktiem.

Promocijas darba galvenais mērķis ir lignocelulozes ekstrakcijas un attīrīšanas process no dažādiem biomasas avotiem, piemēram, koksnes celulozes, koksnes putekļiem un lauksaimniecības atliekām, īpaši kaņepju kātiem. Pēc tam šī celuloze tiek apvienota ar hemicelulozi un lignīnu noteiktās proporcijās, lai atkārtotu dabiskā koka strukturālās un mehāniskās īpašības, pētot divus galvenos materiālu sagatavošanas veidus: celulozes nanopapīrus un vieglas putas, izmantojot progresīvas metodes, piemēram, ķīmisko modifikāciju un nanofibrilāciju.

Disertācijā panāktie uzlabojumi ietver kaņepju bāzes bioplastmasas attīstību ar maināmām īpašībām caur termisko saistīšanu, kā arī to ūdens izturības spēju novērtēšanu. Pētījums kulminējas ar no koka un kaņepēm iegūto nanolignocelulozes putu novērtējumu, koncentrējoties uz to mehāniskajām un termiskajām īpašībām.

Kopumā promocijas darbs sniedz ieguldījumu ilgtspējīgas materiālu zinātnes jomā, demonstrējot izdevīgo veiktspēju un ieguvumus videi, kas saistīti ar celulozes nanomateriālu un bioplastmasas izmantošanu, kas ražota no dabiski sastopamiem atkritumiem vai izejvielām.

Promocijas darbs ir uzrakstīts angļu valodā, tas sastāv no 139 lappusēm, 52 attēliem, 15 tabulām un 240 informācijas un literatūras avotiem.

TABLE OF CONTENTS

ABBREVIATIONS 9
INTRODUCTION 10
Aim of the Doctoral Thesis 13
Tasks of the Doctoral Thesis 13
Thesis statements to be defended 13
Scientific novelty 13
Practical significance 14
Approbation of the PhD Thesis in Scopus and Web of Science indexed articles 14
Other publications on the topic that are not included in the Thesis 15
Dissemination in international scientific conferences 15
1. LITERATURE REVIEW 17
1.1. Sustainable synergies: the role of biopolymers in functional material innovation 17
1.2. Cellulose and Nanofibrillated cellulose (NFC) 18
1.3. Cellulose – a new approach 20
1.4. Cellulose – Lignin interaction 20
1.5. Cellulose – Hemicellulose interaction 22
1.6. Cellulose – Pectin interaction 23
1.7. Cellulose – Starch interaction 24
1.8. Processing biopolymers into functional materials 25
2. MATERIALS AND METHODS 27
2.1. Materials 27
2.2. Testing methods 33
3. RESULTS AND DISCUSSION 39
3.1. Clean manufacturing of cellulose nanopapers by incorporating lignin and xylan as sustainable additives 39
3.1.1. Morphological properties 39
3.1.2. Tensile properties 40
3.1.3. Thermooxidative stability 45
3.1.4. Thermal conductivity 47
3.1.5. Summary 50
3.2. Lignin and xylan as interface engineering additives for improved environmental durability of sustainable cellulose nanopapers 51
3.2.1. UV irradiation and heat effect on the tensile properties 51
3.2.2. Structural analysis 55
3.2.3. UV-VIS and FTIR spectroscopy 58
3.2.4. Moisture effect on the tensile properties 62
3.2.5. Nanopaper performance quality analysis 66
3.2.6. Summary 69
3.3. Sustainable hemp-based bioplastics with tunable properties via reversible thermal crosslinking of cellulose 70

3.3.1. Thermal stability and crosslinking characterization 70
3.3.2. Structure and morphology 74
3.3.3. Tensile properties and water uptake 75
3.3.4. Dielectric properties 78
3.3.5. Depolymerization and recycling 79
3.3.6. Implications 80
3.3.7. Summary 81
3.4. From wood and hemp biomass wastes to sustainable nanocellulose foams 83
3.4.1. Structural characterization 83
3.4.2. Fourier transform infrared spectroscopy (FTIR) 84
3.4.3. X-ray diffraction (XRD) analyses 85
3.4.4. Thermal analysis 86
3.4.5. Foam material morphology characterization 87
3.4.6. Compression properties 89
3.4.7. Thermal conductivity properties 91
3.4.8. Summary 93
3.5. Sustainable Foams from Hemp, Lignin, Xylan, Pectin, and Glycerol: Tunable via Reversible Citric Acid Crosslinking for Absorption and Insulation Applications 94
3.5.1. Chemical interactions 94
3.5.2 Morphology 95
3.5.3. Mechanical performance 97
3.5.4. Absorption characterization 101
3.5.5. Thermal conductivity 105
3.5.6. Summary 105
CONCLUSIONS 107
REFERENCES 108
Supplementary 125
Supplementary 1 126
Supplementary 2 127
Supplementary 3 128
Supplementary 4 129
Supplementary 5 130
Supplementary 6 131
Supplementary 7 132
Supplementary 8 133
Supplementary 9 134
Supplementary 10 135
Supplementary 11 136
Supplementary 12 137
Supplementary 13 138
Supplementary 14 139

ABBREVIATIONS

CA	Citric acid
CI	Crystallinity index
CMC	Carboxymethyl cellulose
CNC	Cellulose nanocrystals
CNF	Cellulose nanofibers
CNP	Cellulose nanopaper
DI	Deionized water
DMAc	Dimethylacetamide
FESEM	Field emission scanning electron microscopy
FFD	Full-factorial design
FTIR	Fourier Transform Infrared Spectroscopy
G	Glycerol
H	Hemp
HPLC	High purity liquid chromatography
L	Lignin
MCC	Microcrystalline cellulose
NCC	Nanocrystalline cellulose
NC	Nanocellulose
NFC	Nanofibrillated Cellulose
NP	Nanopaper
P	Pectin
PEG	Polyethylene glycol
RH	Relative humidity
SEM	Scanning Electron Microscopy
STEM	Scanning transmission electron microscopy
TGA	Thermogravimetric Analysis
UV-vis	Ultraviolet-visible light
WAXD	Wide angle X-ray diffraction
WM	Wood mimic
wt%	Weight percent
X	Xylan

INTRODUCTION

In recent years, there has been an increase in the demand for sustainable materials, with significant innovation in the field of composite materials integrating renewable biomass fiber. Cellulose, a biopolymer derived from plant fibres, is at the forefront of this development due to its biodegradability, renewability, and nanoscale manufacturability. These characteristics make it an attractive candidate for reinforced materials, offering high strength-to-weight ratios suitable for various applications.

Research into nanocomposites utilizing nanocellulose has shown promising versatility, yielding advanced materials for use in hybrid composites, films, and foams. Furthermore, there's a notable emphasis on biomimetic materials in the pursuit of eco-friendly alternatives. Wood-like composites, primarily composed of cellulose, hemicellulose, and lignin, are gaining attention for their sustainability, as these abundant biopolymers are found in plant cell walls and offer a compelling source for environmentally friendly composite materials.

This Doctoral Thesis focuses on the extraction and alteration of nanocellulose and nanolignocellulose from various biomass sources, such as wood pulp, wood dust and agricultural residues (hemp stalks) and the use of external hemicellulose (xylan), and lignin. It should be noted that nanocellulose and nanolignocellulose differ only in the content of cellulose in nanofibers, which can be regulated by chemical treatment; and in the following work they will be denoted by the abbreviation NFC, which is an abbreviation of the widely used English term nanofibrillated cellulose (NFC). Subsequently, these biopolymers are combined in controlled ratios to create composites that mimic natural wood's structural and mechanical properties. Two distinct material preparation routes were explored: the preparation of wood mimic composite thin films (nanopapers) and the preparation of lightweight foams. The fabrication process often involved advanced techniques like chemical modification, nanofibrillation, and blending with other biodegradable polymers.

In the initial phase, nanofibrillated cellulose was derived from an unused laboratory filter paper, leading to the preparation of cellulose nanopapers. In this stage the impact of hybrid modifiers was examined, specifically various combinations of lignin and xylan, on the performance of the cellulose nanopapers. These modifiers' role in structuring the NFC networks was fine-tuned by leveraging the distinct interaction mechanisms associated with lignin and xylan. Mathematical models formulated from experimental data were employed to characterize the potential of the composite materials with hybrid compositions.

Then, the first phase of research focused on evaluating how simulated environmental conditions — namely UV radiation, heat, and humidity — affect the tensile properties of cellulose nanopaper composites. This is relevant because cellulose-based materials and products are often susceptible to degradation from environmental factors like light, temperature, and moisture. Using UV-Vis and Fourier transform infrared spectroscopy (FTIR), the oxidation processes of the nanopaper interfaces were analyzed, revealing that while lignin and xylan experienced degradation, the cellulose fibres' structure remained largely intact. Additionally, scanning electron microscopy provided detailed images of the interface structure, enhancing

the understanding of how UV aging influences both the surface and the depth of penetration in the composites' cross-sections.

In the second phase, the study sought to augment the functionality of the composites by developing sustainable, hemp-based bioplastics with properties that could be adjusted through reversible thermal crosslinking of cellulose. Hemp stalks were processed into cast papers through purely mechanical methods, avoiding the need for chemical alterations or pre-treatments. These papers were then impregnated with a crosslinking blend containing glycerol, xylan, citric acid, and the plasticizer polyethylene glycol (PEG). Thermal crosslinking was efficiently achieved via a single-step reaction, where the materials were cured at 140°C. This process allowed for a considerable degree of tunability in the bioplastics' properties, which could be varied from brittle to ductile by altering the ratios of the components. The resulting bioplastics underwent comprehensive testing to evaluate their resistance to water and their capacity for water absorption.

In the third phase, sustainable lightweight nanolignocellulose foams were prepared from birch wood dust and hemp stalk waste. The lignocellulosic nanomaterials derived from these under-utilized waste residues and byproducts also serve as promising natural precursors for advanced applications, e.g., biomedical, pollution filtering, and thermal insulation. The wood and hemp fibrils were prepared by microfluidic processing of 0.2 – 1.0 wt% cellulose water suspensions. After freeze-drying, the resulting foam materials were characterized with a bulk density of 2 – 36 mg/cc. Key characteristics of the obtained nanocellulose foams were examined by the mechanical response, porosity, thermal conductivity, thermal degradation, chemical composition, and morphology.

In the fourth and final phase, the research explored further functionalization and the creation of sustainable, multifunctional foams using hemp stalk waste and other materials like lignin, xylan, pectin, glycerol, and citric acid. Utilizing freeze-drying and industrial waste products, the research aimed for an eco-friendly, scalable approach, resulting in 25 different foam formulations. These were methodically examined, focusing on citric acid, pectin, and glycerol roles. The foams displayed varying microstructures and densities, with high porosity and impressive absorption capacities for water, rapeseed oil, and kerosine. Most formulations maintained their absorption capacity after repeated cycles. Adding glycerol enhanced the foam's hydrophobicity, demonstrated by water contact angles of 140°-150°. Their thermal conductivity values were low, indicating good insulation properties. Mechanical testing showed their adaptable structure, ranging from soft to rigid. These foams have a wide range of applications, including thermal insulation, filtration, and environmental cleanup. The overall structure of the research is presented in Figure 1.1.

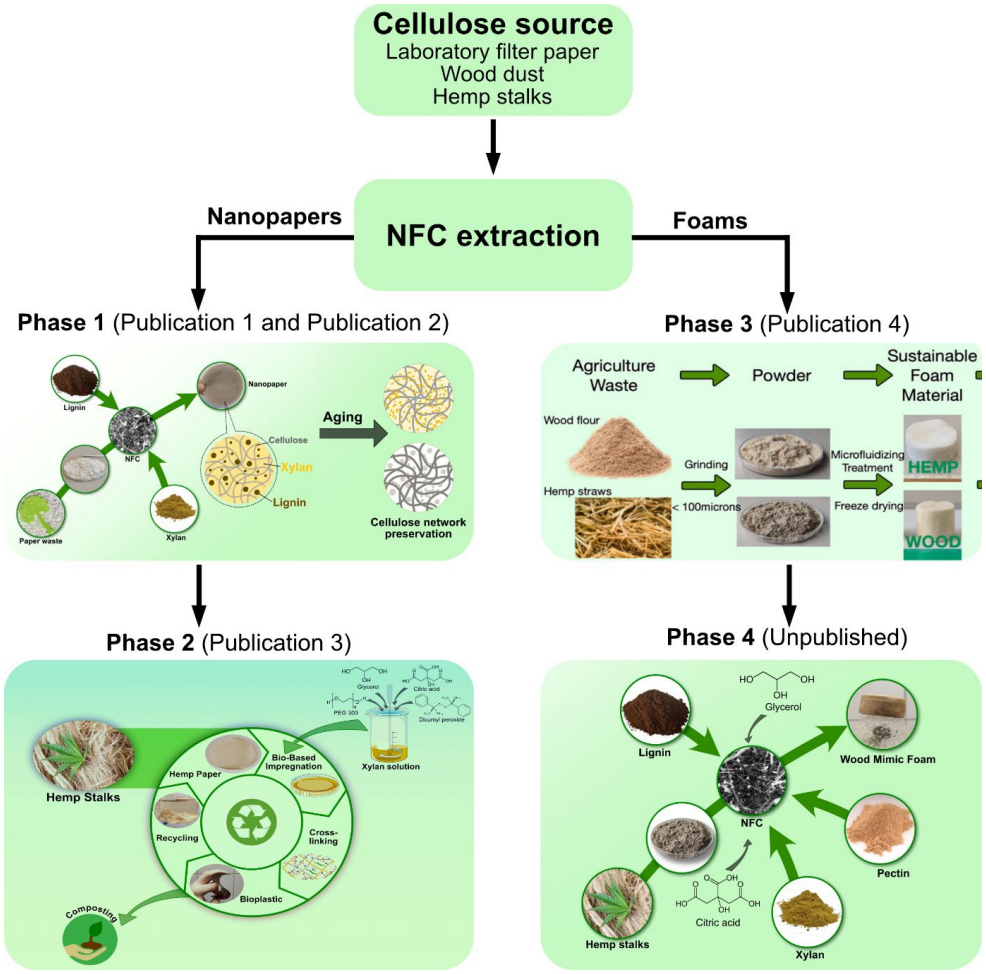

Figure 1.1. Structure of the research [original artwork].

Aim of the Doctoral Thesis

The main aim is to prepare and investigate systematically advanced biopolymer materials using renewable raw materials of nanolignocellulose, hemicellulose, and lignin extracted from biomass waste – through a strategy of their recombination and reassembly and also the introduction of additional green chemistry routes of components functionalization and crosslinking to adjust circularity and performance properties of the resulting wood-imitating materials as films and foams.

Tasks of the Doctoral Thesis

1. To extract nanolignocellulose from different sources of biomass waste with the microfluidization method.
2. To develop green chemistry methods of nanolignocellulose functionalization with biopolymers and crosslinking to tune up the structure and properties of obtained bioplastics.
3. To develop nanolignocellulose papers, bioplastic films, and bio-foams (sponges) inspired by wood structures that can potentially replace fossil-based ones.
4. To validate the performance and structure relationship of obtained lignocellulosic bioplastic materials.

Thesis statements to be defended

1. Nanolignocellulose extracted and manipulated from hemp and birch wood biomass can be recombined with hemicellulose and lignin and processed into wood-mimicking biopolymer papers, films, and foams (sponges).
2. The structure of nanocellulose papers and bio-foams can be regulated by adjusting the content of lignin and hemicellulose and also by green chemical functionalization and physical crosslinking.
3. The varying ratios of xylan, lignin, and nanolignocellulose components and the content of citric acid crosslinking agents and dicumyl peroxide initiator can systematically fine-tune the performance, biodegradation, and circularity of the film bioplastics.
4. The bio-foams (sponges) show tuneable structures ranging from soft to rigid behaviour and their applicability in thermal insulation, filtration systems, and environmental clean-up, among other potential uses.

Scientific novelty

The novel wood-mimicking lignocellulose contains biopolymer materials such as foams, films, and paper with regulated structure and adjustable performance properties. The developed

100 % biomaterials have very wide applications in the production of various packaging, coatings, sorbents, and building materials to replace fossil-origin plastics.

Practical significance

1. Transforming waste from agriculture and paper waste materials (with pretreatment) into valuable composites demonstrates a sustainable approach to resource utilization.
2. Developing wood-like composites can produce lighter, high-performance materials for use across various industries.
3. Adjustable hemp-based bioplastics create a flexible, eco-friendly alternative to traditional plastics.
4. The production of lignocellulose foams offers a green substitute for conventional insulating or packaging materials.

Approbation of the PhD Thesis in Scopus and Web of Science indexed articles

Literature review

1. Platnieks, O., **Beluns, S.**, Briede, S., Jurinovs, M., Gaidukovs, S. Cellulose synergetic interactions with biopolymers: Functionalization for sustainable and green material design (2023), Industrial Crops and Products, 204, 117310. DOI: 10.1016/j.indcrop.2023.117310.
   Chapter 3.1.
2. **Beluns, S.**, Gaidukovs, S., Platnieks, O., Barkane, A., Gaidukova, G., Grase, L., Nabels-Sneiders, M., Kovalovs, A., Thakur, V.K. Clean manufacturing of cellulose nanopapers by incorporating lignin and xylan as sustainable additives (2022), Carbohydrate Polymer Technologies and Applications, 3, 00207. DOI: 10.1016/j.carpta.2022.100207.
   Chapter 3.2.
3. **Beluns, S.**, Platnieks, O., Gaidukovs, S., Starkova, O., Sabalina, A., Grase, L., Thakur, V.K., Gaidukova, G. Lignin and xylan as interface engineering additives for improved environmental durability of sustainable cellulose nanopapers (2021), International Journal of Molecular Sciences, 22 (23), 2939**.** DOI: 10.3390/ijms222312939.
   Chapter 3.3.
4. **Beluns, S.**, Gaidukovs, S., Platnieks, O., Grase, L., Gaidukova, G., Thakur, V.K. Sustainable hemp-based bioplastics with tunable properties via reversible thermal crosslinking of cellulose (2023), International Journal of Biological Macromolecules, 242, 125055. DOI: 10.1016/j.ijbiomac.2023.125055.
   Chapter 3.4.
5. **Beluns, S.**, Gaidukovs, S., Platnieks, O., Gaidukova, G., Mierina, I., Grase, L., Starkova, O., Brazdausks, P., Thakur, V.K. From wood and hemp biomass wastes to sustainable nanocellulose foams (2021), Industrial Crops and Products, 170, 113780. DOI: 10.1016/j.indcrop.2021.113780.

Chapter 3.5.

6. **Beluns, S.**, Platnieks, O., Jurinovs, M., Buss, R., Gaidukovs, S., Orlova, L., Starkova, O., Thakur, V.K. Sustainable Foams from Hemp, Lignin, Xylan, Pectin, and Glycerol: Tunable via Reversible Citric Acid Crosslinking for Absorption and Insulation Applications (2024), Giant, (accepted).

Other publications on the topic that are not included in the Thesis

1. **Beluns, S.**, Platnieks, O., Sevcenko, J., Jure, M., Gaidukova, G., Grase, L., Gaidukovs, S. Sustainable Wax Coatings Made from Pine Needle Extraction Waste for Nanopaper Hydrophobization (2022), Membranes, 12 (5), 537. DOI: 10.3390/membranes12050537.
2. Budtova, T., Aguilera, D.A., **Beluns, S.**, Berglund, L., Chartier, C., Espinosa, E., Gaidukovs, S., Klimek-kopyra, A., Kmita, A., Lachowicz, D., Liebner, F., Platnieks, O., Rodríguez, A., Navarro, L.K.T., Zou, F., Buwalda, S.J. Biorefinery approach for aerogels (2020), Polymers, 12 (12), 2779, pp. 1-63. DOI: 10.3390/polym12122779.

Dissemination in international scientific conferences

1. **Beluns, S.**, Gaidukovs, S. Lignocellulose based aerogel preparation from wood and hemp waste materials. No: RTU 61st International Scientific Conference "Materials Science and Applied Chemistry 2020". Latvia, Riga, October 23, 2020. Online, Oral presentation.
2. **Beluns, S.**, Gaidukovs, S. Biobased low density and high porosity lignocellulose composite materials from wood and hemp waste. Functional Materials and Nanotechnologies FM&NT-2020. Lithuania, Vilnius, November 23-26, 2020. Online, Poster.
3. **Beluns, S.**, Gaidukovs, S. Xylan/Lignin modified biocomposites from lignocellulose waste. 1st Greenering international conference. Portugal, Costa da Caparica, February 15-16, 2021. Online, Poster.
4. **Beluns, S.**, Gaidukovs, S. Sustainable ultralight and completely biobased lignocellulose foams from waste cellulosic nanomaterials. Training school “Advanced Technologies for the processing and characterization of nanostructured materials”. July 5-6, 2021. Online, Oral presentation.
5. **Beluns, S.**, Gaidukovs, S. Sustainable ultralight foams from wood and hemp waste cellulosic nanomaterials for thermal insulation applications. Conference: Aerogel Industry-Academia Forum. July 13-15, 2021. Online, Poster.
6. **Beluns, S.**, Gaidukovs, S. Biobased lignocellulose composite cryogels from hemp waste. 7th International Polysaccharide Conference. France, Nantes, October 11-15, 2021. Poster.
7. **Beluns, S.**, Gaidukovs, S., Platnieks, O., Barkane, A. Lignin and Xylan addition to cellulose nanopaper - a sustainable solution to improve properties. No: RTU 62nd

International Scientific Conference "Materials Science and Applied Chemistry 2021". Latvia, Riga, October 22, 2021. Online, Oral presentation.

8. **Beluns, S.**, Gaidukovs, S. From hemp stalk waste to porous wood-mimic foams. 5th EPNOE Junior Scientist Meeting 2022. Portugal, Aveiro, September 8-9, 2022. Poster.
9. **Beluns, S.**, Gaidukovs, S. Ultralightweight biobased foams from hemp stalk waste with tunable mechanical properties and shape recovery effect. 7th International Conference on Multifunctional, Hybrid and Nanomaterials. Italy, Girona, October 19-22, 2022. Poster.
10. **Beluns, S.**, Gaidukovs, S., Paltnieks, O. Thermally crosslinked Hemp-based cellulose bioplastics with tunable properties and reversible reaction. Nordic Polymer Days 2023. Denmark, Kopenhagen, May 8-10, 2023. Poster.
11. **Beluns, S.**, Gaidukovs, S., Paltnieks, O. Thermally crosslinked cellulose bioplastics derived from hemp with tunable properties and reversible reaction. Renewable Resources & Biorefineries RRB 2023. Latvia, Riga, May 31 – June 2, 2023. Poster.
12. **Beluns, S.**, Gaidukovs, S. Wood mimic composites from cellulose, hemicellulose and lignin. No: RTU 64th International Scientific Conference "Materials Science and Applied Chemistry 2023". Latvia, Riga, October 6, 2023. Oral presentation.

1. LITERATURE REVIEW

1.1. Sustainable synergies: the role of biopolymers in functional material innovation

Biopolymers are slowly transitioning to become the critical raw materials of the modern economy [1,2]. This occurs as we approach the inevitable limits of fossil resources and tackle the reliance built upon them. Resource and energy production efficiency are two significant issues facing the global economy. This marks the modern approach, i.e., extracting more value from waste and byproducts and the formation of efficient recycling routes as means to recover energy and time inputs used in biological and chemical production systems [2,3]. In addition, half a century of extensive use of fossil-based polymers has left a tremendous amount of non-biodegradable pollution. In contrast, extensive use of chemical processing has led to toxic chemicals accumulating in the environment [4]. For these reasons and more, biopolymers, as a renewable, non-toxic, and biodegradable source of materials, have become the focus of modern material science and chemical engineering. Recent trends in various materials like hydrogels [5,6], aerogels [7,8], films [9,10], and fibers [11,12] show an increasing number of works focused on biopolymer-centered systems.

The abundant natural biopolymers can be divided into three large groups: polysaccharides, polyphenols, and proteins. The availability of various crop polysaccharides and lignin as the most prominent representative of polyphenols has seen an increasing number of researchers exploring these relatively cheap and renewable biomass wastes [13]. The transformation of raw material harvesting requires approaching the crops as multipurpose plants where every section sees the application. Similarly, the isolated material concept has been slowly phased out with the requirement for more advanced functional materials. More research has been dedicated to bottom-up processes and understanding various biopolymer roles and their synergetic interactions in living organisms [14]. This approach coincides with the rapidly growing popularity of bacterial cellulose and nanocellulose applications in material preparation [15,16]. Biopolymers are more complex than their synthetic counterparts. Still, with advancements in the computing power of modeling, nanotechnology, and even artificial intelligence, our understanding of molecular interactions and hierarchical assembly is growing rapidly. Studies that analyze biopolymer interfacial interactions [17] and create optimal routes for assembly methods of biopolymer networks [18] are increasing annually.

The conceptual approach for this review explores the mutualistic synergy of biopolymers reproduced in synthetic systems for advanced and functional material applications. As such, the discussion is organized with an emphasis on known literature and explores synergies between cellulose and various plant-based biopolymers, i.e., lignin, hemicellulose, pectin, and starch. Figure 1.2 shows schematic representations of some reviewed interactions. Discussion transitions provide the perspective of these synergetic interactions for novel functionalities and properties in physically or chemically crosslinked biopolymer networks.

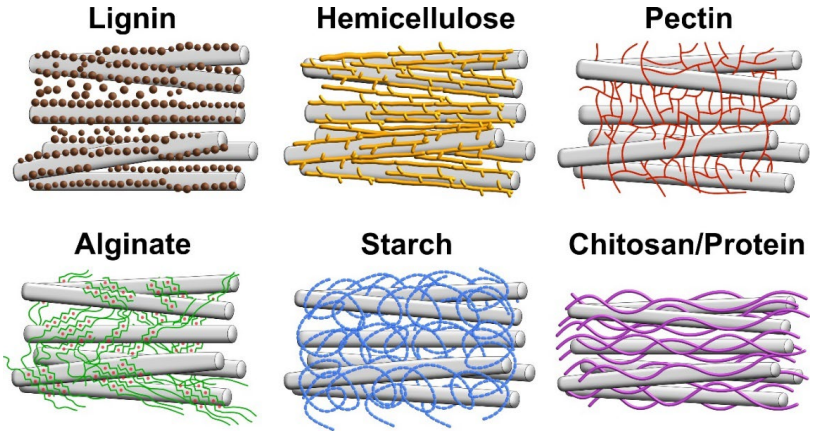

Figure 1.2. Schematic representation of cellulose interactions with various biopolymers [original artwork].

1.2. Cellulose and Nanofibrillated cellulose (NFC)

Cellulose, the most abundant natural biopolymer on Earth, can be found in a wide array of living organisms, including plants, animals, and certain bacteria [19]. It serves as the fundamental building block in the structural framework of plants and is gaining renewed attention as a sustainable alternative to petroleum-based products [20]. Regardless of its origin, cellulose consists of straight chains of sugars comprised of β-D-glucopyranose units linked by β-1–4-linkages, and its fundamental structure is a two-unit glucose molecule referred to as cellobiose.

The term "Nanocellulose" describes cellulosic materials with at least one dimension on the nanometer scale, and it can be derived from various lignocellulosic sources using diverse methods. Cellulose nanofibers have attracted significant interest due to their minimal thermal expansion [21], impressive length-to-diameter ratio [22], and capacity to enhance strength, alongside remarkable mechanical and optical properties. These properties make them highly versatile and applicable in various fields, including nanocomposites, paper production, coatings, security papers, food packaging, and gas barriers [23].

The generation of cellulose fibers at the nanoscale can be achieved through mechanical processes, such as homogenization. While other mechanical techniques can also be employed, the downside of many of these methods is their substantial energy consumption, particularly when multiple cycles are needed for further defibrillation [24]. To address these energy concerns, scientists have adopted a combination of mechanical pretreatments like refining and cryocrushing [25], biological methods involving the use of enzymes [26], and chemical approaches such as alkaline treatments and oxidation [27]. These combined methods aim to reduce fiber size before homogenization, subsequently decreasing energy consumption.

Nanofibrillated Cellulose (NFC), which represents the smallest structural component of plant fibers, is essentially an assembly of elongated cellulose molecular chains [28]. These

chains are composed of long, flexible, and interwoven cellulose nanofibers primarily derived from individual cellulose microfibrils, with side dimensions ranging from 10 to 100 nm [23]. Typically, their length is measured in micrometers, exhibiting a combination of crystalline and amorphous regions [29]. NFC is obtained by separating wood pulp using mechanical force, either before or after undergoing a chemical or enzymatic process [27].

Defibrillating NFC necessitates rigorous mechanical methods, although chemical pretreatments are often applied before mechanical fibrillation depending on the extent of processing and the source material. It's important to note that appropriate pretreatments of cellulose fibers improve the exposure of hydroxyl groups, expand the internal surface area, modify crystallinity, disrupt cellulose hydrogen bonds, and ultimately enhance the reactivity of the fibers [23]. Mechanical techniques to reduce cellulose fibers to nanofibers include refining and homogenizing, microfluidization, grinding, cryocrushing, and high-powered ultrasonication [19,28,29]. An overview of fibrillated cellulose is presented in Figure 1.3.

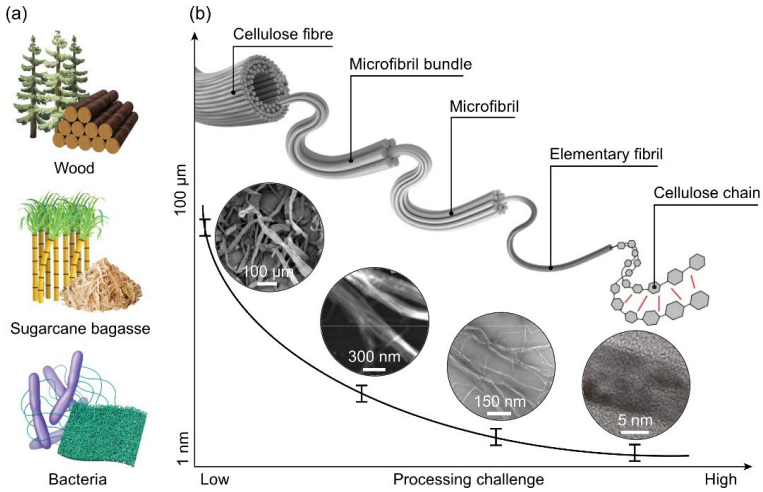

Figure 1.3. An outline of fibrillated cellulose. (a) Several common sources of fibrillated cellulose. (b) Schematic description of the hierarchical structure and manufacturing challenge of fibrillated cellulose [30].

NFC possesses a unique combination of properties, including a high surface area, impressive mechanical strength, flexibility, and the ability to form a dense network structure [31]. Its nano-scale dimensions and high aspect ratio contribute to superior mechanical and barrier properties compared to bulk cellulose [22]. Despite its promising applications, NFC does face specific challenges, such as scaling up production, ensuring uniformity in NFC properties, and integrating it into existing manufacturing processes. Ongoing research is dedicated to developing green and energy-efficient methods for NFC production and expanding its range of applications. From its origins as the primary structural component of plant cell walls, cellulose, particularly in its nanofibrillated form, is reshaping the landscape of material science and technology. The multifunctional properties of NFC are driving innovations across various sectors.

1.3. Cellulose – a new approach

While cellulose is a versatile and abundant natural polymer, relying solely on its utilization may not be sufficient to meet the diverse requirements of modern applications. There are several reasons why relying exclusively on cellulose is insufficient; thus, we emphasize the importance of blending and functionalizing cellulose with other biopolymers.

Cellulose exhibits certain limitations in terms of its inherent properties. For example, cellulose has relatively poor solubility, which can restrict its processability and limit its applications in certain industries [32]. Additionally, cellulose has moderate mechanical strength and thermal stability, which may not be suitable for demanding applications requiring exceptional performance [33]. Chemical modifications of cellulose often require elaborate procedures, specialized equipment, and substantial amounts of energy and reagents, which can increase the overall production costs [34]. Moreover, some methods lead to environmental concerns due to the generation of waste byproducts and the use of potentially hazardous chemicals [35]. This leads to an alteration of cellulose's natural biodegradability and biocompatibility [36].

The use of additives or blending mixtures can prove to be a highly competitive solution to chemical functionalization [37]. Enhancing the processability, mechanical strength, thermal stability, and other desired attributes of cellulose-based materials becomes possible. Thus, hybrid materials with improved properties that neither component individually possesses are made possible. For instance, blending cellulose with polymers can lead to improved flexibility, strength, or toughness, while incorporating nanoparticles can provide electrical and thermal conductivities, antimicrobial properties, or optical functionalities [38-40]. To preserve biodegradability and biocompatibility, these materials should be selected carefully and used with cost-effective, green solutions. Within the scope of current limitations, i.e., sustainability, environmental friendliness, and goals like waste and fossil-based resource reliance reduction, biopolymers are a group that is perfectly suitable for novel material development.

The interactions discussed in the following sections can be divided into synergies with plant-based polysaccharides and lignin.

1.4. Cellulose – Lignin interaction

Lignin, often reported as the second most abundant biopolymer in biomass, is relatively different from cellulose [41]. Lignin can be classified as a polyphenol, which lends itself to primarily hydrophobic properties, and from a chemical point of view, it is incompatible with hydrophilic cellulose [42]. At the same time, lignin's significantly different set of properties can modify cellulose systems with their own unique set of properties. Borrowing concepts from nature, lignin protects cellulose from radiation, pests, and rotting and even regulates plant water transport [43]. Lignin is often compared to glue, which holds plant fibers and structures together. In nature, a balanced structure that consists mainly of cellulose, hemicellulose, and lignin is present in cell walls, where, in particular, lignin is bound together more with hemicellulose, creating naturally cross-linked structures with covalent bonding [44]. This leaves the reassembly

of just the lignin and cellulose systems relatively challenging, as lignin forms colloidal spheres on the cellulose fibers' surface, resulting in structural holes (gaps) [45]. One way to achieve a uniform hydro-stable lignin/cellulose composite is by heating (baking) it in an oven at 150 °C for several hours [46]. Figure 1.4 shows plant-inspired cellulose-lignin composite materials and their potential application as straws. This results in lignin filling the gaps in the micro- and nanostructure of cellulose fibers.

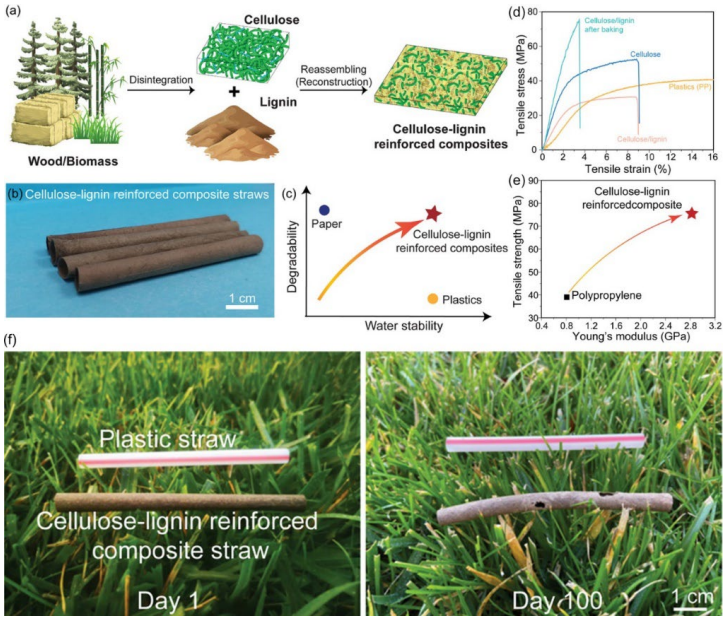

Figure 1.4. a) Schematic of the plant-inspired cellulose-lignin reinforced composite materials. b) Photograph of cellulose-lignin reinforced composite straws. c) Comparison between cellulose-lignin reinforced composite material with paper and plastics on degradability and water stability. d) Tensile stress–strain curves and e) Tensile strength and Young's modulus compassion of cellulose-lignin reinforced composite film compared with polypropylene. f) Degradation test for cellulose-lignin reinforced composite straw and plastic straw [47].

Vermaas et al. modeled lignin and cellulose interactions using molecular simulation and found that interactions depend on the cellulose surface, especially the hydrophobic face of the cellulose [42]. If micro-sized lignin is used as an additive to nanocellulose films (nanopapers), mechanical properties decrease while UV resistance is enhanced [48,49]. Thus, a way to directly enhance the contact surface would be to work with nanosized lignin and cellulose fibers, especially with water solutions. Huang et al. used nanosized lignin to improve the properties of cellulose nanofibers (CNF) and produced transparent films cast from a water suspension [50]. The composite films block 91.5 % of UV-A and 99.9 % of UV-B light, have antimicrobial properties, and even increase tensile strength by 32 % compared to neat CNF films. As an alternative, using solvents for cellulose solution preparation has been explored. This approach would reduce the inherent compatibility challenges and potentially reduce the requirements for producing high-quality nanoparticles. Follow-up research by the same institution tried to tailor

the surface morphology and physical performance of cellulosic nanofibril films by controlling lignin content in films [51]. It was reported that films with high lignin content lower the production cost and exhibit excellent hydrophobicity but reduce mechanical performance.

Guo et al. prepared transparent cellulose/lignin films using a dimethylacetamide (DMAc)/LiCl system and reported that adding 5 wt% lignin adds UV-shielding properties to films [52]. The authors could produce high-quality films from microcrystalline cellulose (MCC) by employing the solution method. Recent years have seen growing interest in using modern, greener, non-toxic solvents such as ionic liquids [53]. Ma et al. produced high-strength composite fibers from cellulose/lignin blends by dissolving pulp and organosolv/kraft lignin in the ionic liquid 1,5-diazabicyclo[4.3.0]non-5-enium acetate and applying dry-jet wet spinning [54]. The authors proposed two potential applications: naturally dyed textile fibers and using fibers as precursors for carbon fiber production. The potential to produce bio-based and sustainable carbon nanofibers from cellulose/lignin composites has recently seen relatively large scientific interest [55-57]. Still, the crucial step of stabilizing precursor fibers to withstand high carbonization temperatures remains the main challenge to obtaining high mechanical properties. While fiber spinning has seen relatively large interest, other possible applications include papers [58], aerogels (foams) [59], and hydrogels [60]. Nanolignin has been explored relatively extensively for various biomedical applications, from antimicrobial activity to assisted drug delivery; one such concept could involve cellulose-based wound dressings (in the form of mats or gels) filled with active lignin nanoparticles [61,62].

The selection of starting materials has been extensively studied, with one approach trying to utilize existing lignocellulose while the other uses the recombination of cellulose and lignin components. When examining the beneficial amounts of lignin needed to achieve the desired properties, the recombination route is interesting. Tian et al. prepared composite films by introducing various types of lignin into bacterial cellulose growth medium, which slowed the biodegradability of films in the presence of the Cellic CTec2 enzyme [63]. Water suspensions for sample preparation remain a relatively attractive option due to their simplicity and non-toxicity, but the requirements of nanosized components mainly limit them. Advanced materials and applications based on cellulose and lignin highly benefit from using solvents, as this solves inherent incompatibility issues and reduces the requirements for component processing. Lignin is commonly classified into Kraft, sulfate, and Organosolv types by extraction method [64]. The literature does not reveal a significant preference for one type.

1.5. Cellulose – Hemicellulose interaction

Hemicellulose, a polysaccharide, is among the most abundant biopolymers in the biosphere. Cellulose provides the structural framework for the cell wall, while hemicelluloses act as cross-linking agents that bond micro- and nanofibrils via hydrogen bonding [65]. Thus, hemicellulose acts as the supporting matrix for cellulose microfibrils. Hemicellulose composition varies between plant species, and the main types based on structure are known as xylans, xyloglucans, mannans, and glucans [66]. As such, in the literature, the names of specific hemicelluloses are used instead of the general term hemicellulose. Hemicellulose is highly hydrophilic, soluble in

hot water or alkalis, and susceptible to acid hydrolysis. The solubility of hemicellulose means that materials (composites) can be prepared from water solutions. The degree of polymerization of monomer units in hemicelluloses ranges between 80 and 200, notably lower than that of cellulose, which ranges upwards of 10 000 [67,68]. In addition, hemicelluloses are often branched molecules, unlike cellulose and structure is amorphous.

Hemicellulose's ability to support cellulose and improve its properties is known in papermaking. Ren et al. provided an overview of various modification types that benefit hemicellulose, most notably widely applied carboxymethylation [69]. Unsubstituted linear xylan was shown to have an excellent affinity for bacterial cellulose, while the presence of arabinosyl and O-acetyl substituents decreased the surface adsorption of xylan considerably [70]. Arola et al. examined CNF prepared from bleached birch Kraft pulp [71]. When xylan content was reduced by about 9 % from the original 27 %, the CNF network became stiffer and more rigid, but at the same time, fibril flocculation was more pronounced. Abdulkhani et al. used a significantly different strategy, using oxidized carboxymethyl cellulose and CNF to reinforce xylan films [72]. As a result, the composite films showed a tensile strength of up to 32 MPa, an elongation at break of up to 6.1 %, and a modulus of up to 465 MPa, which were found suitable for possible application as packaging material. Taylor et al. examined the effect of hemicellulose (xylans and glucomannans) content on the microfibrillation process [73]. The authors reported that higher hemicellulose content correlates with finer microfibril structure. Using the hydrophilic nature of hemicellulose, Berglund et al. prepared bacterial cellulose and hemicellulose-based hydrogels [74]. The addition of glucomannan increased stiffness and elastic modulus in compression tests, while xylan improved tensile elongation values. Tedeschi et al. prepared bioplastic films from microcrystalline cellulose, xylan, and hydrolyzed lignin [75]. The authors reported enhanced tensile properties, showing that hydrophobicity, water vapor, oxygen, and grease barrier properties can be tuned with component composition.

As can be seen, the commonly used method for cellulose/hemicellulose composite preparation involves component mixing in the water medium, thus trying to reconstruct structures like those in plant cell walls. For example, Szymańska-Chargot et al. cultivated bacterial cellulose with xyloglucan and pectin [76]. The authors reported that a lower ratio of xyloglucan to pectin in the composites yielded a higher Young's modulus and thinner fibers, while a higher ratio yielded longer microfibrils. In addition, cellulose crystallinity was reduced, which coincides with the reported results by Whitney et al. [77], where only xyloglucan was used. This approach is primarily notable for tuning the properties of bacterial cellulose structure, which can be applied in the desired field. The tailor-made bacterial cellulose films have already been reviewed by Chibrikov et al. [78].

1.6. Cellulose – Pectin interaction

Pectin, a biopolymer (heteropolysaccharide), is naturally occurring in cell walls and lamella with diverse structures that contain homogalacturonan (HG), rhamnogalacturonan I (RG I), and rhamnogalacturonan II (RG II) [79]. It is known that pectin polysaccharides can adsorb on the cellulose surface [80]. However, the interactions of pectin with cellulose and their influence on

mechanical properties are not fully understood. Using nuclear magnetic resonance (NMR), it has been shown that some pectin polysaccharides and cellulose have relatively strong interactions, and the authors proposed that pectic sidechains function as structural linkers between cellulose microfibrils [81]. Wang et al. detected sub-nanometer contacts between pectin and cellulose in the primary cell wall of the plant *Arabidopsis thaliana* [82]. Broxterman et al. detected substantial amounts of pectin in the final residue of enzymatically processed cellulose [83]. The release of RG-I-rich pectin during the enzymatic digestion of cellulose evidenced the covalent bonding between pectin and cellulose in the carrot cell wall.

High-methoxylated pectin (HMP) was integrated into bacterial cellulose (BC) by Cacicedo et al. [84]. SEM studies revealed the presence of structures composed of interconnected fibers. Moreover, composite films with 2.0 % HMP were tested as a drug delivery system for levofloxacin. The biocompatible, self-healing, and biodegradable drug-loaded hydrogel was prepared from acylhydrazide functionalized carboxymethyl cellulose (CMC) and oxidized pectin [85]. The hydrogel inhibited tumor growth in mice and reduced *in vivo* toxicity. Hydrogels made from pectin and cellulose exhibit considerable mechanical properties as well. Pectin-cellulose hydrogel synthesized with $CaCl_2$ as a cross-linker reached a swelling ratio of 567 %, a compressive strength of 49.31 MPa, a strain of 65.27 %, and a Young's modulus of 9.73 GPa [86]. Lopez-Sanchez et al. examined the impact of calcium pectin gel addition on bacterial cellulose hydrogel by introducing it before or after cellulose synthesis [87]. The introduction of pectin significantly enhances cellulose hydrogel properties. Assembly of the Ca^{2+}-pectate gel after cellulose synthesis led to more homogeneous gel distribution and higher mechanical properties. At the same time, direct molecular interaction between pectin and cellulose microfibrils was observed only when pectin was present during cellulose synthesis.

1.7. Cellulose – Starch interaction

Starch is a polysaccharide composed of two polymers: amylose and amylopectin. Both polymers, like cellulose, are built from D-glucopyranose units, indicating that strong hydrogen bonds can be formed. Due to its abundance and chemically inert structure, starch has found applications in pharmaceutics, where it is often combined with other polymers [88]. Formulations like alginate films, starch, and cellulose have been used as substitutes [89]. Starch promotes faster biodegradation, while cellulose provides better resistance to water and film dimensional stability. The affinity of starch films towards water and vapor permeability rates was reduced through intermolecular bonding between starch and CMC, improving barrier properties and making the material promising for food packaging [90]. The same study also determined the decrease in crystallinity when starch and cellulose were mixed to form a film. The decrease in crystallinity was explained by CMC acting as a lubricating agent and decreasing intermolecular interaction between starch chains. Ek et al. extruded high-amylose-content corn starch with cellulose loadings up to 30 wt% [91]. An expansion ratio of extrudates decreased as the cellulose content increased, while phase separation was observed. Chen et al. developed thermoplastic starch (TPS) composites with MCC loadings up to 9 wt% for use as packaging materials [92]. Hassan et al. used MCC powder as an additive (up to 5 wt%) to starch to prepare

citric acid crosslinked foams [93]. The authors used compression molding at 220 °C for thermal crosslinking and reported that formed bioplastics showed up to a 2-fold increase in tensile and flexural properties.

The formation of strong hydrogen bonds between MCC and starch molecules resulted in a tensile strength increase from 7.63 MPa to 12.47 MPa with an optimal loading of 6 wt% MCC compared to neat TPS. Souza et al. prepared starch films containing CNC-stabilized Pickering emulsions of different essential oils [94]. The elastic modulus increased from 223.7 to 479.5 and 491.7 MPa, and the tensile strength increased from 6.4 to 12.9 and 10.8 MPa by adding 2 and 5 wt% CNC, respectively. The results were achieved with ho wood oil, demonstrating the importance of nanoparticle dispersion, while a tensile strength increase shows excellent compatibility between cellulose and starch. A strong starch-CNC interaction was observed with 1.5 and 2.5 wt% CNC loading in the nanocomposite [95]. When CNC loading was increased to 5 and 10 wt%, aggregation and interference with hydrogen bonds in starch double helices were observed. In a different study by Ghasemlou et al., the synergistic reinforcement effect of CNC on starch and polyhydroxyurethane matrix was investigated [96]. The prepared nanohybrid materials were transparent, with hydrogen bonds contributing to a synergetic 26-fold increase in Young's modulus, corresponding to 440.1 MPa, which was observed when incorporating 2 wt% of CNCs in the matrix.

1.8. Processing biopolymers into functional materials

The design and integration of biopolymers into various materials must consider biopolymer characteristics. Biopolymers form strong intermolecular bonds, start to degrade at relatively low temperatures, and are often challenging to dissolve in large quantities. Thus, classical thermoplastic processing is not a suitable method for preparing biopolymer materials, although some workarounds that mimic these plastic properties are known, e.g., thermoplastic starch. In the case of solvents, there are often tradeoffs between quality, efficiency, price, and toxicity. Greener cellulose dissolving options, like an alkali/urea solution, have recently become popular [97-99]. Similarly, options like ionic liquids and deep eutectic solvents are widely explored [100-102].

Research with materials prepared from biopolymer suspensions often shows mechanical and morphological properties comparable to those of the dissolved cellulose approach, especially if nanoparticle suspensions are used [103]. Using biopolymer suspensions with water as a liquid medium is generally desirable as a green, cheap, and non-toxic route. Water that does not dissolve but swell biopolymers due to physically crosslinked polymer networks can be considered an advantage. Chemical crosslinking is commonly used to control the final structure for tuned properties [104]. These crosslinked water-swelled networks, often known as hydrogels, have seen massive interest in the biomedical research field but are not limited to other applications like sorbents for water treatments, sensors, stimuli-responsive devices, and others [105,106]. Aerogels or foams, which frequently start in the form of gels or hydrogels, are a particular class of adaptable, lightweight, high-specific-surface-area, and low thermal conductivity materials [107]. Aerogel powder can be employed as a drug delivery agent, while

typical applications include thermal or sound insulation, sorption, catalyst carriers, scaffolds, sensors, stimuli-responsive devices, and others [108,109].

Fibers are a crucial material type gradually returning to their bio-based and biodegradable origins. The return to biopolymer-based fibers aims to create biocompatible and biodegradable composites. Fibers obtained from renewable sources aim to counter fossil polymer pollution and non-renewable and energy-demanding processes applied to produce widely used glass and carbon fibers [110]. Similarly, versatile and biodegradable polymer films could replace fossil-based plastic packaging. This is especially important since packaging and one-time-use plastic products often end up in the wrong waste streams, are hard to recycle, and contribute to growing landfills [111]. Nevertheless, biopolymer films are not limited to such applications and can be applied to modern electroconductive materials, tissue recovery, skin impedance sensors, and other applications [112].

Biopolymer materials are extensively studied in biomedical fields due to their high value-added applications and biocompatibility, e.g., hydrogel consistency and water uptake can mimic living tissue [113]. Biopolymer fiber mats and films serve as excellent scaffolds for tissue recovery [114,115]. All forms of biopolymer materials have been used in some way or another to deliver active drug compounds [116,117]. While these are just some examples of biomedical applications, the main potential and growth of the biopolymer material field are centered around the industries widely dominated by conventional polymers and composites, such as adhesives, automotive, electronics, packaging, construction, etc.

2. MATERIALS AND METHODS

2.1. Materials

Cellulose and lignocellulose source

High-purity cellulose was obtained from old, unutilized laboratory filter paper. Paper was shredded using Retsch SM300, with a sieve size of 2.00 mm. The process was repeated with a sieve size of 0.25 mm, and for both pass-throughs, the mill rotation speed was 1500 rpm. The milled paper was used without further purification and treatment.

As the first processing waste, dried Santhica 27 variety hemp stalks were collected from a private farm in Latvia. The Retsch cutting mill SM300 (Retsch GmgH, Haan, Germany) was used to grind hemp stalks. The first grinding cycle used a sieve size of 4.00 mm, followed by the second and third milling cycles, which used sieve sizes of 0.25 mm and 0.12 mm, respectively. The mill was manually fed, and the rotation speed was set to 1500 rpm throughout the process.

Wood dust flour was obtained from Latvian birch plywood producer "Latvijas finieris" JSC as industrial waste from the plywood sanding process and was used as received.

Other chemicals

Laboratory-grade sodium hydroxide (NaOH) was used for lignin suspension preparation without further purification. Kraft lignin was purchased from Merck KGaA (Darmstadt, Germany) and used as received without additional processing. Beechwood xylan was purchased from Carl Roth GmbH (Karlsruhe, Germany). Merck KGaA (Darmstadt, Germany) provided PEG 300 (polyethylene glycol), apple pectin, glycerol, citric acid (CA), tert-butanol and dicumyl peroxide. All processes and sample preparation were carried out with deionized (DI) water.

Nanofibrillated cellulose and lignocellulose

For nanopaper production, nanofibrillated cellulose (NFC) and nanofibrillated lignocellulose were prepared by dispersing 1 wt% of milled paper or milled hemp in DI water. Both nanofibrillated celluloses are hereafter abbreviated as NFC or NC (nanocellulose). The obtained aqueous dispersion was mixed in an ordinary kitchen blender (800W) and then passed through a microfluidizer (LM20, Microfluidic, U.S.A.) equipped with a chamber H210Z (200 μm). Five passes were used to increase the degree of defibrillation. The pump pressure was set at 30,000 psi.

For lignocellulose foam production, alkaline treatment was used to remove lignin, hemicellulose, and other non-cellulosic substances from source waste material to facilitate the mechanical defibrillation process. Separately, wood and hemp were immersed into 5 wt% NaOH solution (cellulose to NaOH solution ratio was 1:8) in the stainless-steel kettle and heated up to 80 °C for 3h under continuous stirring. Afterwards, the solution was carefully discarded, replaced with a fresh one, and left overnight at room temperature under constant stirring. After treatment, wood and hemp particles were filtered and washed with DI water until the slurry's pH reached DI water values (around 7.0). The obtained slurry was dried in a laboratory oven at

50 °C. The chemical composition of wood and hemp before and after alkaline treatment is summarized in Table 2.1. Hemp showed around 68% and 89% cellulose content, while wood samples – were around 40% and 57% before and after treatment, correspondingly.

Nanolignocellulose suspensions with concentrations of 0.2, 0.5, and 1.0 wt% were prepared from alkaline treated wood and hemp waste powders by redispersing them in DI water with vigorous stirring for 8 hours. The obtained aqueous suspensions were passed through a microfluidizer (LM20, Microfluidic, U.S.A.) with chamber H210Z (200 μm) as described previously. High cellulose concentration dispersions clog the apparatus, so the 3.0 wt% was obtained from 1.0 wt% suspension by evaporating excess water at 80 °C with continuous stirring until the desired concentration was achieved.

For the phase 4 study, an aqueous suspension containing 1.5 wt% of the ground hemp (without chemical treatment) was prepared using deionized water. This suspension was mixed in a conventional 800 W kitchen blender for 2 minutes, then processed in a Microfluidics microfluidizer. The microfluidizer was set to a pressure of 30,000 psi, and the material underwent five passthrough cycles for uniform defibrillation. The process resulted in the production of hemp NFC with dimensions of 86 ± 41 nm.

Table 2.1.

Chemical composition of wood and hemp before and after treatment

Chemical composition (% odp)	**Wood**	**Treated wood**	**Hemp**	**Treated hemp**
Ethanol-Benzene extractives	2.02	0.44	1.78	0.10
Glucan*	40.35 ± 0.68	56.63 ± 0.82	68.49 ± 0.77	88.78 ± 0.19
Xylan**	19.01 ± 0.21	9.78 ± 0.10	2.95 ± 0.04	2.39 ± 0.00
Rhamnan**	0.90 ± 0.07	0.00 ± 0.00	1.36 ± 0.07	Traces
Galactan**	0.89 ± 0.05	0.70 ± 0.02	1.51 ± 0.04	0.88 ± 0.04
Arabinan**	0.30 ± 0.03	0.29 ± 0.04	0.65 ± 0.06	0.27 ± 0.04
Mannan**	1.83 ± 0.05	1.54 ± 0.05	4.60 ± 0.09	1.69 ± 0.11
Acid Soluble Lignin	0.00 ± 0.00	0.00 ± 0.00	0.00 ± 0.00	0.00 ± 0.00
Acid Insoluble Lignin	19.29 ± 0.09	24.06 ± 0.11	5.98 ± 0.10	4.30 ± 0.10
Acetyl groups	4.59 ± 0.18	0.00 ± 0.00	1.25 ± 0.02	0.00 ± 0.00
Other identified comp.	1.26 ± 0.2	1.34 ± 0.03	1.69 ± 0.02	1.61 ± 0.09

odp: oven-dry pulp

*Cellulose

**Hemicellulose

Lignin and Xylan solution preparation

50 g of kraft lignin was first suspended in 470 mL of DI water and stirred magnetically for 1 h at 85 °C. The suspension was stabilized to pH 10 using a strong alkaline solution (NaOH). A dark, homogeneous suspension was obtained, having a lignin concentration of 10 wt% (adjusted with evaporation). For the phase 4 study, this suspension was then passed through medium-pore laboratory filter paper using a Büchner funnel, a Bunsen flask, and a vacuum

pump system. A second filtration was conducted using smaller pore-sized filter paper. After these steps, the final lignin solution had a concentration of 2.2 wt%.

30 g of beechwood xylan was dissolved in 285 mL of DI water and stirred magnetically at 80–85 °C for 1 h until the xylan dissolved in the water. A slightly brown, viscous solution was obtained, having a xylan concentration of 10 wt% (adjusted with evaporation). After cooling at room temperature, both solutions were used as follows in the preparation of the samples.

Cellulose and lignocellulose nanopaper preparation

Nanopaper films from wastepaper were produced by casting 1 wt% NFC dispersion onto polystyrene Petri dishes. Dispersions and solutions were mixed (with xylan and lignin) to selected concentrations, magnetically stirred for 2 h, cast onto prepared Petri dishes, and placed at room temperature until evaporation. Afterwards, the nanopaper films were dried in a laboratory oven at 50 °C for 24 h. 1, 2.5, 5, 10, 20, and 30 wt% of lignin (L) and xylan (X) loadings into cellulose nanopaper were prepared. In the text, single filler samples have been abbreviated as L and X, combined with the filler concentration number. At the same time, several complex compositions with simultaneous lignin and xylan loading were also proposed, abbreviated as LX systems. For example, the X1 sample corresponds to xylan 1 wt% loading, L1 sample – lignin 1 wt% loading, L1X1 sample – lignin 1 wt% and xylan 1 wt% complex loadings. A sample without any loading is abbreviated as cellulose nanopaper (CNP).

Hemp paper films were made by pouring a microfluidized 1 wt% dispersion onto 145 mm polystyrene (PS) Petri plates and leaving them at room temperature until evaporation. The films were then dried in a laboratory oven at 50 °C for 24 h.

Hemp paper impregnation – preparation of bioplastics

A 10 wt% xylan solution was combined with PEG, glycerol, and citric acid in various weight ratios. To better facilitate and catalyze the crosslinking reaction, dicumyl peroxide was also added (0.1 wt% of the mixture's total weight dissolved in roughly 1-2 ml of acetone). The combined mixture was stirred until the citric acid was completely dissolved and the mixture was homogeneous. The prepared mixture was poured into a polystyrene petri dish, and the previously prepared hemp paper was fully immersed in the mixture overnight. Before temperature treatment, any excess mixture was gently scraped off the paper, leaving only impregnated paper. The impregnated paper was then crosslinked in a laboratory oven for 12 h at 140 °C. Figure 2.1 depicts the whole sample preparation procedure. The names of the prepared samples were derived from the weight ratios of the components, which were abbreviated as XPGC (X - Xylan solution 10 wt%; P - PEG 300; G - Glycerol; C - Citric acid). For example, 2:1:2:2 is made up of two parts Xylan solution, one part PEG 300, two parts Glycerol, and two parts Citric acid. Visual images of bioplastics and impregnated mixtures are shown in Figure 2.2. All seven prepared mixtures are represented in Table 2.2. Abbreviations throughout the work are used for impregnated hemp papers after 48 hours of washing in water and following the drying step unless specified otherwise. Hemp paper is abbreviated as “hemp,” and its structure is studied after initial paper casting.

A three-layer laminate was prepared using the same principles as described above. Three hemp papers were impregnated separately, and the excess mixture was scraped off. Then all three impregnated papers were combined and put in the laboratory oven at 140 °C for the crosslinking reaction under 10 kg weight for 12 h.

Table 2.2.

Prepared sample mixtures with various component weight ratios

Sample abbreviations*	**Impregnated composition** **Xylan : PEG : Glycerol : Citric acid (weight ratio)**
Hemp	-
1:2:1:1	1 : 2 : 1 : 1
2:1:2:2	2 : 1 : 2 : 2
2:2:1:2	2 : 2 : 1 : 2
4:2:1:1	4 : 2 : 1 : 1
4:4:1:1	4 : 4 : 1 : 1
4:4:1:2	4 : 4 : 1 : 2
4:8:1:1	4 : 8 : 1 : 1

***** Impregnated composition abbreviations are used for dried samples after 48 h washing in water unless specified otherwise.

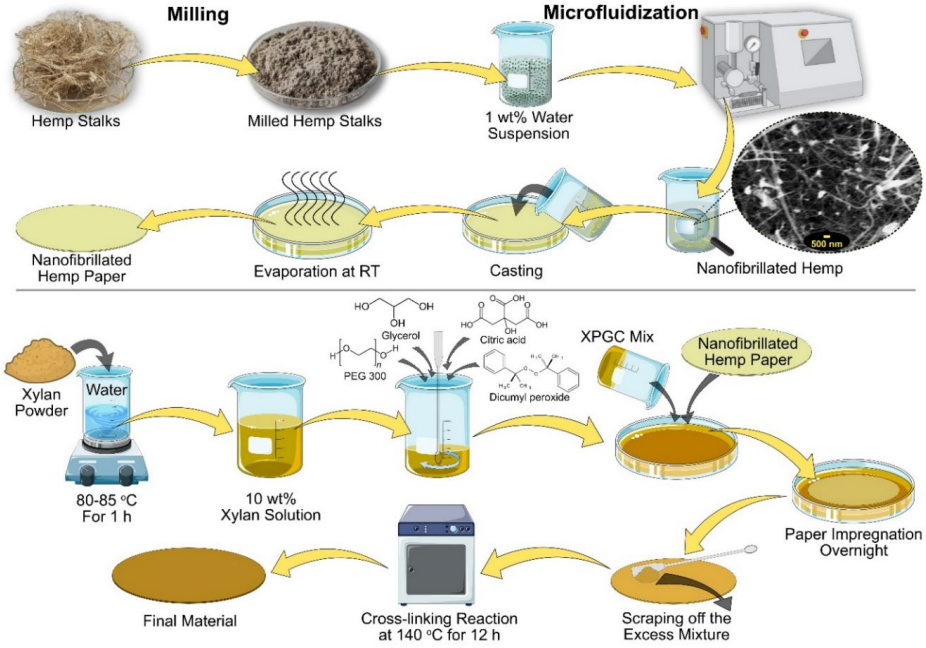

Figure 2.1. Schematic illustration showing the main steps of hemp bioplastic preparation.

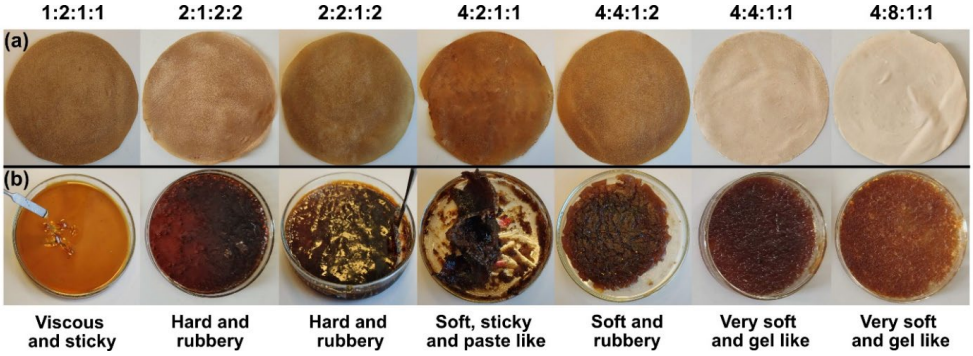

Figure 2.2. (a) Hemp bioplastics after impregnation and crosslinking, (b) crosslinked impregnation mixture.

Nanolignocellulose foam preparation

Foams for the phase 3 study were fabricated using the freeze-drying method. The obtained NC suspensions were vigorously stirred and poured into cylindrical polypropylene molds of 35 mm in diameter. Afterwards, every mold was plunged into liquid nitrogen to freeze and solidify. Freeze-drying was done via a vacuum freeze dryer Sentry 2.0, VirTis SP Scientific, at a condenser temperature of -60 °C and a high vacuum of 200 mT. The sublimation process was carried out for 72 hours. Obtained foam samples were self-standing, lightweight, and soft.

For phase 4 study crosslinked lignocellulose foams were prepared utilizing the freeze-drying technique according to the following detailed protocol. To produce unaltered lignocellulose foams, a 1.5 wt% hemp NFC suspension was combined with varying quantities of citric acid (CA), ranging from 0.5 to 5 g per 100 g of suspension, corresponding to approximately 0.5-5 wt% CA. This mixture was vigorously agitated using a magnetic stirrer. To each blend, 10 wt% tert-butanol was added and similarly stirred vigorously. The resultant suspension was then transferred into cylindrical polypropylene trays with a diameter of 43 mm. These trays were subjected to freezing at -80 °C in the condenser chamber of a Telstar LyoQuest -85 plus freeze-dryer until they were completely solidified. Subsequently, the samples were relocated to the vacuum chamber of the freeze-dryer and subjected to a high vacuum of 0.03 mbar. The sublimation process was conducted over a period of 72 hours. The resulting foam samples were self-supporting, lightweight, and soft.

Thermal heating was employed to initiate the CA crosslinking reaction. Dicumyl peroxide (DP) was utilized as a catalyst for this reaction. A minuscule quantity of DP, specifically two flakes, was dissolved in 2 ml of acetone. This solution was then applied to the surface of the foam samples using a dropper, administering three drops per sample. Subsequently, the samples were placed in a laboratory oven at 140 °C for 6 hours to facilitate the crosslinking reaction. A pure hemp foam sample without added CA or crosslinking was also prepared for comparative purposes. The nomenclature for these samples was designated as H- (indicating hemp) and CA(0.5-5) to denote the amount of citric acid used. For example, H-CA0.5 refers to a hemp foam crosslinked with 0.5 g of CA.

For the creation of wood mimic (WM) foams, lignin and xylan solutions were incorporated into the same 1.5 wt% hemp NFC suspension to achieve a composition mimicking that of average hardwood: 45% hemp, 35% xylan and 20% lignin by dry weight. The NFC suspension was thoroughly mixed with the lignin and xylan solutions using a magnetic mixer for 30 minutes. As in the previous process, similar quantities of citric acid and tert-butanol were added to the WM suspension and vigorously stirred. The subsequent steps for foam preparation were identical to those described earlier. A pure WM foam sample without added CA and crosslinking was also prepared for reference. The sample naming convention was analogous to the previous series, denoted as WM- (wood mimic) and -CA(0.5-5) for the quantity of citric acid added.

Furthermore, both Hemp and WM suspensions were modified with pectin and glycerol. Compositions, including solely pectin or glycerol, as well as hybrid variants with both additives, were explored. For pectin-modified foams, varying amounts of pectin (0.25-1 g) were dissolved in the Hemp NFC and WM suspensions and stirred magnetically at 80–85 °C for 1 hour until fully dissolved. Subsequently, 1 g of citric acid and 10 wt% tert-butanol were added. For the glycerol-modified versions, different glycerol quantities (0.5-2 g) were incorporated and similarly stirred. In both pectin and glycerol-modified foams, a constant amount of 1 g CA was used, with varying amounts of pectin and glycerol. The preparation steps for these foams were consistent with those outlined above. The sample naming scheme remained the same, with pectin denoted as -P and Glycerol as -G. The amount of each component added is indicated next to the respective abbreviation. For instance, the hybrid sample WM-P0.5-G2-CA1 comprises WM suspension, 0.5 g pectin, 2 g glycerol, and 1 g citric acid. A comprehensive summary of all prepared compositions and the quantities of each modifier used is presented in Supplementary 9, encompassing a total of 25 distinct compositions. Overall schematic showing the main steps of foam preparation and some sample pictures is illustrated in Figure 2.3.

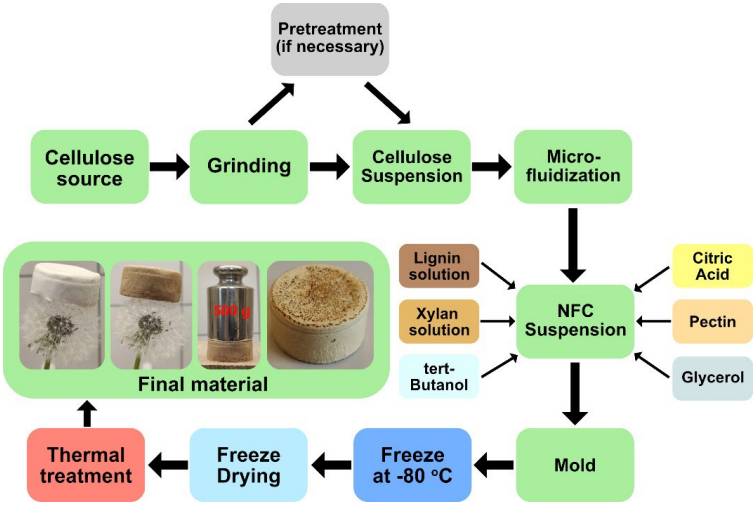

Figure 2.3. Overall schematic showing the main steps of foam preparation and some sample pictures.

2.2. Testing methods

Chemical composition analysis

The structural carbohydrates in wood and hemp samples before and after treatment were determined according to the NREL/TP-510-42618 issued by the U.S. National Renewable Energy Laboratory. The biomass's chemical composition (C-5 sugars, C-6 sugars, and lignin) was determined by performing a two-step sequential acid hydrolysis, based on the material reaction with 72 wt% H_2SO_4 at 30 °C for 1 h. After this pretreatment, DI water was added to the mixture to dilute H_2SO_4 to 4 wt% and autoclaved at 121 °C for 1 h. The concentrations of saccharides were determined by high-performance liquid chromatography (HPLC) using a Shimadzu LC20AD liquid chromatograph equipped with an RI detector (Shimadzu RID 10A), and a Shodex Sugar SP-0810 column at 80 °C, DI water as a mobile phase under a flow rate of 0.6 mL/min. The concentration of hydrolysis process byproducts, such as formic acid, acetic acid, levulinic acid, 5-hydroxymethylfurfural, and furfural, was also analyzed by the same HPLC but using a Shodex Sugar SH-1821 column at 50 °C, 0.008 M H_2SO_4 as eluent at a flow rate of 0.6 mL/min. Before determining carbohydrates in the previously prepared biomass, the quantification of extractives was performed according to the TAPPI 204 cm-07 standard. The solvent used was ethanol-benzene in the ratio 1:2. The extraction time was 5 h.

Zeta potential measurements

Zeta potential assessment of colloidal stability of prepared suspensions was acquired using a Malvern Zetasizer Nano ZS particle analyzer. Each defibrillated suspension was diluted with DI water to 0.01 wt%, sonicated for 5 min, and then analyzed. Measurements were made at ambient room temperature of 22 °C and pH of 7. Smoluchowski's model was chosen for the calculation of zeta potential. No additional electrolytes were added to the suspension.

Density, porosity, volume shrinkage

The apparent density of bioplastic and foam samples was calculated by dividing the weight of the sample by its volume. The sample's weight was measured by an analytical balance (readability 0.0001 g, Precisa XT 220A, Precisa Gravimetrics AG, Switzerland), and a digital caliper measured the dimensions of the sample at five different positions.

Porosity (P) was calculated by considering a simple mixing rule with a negligible gas density and using the apparent density (ρ_a) and the theoretical density (ρ_t) of the sample using expression (2.1):

$$P(\%) = \left(1 - \frac{\rho_a}{\rho_t}\right) \times 100, \tag{2.1}$$

The theoretical density (ρ_t) of the sample was calculated using a simple density addition approach with expression (2.2):

$$\rho_t = a\rho_{hemp} + b\rho_{XPGC}, \tag{2.2}$$

where *a* and *b* are percentile contributions in the sample; ρ_{hemp} is the skeletal density of cellulose (1.5 g/cm^3); ρ_{XPGC} is the theoretical density of the impregnation mixture, which was also calculated using the same approach by adding each component density and its percentile contribution.

Volume shrinkage was determined by accurately measuring the dimensions (diameter and height) of the samples using a digital caliper with a precision of 0.01 mm. The calculation of percentage volume shrinkage was conducted using expression (2.3).

$$Volume\ shrinkage(\%) = \frac{(V_m - V_s)}{V_m} \times 100, \quad (2.3)$$

where, Vm and Vs are the volumes of the mold and sample after drying, respectively.

Sol content and water uptake

The unreacted part of the XPGC mixture that dissolves in water and can occur after the crosslinking reaction is referred to as the sol content. The sol content was determined by dissolving bioplastic in water for 48 h at room temperature with occasional stirring. After water treatment, the samples were dried in a laboratory oven at 60 °C until a consistent dried weight was achieved. The unreacted part of the XPGC mixture was calculated as the sol content using the expression (2.4):

$$Sol\ content(wt\%) = \frac{(m_0 - m_{dry})}{m_0} \times 100, \quad (2.4)$$

where m_0 is the initial sample weight, m_{dry} is the dry sample weight after rinsing with water.

Water uptake was determined similarly. Dry bioplastics were immersed in water at room temperature for 30 days after being treated with water. During this time, the sample weight was monitored; however, weight equilibrium was consistent after the first 24 hours. Samples were gently wiped with a paper towel before weighing. Water uptake was calculated using the expression (2.5):

$$Water\ uptake(\%) = \frac{(m_{wet} - m_0)}{m_0} \times 100, \quad (2.5)$$

where m_{wet} is the wet sample weight, and m_0 is the initial sample weight.

Absorption capacity

The absorption capacity of foam samples was evaluated in various mediums, including water, rapeseed oil, and kerosene. Each sample was submerged in the respective medium for a duration of 5 minutes. The absorption capacity was quantitatively determined using the following equation (2.6):

$$Absorption\ capacity(g/g) = \frac{(m_2 - m_1)}{m_1}, \quad (2.6)$$

where m_1 and m_2 are the foam weights before and after the immersion, respectively. Additionally, the cycling performance of the samples was assessed for water and kerosene absorption (oil samples only lasted one cycle). This involved a systematic process where, after each absorption cycle, the sample was compressed to expel the absorbed fluid, and then re-immersed in the medium for subsequent absorption measurements. This process was repeated until the sample either deteriorated or completed 10 cycles. For certain hydrophobic foam compositions, the absorption process in the water medium was further enhanced by mechanically compressing the sample.

Morphology

Particle size for raw wood and hemp waste particles was calculated using images from fibers deposited on a glass slide taken using optical microscope Leica DMR (Leica Microsystems, Germany) at 10x magnification. Leica Image Suite™ software was used for the measurement of fiber length and diameter. A hundred measurements were acquired, and statistical analyses were performed to identify mean fibers like particle length and diameter.

The FEI Nova NanoSEM 650 Schottky field emission scanning electron microscope (FESEM) was used to examine the morphology and structure of prepared materials. The morphology of nanopapers and bioplastics was studied with Scanning Electron Microscopy (SEM) at a voltage of 10 kV. Crosscuts were obtained in liquid nitrogen. Coatings were not applied on the surface or crosscut surfaces. Phase 4 foam samples, prior to the examination, were coated with a 3.6 nm layer of gold.

To acquire images of NFC, a Scanning Transmission Electron Microscopy (STEM) probe was used. Measurements were performed in transmission configuration using an acceleration voltage of 10 kV. A 400 W ultrasound probe was used to sonicate a diluted NFC suspension for 1 minute. After that, the NFC suspension droplet was placed on a copper grid (mesh 200) and allowed to evaporate at room temperature.

Thermal characterization

The thermal stability was evaluated with thermogravimetric analysis (TGA) using a Mettler TG50 instrument. Measurements were performed on samples with a weight of about 10 mg. Heating under an oxygen atmosphere was conducted from 25 to 750 °C with a heating rate of 10 °C/min.

The thermal conductivity and thermal diffusivity were evaluated with the Netzch LFA 447 NanoFlash System. The film specimens were heated with a Xenon flash lamp (10 J/pulse) in the air. The measurements were taken at three temperatures: 25 °C, 35 °C, and 45 °C. Before testing, the samples were coated with graphite to enhance the absorption of light energy and the emission of infra-red radiation to the detector.

The thermal conductivity of foams was determined by the transient plane source method HotDisk TPS500. A sensor with a radius of 3.189 mm was placed between two identical cylindrical samples with a diameter of 30 mm and a total height (distance) more than 10 mm. 10 mW power was supplied to the sensor and a measurement time was set to 20 s. These parameters were experimentally found as optimal ones to satisfy requirements for the device and material type, i.e., allowable ranges for the characteristic time, probing depth, and temperature increase. For each pair of samples, five measurements were repeated with 15 min interval between them. The thermal conductivity (k) was calculated using at least three intervals from temperature vs. time curves. The mean values for k are average from at least fifteen measurements. The effective thermal conductivity is expressed as a sum of two components (2.7):

$$k = k_c + k_r, \tag{2.7}$$

where k_c is a combination of thermal conductivity from gas and solid, k_r is a combination of the radiation through skeleton and contribution from voids. Four models are considered to calculate the effective thermal conductivity of the produced foams.

UV irradiation

Samples with thicknesses around 0.1 mm in the shape of strips, 10 mm in width and 40 mm in length, were cut from films. Before testing, samples were stored in a thermostat at 50 °C and RH < 10%. These samples are considered dry reference samples. The samples were removed from the thermostat (50 °C and RH < 10%). Films were irradiated with 1.6 W/cm^2 intensity and at a fixed distance of 25 cm from the source. A deep UV exposure lamp (Hg, 1000 W) with a broad emission spectral range from 200 to 600 nm was used as an irradiation source in an air environment. The constant temper-ature of 80 °C was maintained in the experimental chamber with the UV lamp. Exposure time was set to 6, 12 and 24 h. After irradiation, samples were collected in sealable plastic bags and kept for 24 h, before performing a tensile test.

X-ray diffraction (XRD)

The wide-angle X-ray diffraction (WAXD) measurements were carried out to evaluate the crystallinity of the NC. They were obtained on a Panalitical X'Pert PRO diffractometer at a temperature of 20 °C. The monochromatic irradiation of CuKα with a wavelength of λ = 0.154 nm in the range of scattered radiation angles 2θ from 5° to 40° was used. The voltage was 40 kV, current 30 mA, and the scanning rate 0.05 deg/s. The crystallinity index (CI) was calculated using the empirical equation (2.8) by Segal et al. method [118,119]:

$$CI(\%) = \left(1 - \frac{I_{am}}{I_{002}}\right) \times 100, \quad (2.8)$$

where I_{002} is the maximum intensity of the lattice's diffraction band located in the interval 2θ = 21 – 23 °. I_{am} is the minimum intensity for diffraction band 2θ = 18 – 20 °, which corresponds to an amorphous part.

Spectroscopy

UV-vis absorbance was measured in a range from 240 to 740 nm using a Sol-idSpec3700 UV-VIS-NIR Shimadzu (Kyoto, Japan) spectrophotometer. White $BaSO_4$ plate was used as the reference plate for all measurements. Three parallel measurements were combined in the final spectra.

Nicolet 6700 (Thermo-Scientific, Waltham, MA, USA) Fourier transform infrared spectroscopy (FTIR) in attenuated total reflectance (ATR) mode was used to investigate prepared material with a resolution of 4 cm^{-1} in the 650–4000 cm^{-1} range. Sixteen measurements were made on each specimen, and the average spectrum was given.

The dielectric characteristics were measured using a Novocontrol Alpha Broadband (Novocontrol technologies, Germany) dielectric spectrometer. Samples with a diameter of 20 mm were placed between plate electrodes and evaluated at 22 °C with a frequency range of 0.01–10 MHz.

Rheology

Rheological measurements were recorded using an Anton Paar Smart Pave 102 (Graz, Austria) rheometer with a parallel plate measuring system PP25 (plate diameter 25 mm). The crosslinking reaction was monitored using a time sweep measurement at a constant temperature of 140 °C. Time sweep measurements were carried out with a strain of 0.2% and a frequency of 3 Hz. The initial gap was set to 0.3 mm with no force adjustment. These parameters were chosen to mimic the stationary crosslinking process and are in the linear viscoelastic region (LVR), as determined by a strain sweep experiment.

Moisture absorption

Samples were conditioned in desiccators under different relative humidity environments (RH%) at room temperature 22 °C. The humid environments were created by using different saturated salt solutions: $KC_2H_3O_2$ (RH24%), NaCl (RH75%), and K_2SO_4 (RH97%). Gravimetric measurements were made with an accuracy of 0.01 mg, and the relative weight changes of samples w [%] were determined as weight gain per weight unit. Moisture saturation was achieved within 3-7 days. Retention of the me-chanical properties after moisture desorption was studied on samples initially satu-rated at RH75% and RH97% and then conditioned at RH24% until weight stabilization: abbreviated as RH75-->24% and RH97-->24%, respectively.

Hydrophobicity

The water contact angle (WCA) was measured using the static sessile drop technique, employing a Theta Lite optical tensiometer (Attension® Biolin Scientific, Gothenburg, Sweden). This process involved making five distinct measurements for 60 seconds, each using a 2 µL droplet of water placed on the surface of the specimen.

Mechanical properties

Tensile tests were performed on nanopaper films using a universal testing machine, Tinius Olsen model 25ST (USA), equipped with a load cell of 5 kN at 1 mm/min crosshead speed. The cellulose nanopaper was cut into a rectangle strip of 10 mm in width and about 40 mm in length. The gauge length between grips was 20 mm. Five parallel measurements were performed for each film sample at room temperature and ambient conditions. The samples were conditioned for 48 h at 50% humidity and measured at 20 °C.

Tensile properties of moisture-saturated samples were tested using a Zwick testing machine with a load cell of 2.5 kN at a crosshead speed of 1 mm/min. Tabs from the paper tape were applied to the samples, and the gauge length was set to 20 mm. The elastic modulus was determined in the linear part of the stress-strain curve within the strain range of 0.2 – 0.5%. Five replicate samples were tested immediately after their extraction from a desiccator (within 1 to 2 min) for each NP composition and RH.

A compression test for foam samples was conducted using the Tinius Olsen model 25ST (USA) universal testing machine equipped with a load cell of 5 kN. The cylindrical samples with a height of 25 mm were compressed at a rate of 5 mm/min. Before the testing, the samples were preconditioned for 24 h at room temperature and ambient conditions. Sandpaper was used

to even the sample surface if necessary. The mean result of three specimens for each sample is reported.

Experimental Design and Response Surface Technique.

The effect of lignin and xylan on the mechanical properties of the nanopaper was assessed in several stages: (a) the selection of the design parameters and their intervals of variation, (b) the development of the design experiment for the parameters selected, (c) experimental testing, and (d) the determination of the second-order polynomial regression equation.

The full-factorial design (FFD) has been selected, generating 9 experimental runs for two parameters and three levels (Supplementary 1). The minimum and maximum levels for the design parameters are given in Table 2.3.

Table 2.3.

Process parameters and their levels

Parameters	**Levels**		
Lignin (wt%)	1	2.5	5
Xylan (wt%)	1	2.5	5

A second-order polynomial regression equation (2.9) has been proposed to predict the response of polymer composites.

$$F(x) = b_0 + \sum_{i=1}^{m} b_i x_i + \sum_{i=1}^{m} \sum_{j=i}^{m} b_{ij} x_i^2 + \sum_{i=1}^{m} \sum_{j=i}^{m} b_{ij} x_i x_j, \quad (2.9)$$

where $F(x)$ *is* the response, x_i and x_j are the values of parameters, b_0 is the constant, b_i, b_j, and b_{ij} are regression coefficients, respectively, and m is the number of the parameters.

The design parameters and experimental values of specific modulus, specific stress, and strain were determined by averaging the test results of 5 specimens of nanopapers and are presented in Supplementary 1.

3. RESULTS AND DISCUSSION

3.1. Clean manufacturing of cellulose nanopapers by incorporating lignin and xylan as sustainable additives

This work reports the clean manufacturing of cellulose nanopapers by a green path of mixing nanocellulose suspension in water with lignin and xylan. The procedure involves grinding the old wastepaper, microfluidizing, casting, and water evaporation. The introduction of lignin and xylan with various loadings from 1 to 30 wt% showed that properties could be significantly tuned. Moreover, lignin and xylan loadings introduced into these nanopapers endow them with improved mechanical and structural properties, as evidenced by tensile tests and scanning electron microscopy analysis. Xylan strongly promotes the transparency of nanopapers. Even at low loadings, adding xylan and lignin enhanced specific strength by 1.3-fold, while specific elastic modulus exhibited a 2-fold enhancement. Mathematical modeling complemented the analysis of tensile properties. Thermogravimetric analysis testified that the wastepaper is made of highly purified cellulose.

Furthermore, thermal properties analysis shows that the modified nanopapers have higher thermal conductivity and diffusivity than the unmodified ones. Thermal conductivity was found to improve 3.5-fold for compositions with 30 wt% loading of modifiers corresponding to the developed denser structure as revealed by SEM. The introduced crosscut and surface structure changes enable functional applications to obtain packaging, filtering, biomedical, and sensor materials.

3.1.1. Morphological properties

After shredding in the mill, the mean length of fibers was 280 μm, and the width was up to 50 μm. Therefore, mechanical delamination with microfluidization was carried out to reduce the fiber dimensions to the nanoscale. STEM micrograph shows long nanofibrils (Figure 3.1) with an average width of 86±41 nm.

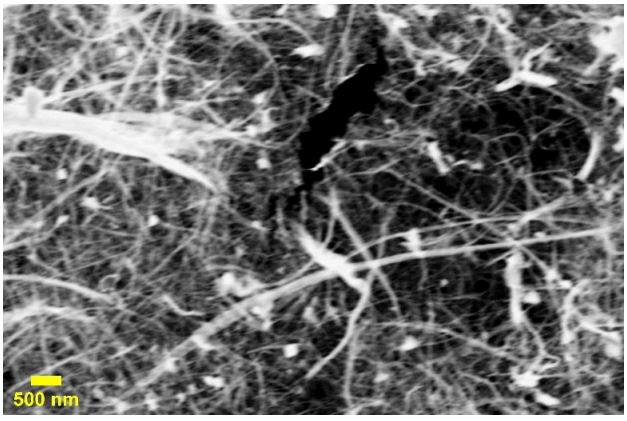

Figure 3.1. STEM image of NFC obtained from wastepaper.

Figure 3.2 presents the surface and cross-section micrographs of the obtained NPs. The network of randomly orientated fibers is visible with dimensions in micrometers, indicating that NFC has formed microfibril aggregates. Similar observations were made by Henriksson et al. [120]. In addition, a crosscut image of NP shows a rough structure with visible microfibril ends. Adding lignin to NFC significantly changes the crosscutting structure of NPs, introducing visible voids in all examined samples. Lignin addition also reduces crosscut surface roughness. The L5 sample has larger voids than the L1. Thus, the addition of lignin directly causes the formation of voids, as observed in the microstructure. While the construction of cavities could be helpful in specific filtration applications, it would directly influence the mechanical properties of the present NPs [121,122].

The addition of xylan has been found to contribute to the formation of a relatively smooth crosscut surface, like the surface formed by CNP. The X1 sample shows some structural defects, such as voids and layer separation, which are not visible in the X5 sample. As a result, xylan fills the void spaces between cellulose fibrils, resulting in continuous smooth crosscut surfaces with no visible micro- or nanostructure voids. As Goksu et al. [123] and Hansen et al. [124] reported, xylan content can significantly affect the porosity and water vapor transmission rate. Hybrid compositions L1X1 and L5X5 show that lignin strongly influenced the formation of the structure, which is visually comparable to L1 and L5 NPs.

The transparency and visual appearance of NPs are presented in Figure 3.3. The reference CNP shows a distinct white color without transparency. Adding lignin results in a substantial color shift from yellow to dark brown and the appearance of grainy texture in the form of small lignin particle agglomerates. At the same time, all xylan NPs are transparent, but loadings of 2.5 wt% and above yield a yellowish tint in color. It has been reported earlier that eliminating structural cavities in nanopapers yields transparent structures due to the significantly reduced light scattering [125]. In our case, casting did not yield such a dense structure for CNP. Still, as revealed by SEM analysis, xylan fills all the cavities between cellulose fibrils, thus providing a simple modification route for transparent NP.

3.1.2. Tensile properties

The stress-strain curves measured for NPs samples are presented in Figure 3.4. The behaviour of all curves is predominantly linear, consisting of the elastic and plastic regions. A substantial increase in the samples' rigidity and material brittleness for lignin, xylan (loadings above 5 wt%), and single, and complex filling systems has been observed. It has been suggested that such behavior is caused by decreased slippage yield deformation between the extended cellulose fibrils rather than by covalent bond breakage [126].

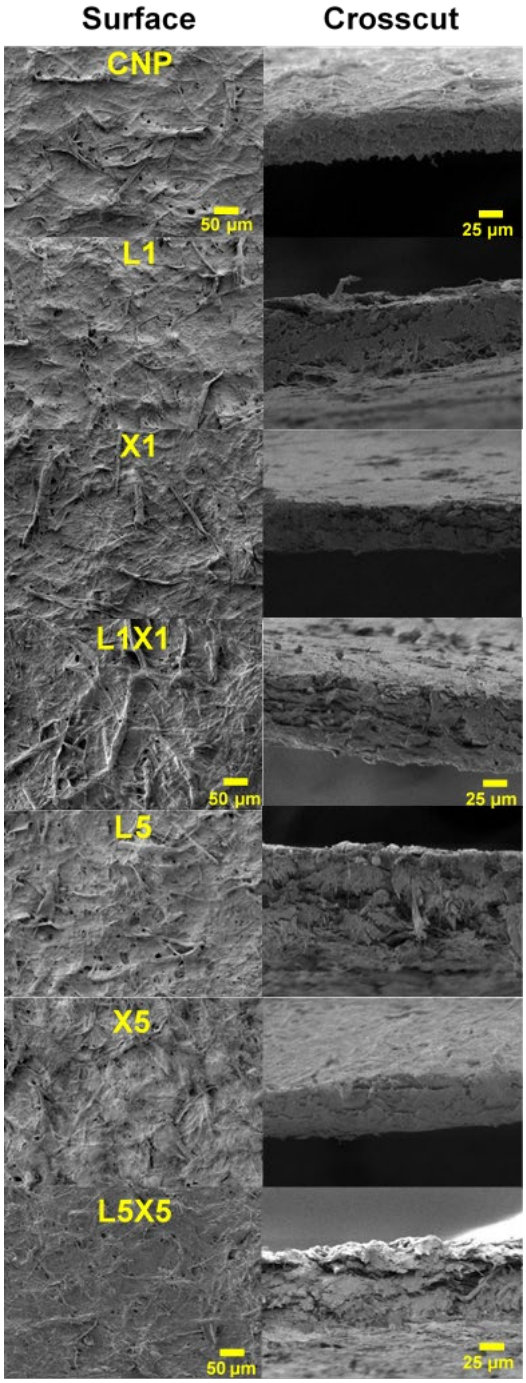

Figure 3.2. SEM images of cellulose nanopapers surfaces and crosscuts with lignin and xylan loadings.

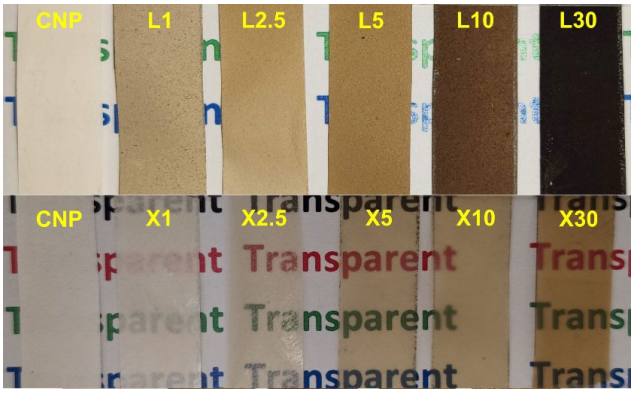

Figure 3.3. Transparency comparison of prepared NPs with lignin and xylan.

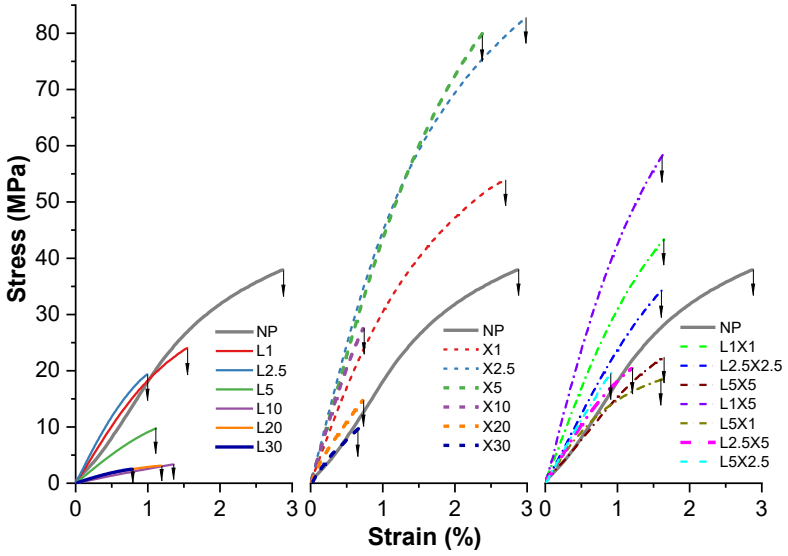

Figure 3.4. Tensile curves of nanopapers.

The characteristic tensile properties of elastic modulus, tensile strength, and strain have been summarized to compare single lignin and xylan fillers in Figure 3.5. Their hybrid materials (LX) are outlined as surface charts in Figure 3.6. Both lignin and xylan reveal that adding L2.5 and X2.5 contents substantially increases specific elastic modulus, but xylan also contributed to increased specific strength values (Figure 3.5). At and above 5 wt% lignin loadings, samples show lower specific modulus values than neat CNP. 2.5% addition of Lignin and xylan to NPs showed a 2-fold increase and 1.8-fold increase for specific elastic modulus values. An increase in specific tensile strength was measured for the X2.5 and X5 samples, indicating a 1.3-fold increase compared to CNP.

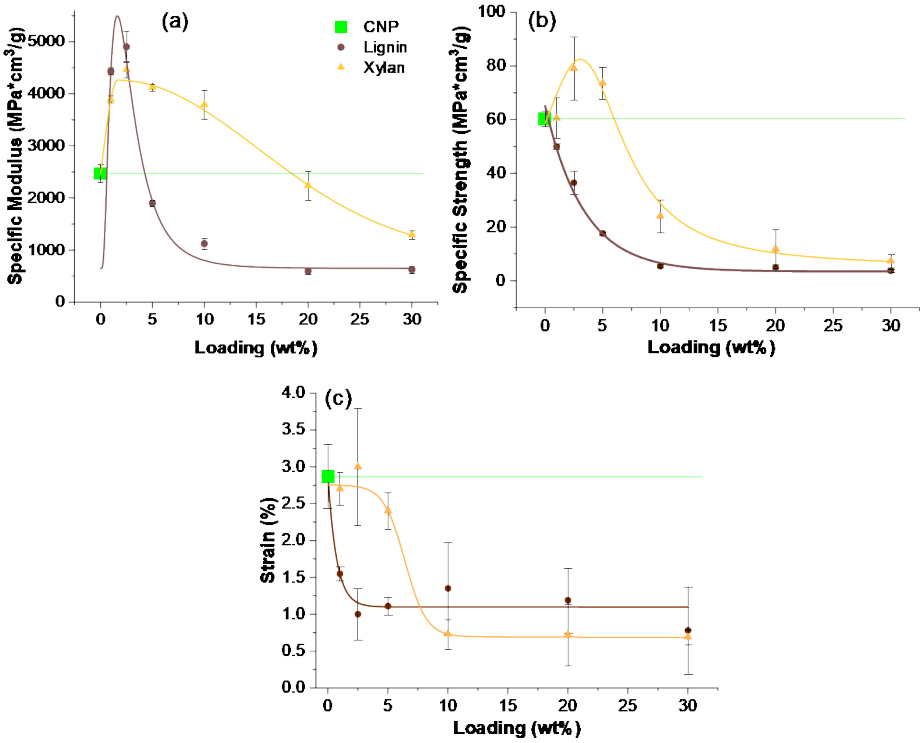

Figure 3.5. Tensile properties of cellulose nanopapers: specific elastic modulus (a), specific strength (b), and strain (c).

In addition, all four xylan compositions with loadings up to 10 wt% showed high specific modulus values, but further addition of xylan resulted in a drop for specific modulus values. The increase in tensile strength and elastic modulus could be explained by growth in the contact surface between fibrils, decreased voids, and overall porosity values, forming more hydrogen bonds and dense structures. Relatively shorter and more branched xylan molecules act as surface modifiers by increasing entanglement between NFC; thus, slippage between fibers during deformation is more complicated [127]. Increasing xylan content could yield phase separation between NFC as local agglomerates of cellulose nanoparticles are formed and evidenced by SEM [128]. These more soft xylan phase sections pose significantly lower mechanical strength, weaken the overall composite film, and explain the poor mechanical performance observed for X10, X20, and X30 samples. Lignin-modified NPs saw decreased specific strength values for all concentrations. This could be defined by introducing voids and structural defects observed in SEM images (Figure 3.2). While higher lignin particle concentrations similarly saw a further decrease as large particles developed voids and defects in the structure, which does not pose high mechanical properties. Elongation at the break for xylan samples with loading up to 5 wt% remained comparable to CNP, while higher concentrations saw decreased values. All lignin concentrations showed a significant decrease

in strain values from 3 % to around 1 % compared to CNP. The decline in elongation values is visible in a shorter plastic region, indicating that some compositions promoted fibril slippage.

Considering hybrid compositions, an in-depth comparison can be made for tensile properties. Using the experimental data as a basis, a response surface plot was constructed for each tensile characteristic to model component contributions (Supplementary 1). The experimental data obtained in testing were used to construct the second-order polynomial regression equation using the program EdaOpt [129]. The relationships between the design variables $x_i = (X_1, X_2)$ and the corresponding behavior functions Y_i are given as follows:

Specific modulus:

$$Y_{SM} = 3273+277\cdot X_1+555\cdot X_2-84\cdot X_1\cdot X_1-94\cdot X_2\cdot X_2-75\cdot X_1\cdot X_2, \quad (3.1)$$

Specific strength:

$$Y_{SS} = 64.63-18.19\cdot X_1+10.75\cdot X_2+1.83\cdot X_1\cdot X_1 -1.98\cdot X_2\cdot X_2-0.247\cdot X_1\cdot X_2, \quad (3.2)$$

Strain:

$$Y_S = 2.939-0.987\cdot X_1+0.02\cdot X_2+0.1147\cdot X_1\cdot X_1 -0.0213\cdot X_2\cdot X_2+0.04\cdot X_1\cdot X_2, \quad (3.3)$$

where X_1 and X_2 are the weight contents of the Lignin and Xylan, respectively.

Specific elastic modulus, specific tensile strength, and strain graphs (Figure 3.6) show the highest mechanical performance for samples modified with xylan from 2.5 to 5.0 wt% and up to 2.5 wt% added lignin. Surface charts also indicate that up to 1.0 wt% lignin can be added to retain relatively high specific strength and strain values, as other sections discuss the benefits of adding lignin. The strain at break values dropped strongly for hybrid compositions due to the lignin particles' impact on the structure. The optimal specific strength values were obtained for composition L2.5X2.5, which combines cellulose surface modification and densification by xylan, negating the formation of voids in the structure induced by adding lignin particles. Compared to single filler systems, the creation of bio-based hybrid compositions has been shown in the literature to obtain improved mechanical qualities in the fiber-fiber and fiber-particle compositions [130,131]. The specific elastic modulus was the only mechanical characteristic that improved from hybrid compositions containing 2.5 wt% xylan and lignin loadings.

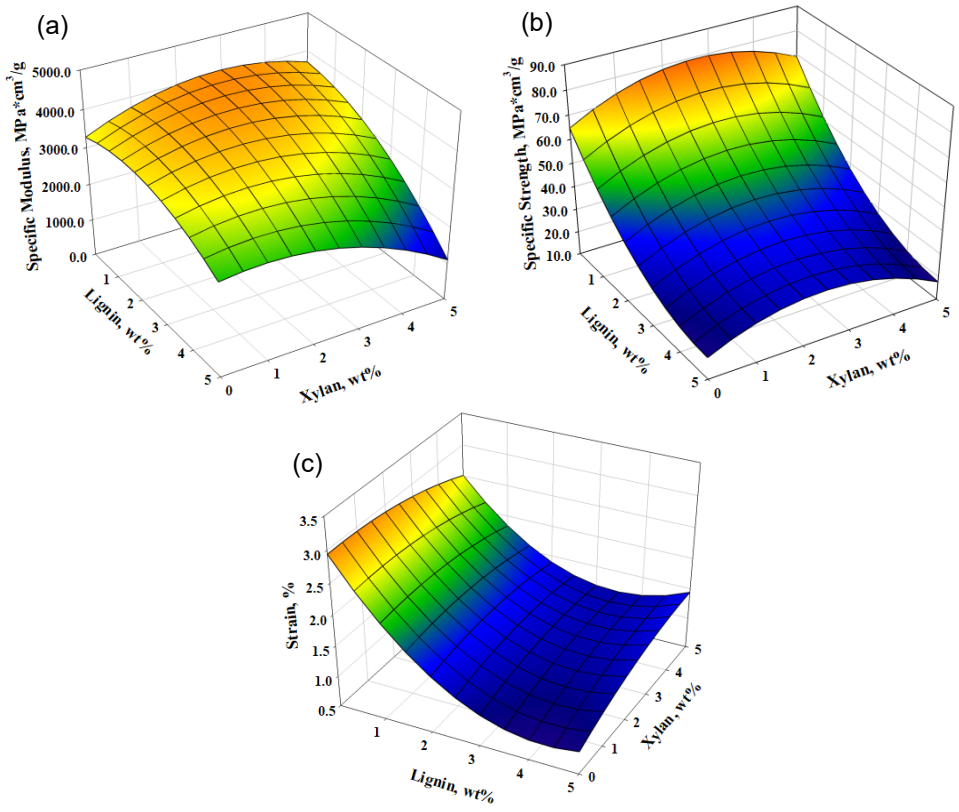

Figure 3.6. Response surface plots present the results obtained for (a) the specific modulus, (b) specific strength, and (c) strain of the nanopaper with different weight contents of Lignin and Xylan using the data obtained from regression equations.

3.1.3. Thermooxidative stability

Thermooxidative stability of the nanopaper and its composites was determined using thermogravimetric analysis with a heating rate of 10 °C /min under an oxidative air atmosphere. TGA and derivative weight loss of the prepared nanopaper composites have been shown in Figures 3.7 (a) and (b), respectively.

Lignin is known for its superior thermal stability over other cellulose-based nanoparticles. It is often used for thermal stability enhancement [132,133]. As shown in Figure 3.7, lignin has the highest thermal stability, but in the case of nanopapers, significant enhancement was not observed before the maximum degradation temperature. Xylan has been identified as the thermally most unstable component of lignocellulose, with the primary degradation step between 200 and 370 °C attributed to side-chain unit decomposition, while cracking of the xylan chain backbone is attributed to peak and shoulder with maximum thermal destruction temperature (T_{max}) 250 and 296 °C, respectively [134]. Figure 3.7(b) coincides with the literature [134], where the main T_{max} for xylan powder is the lowest (250 °C). However, the char

combustion temperature for xylan appears to be the highest (526 °C). The observations in Figure 3.7(b) and Table 3.1., where the highest T_{max} is 327 °C for CNP, align with the literature [135,136].

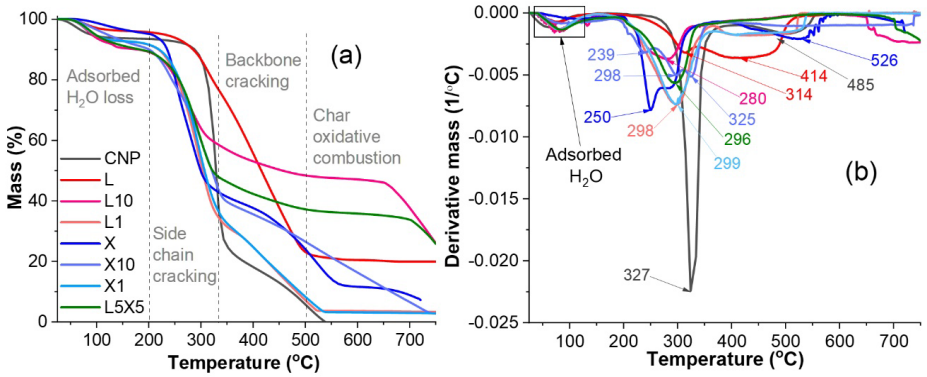

Figure 3.7. TGA mass (a) and the derivative mass (b) of cellulose (CNP), lignin (L), xylan (X), and hybrid (LX) nanopapers.

The weight loss for all samples starts with the evaporation of adsorbed water, and the temperature range up to 200 °C is commonly attributed to this process [132,137]. Depending on sample composition, the adsorbed water amount has been from 4 to 10 wt%. This phenomenon could be attributed to an additional covalent linkage between lignin and cellulose fibrils [133] that bind with -OH groups; the same goes for xylan. Therefore, less water is absorbed. Thus, the introduction of xylan and lignin has reduced the hydrophilicity of the NPs and increased their initial thermal stability.

Reportedly, the primary degradation of NFC happens from 206 to 381 °C when adsorbed water has already been evaporated [132,138]. The cellulose pyrolysis model says that cellulose melts at a range of 200 to 280 °C, and then the formation of dehydrogenated cellulose happens, followed by strong cellulose depolymerization [132,138]. Figure 3.7 shows similar three-step thermal degradation of the CNP; heating to 200 °C removes adsorbed water, then approximately up to 330 °C next steps of cellulose melting and dehydrogenation occur, followed by strong depolymerization, leaving around 20 wt% of the sample left. Thermal degradation after 330 °C is almost a separate degradation step, not reported when an inert nitrogen atmosphere is used [132]. This leads to a much lower char yield of the NPs due to the thermal oxidation of the char in the range of 440 to 580 °C [139]. Adding L and X decreases maximum degradation temperature (thermal stability) by 29, 47, 28, 2, and 31 °C for L1, L10, X1, X10, and L5X5 composites respectively. Changes in structure affected moisture absorption and significantly contributed to observed differences. L10 composition with a remaining 50 wt% showed superior thermal stability. Table 3.1 shows that lignin addition increases char yield by 1 and 22 wt% for L1 and L10 composites.

Table 3.1.

Thermal degradation characteristics of cellulose nanopapers

Sample	Onset degradation temp. (°C)	Maximum degradation temp. (°C)	Char yield (wt%)
CNP	268	327	0
L	182	414	20
X	207	251	7
L1	154	298	3
L10	176	280	24
X1	225	299	3
X10	198	325	3
L5X5	188	296	24

3.1.4. Thermal conductivity

Table 3.2 summarizes NPs density, diffusivity, activation energy (E_a), and inherent conductivity value (λ_0). It has been proposed that the pore size in NPs is too small for air to participate in heat conduction; thus, cellulose crystal orientation and interfacial bonding strength play a significant role in thermal conductivity parameters [140,141]. The film casting process resulted in non-aligned NPs, eliminating anisotropy for thermal properties. The formation of interfaces can be expected from the density of prepared NPs (Table 3.2). The addition of 1 wt% lignin decreased density to 0.48 g/cm^3, the lowest value observed from prepared NPs.

While loading more lignin increased density value, they remained comparable to CNP. As discussed in the morphology section, lignin resulted in various defects like voids, which contributed to higher porosity and lower density values. While, as proposed before, xylan is a shorter, more branched molecule that can fill gaps between NFC networks and increase interfacial bonding, this is reflected as a loss of porous structure (Figure 3.2) and significantly increased density in rage from 0.89 to 1.36 g/cm^3 showing 1.4 to 2.2-fold increase compared to CNP. The changes in thermal conductivity coincide with density changes (Figure 3.8), as NPs with higher density show higher values. The L10 sample and L30 samples show slight deviations from predicted changes. Two conflicting effects could explain it. The formation of larger irregular voids reduces density. Lignin particle packing between NFC fibrils enhances thermal conductivity. The addition of xylan has been found to show around a 3 to 4-fold increase in thermal conductivity, while even high loadings of lignin did not exceed a 2-fold increase. The L1 sample showed the lowest thermal conductivity between NPs in all measured temperatures. Hybrid compositions inherited thermal properties identical to samples modified only with lignin. This indicates that lignin intervenes with xylan dispersion and the formation of interfacial bonding. Thermal conductivity slightly increased when measurements were performed at a higher temperature. This is commonly explained by the rise in phonon conduction for solids that are not metals.

Table 3.2.

Density, diffusivity (at 25 °C), specific heat (at 25 °C), activation energy E_a and inherent conductivity value λ_0 of cellulose nanopapers

Sample	Bulk density (g/cm^3)	Diffusivity (mm^2/s)	λ_0 (W/(m·K))	E_a (kJ/mol)
CNP	0.63 ± 0.06	0.091	0.27	3.59
L1	0.48 ± 0.03	0.096	0.22	3.61
L2.5	0.52 ± 0.03	-	-	-
L5	0.55 ± 0.03	-	-	-
L10	0.61 ± 0.05	0.167	0.42	4.01
L20	0.63 ± 0.04	-	-	-
L30	0.66 ± 0.07	0.142	0.22	1.89
X1	0.89 ± 0.06	0.099	0.51	2.64
X2.5	1.05 ± 0.04	-	-	-
X5	1.09 ± 0.03	-	-	-
X10	1.14 ± 0.04	0.180	2.73	6.81
X20	1.24 ± 0.04	-	-	-
X30	1.36 ± 0.03	0.161	1.16	3.93
L1X1	0.64 ± 0.04	0.076	0.50	5.54
L1X5	1.01 ± 0.04	-	-	-
L5X1	0.6 ± 0.03	-	-	-
L2.5X25	0.69 ± 0.05	-	-	-
L2.5X5	0.99 ± 0.02	-	-	-
L5X2.5	0.79 ± 0.04	-	-	-
L5X5	0.89 ± 0.03	0.103	0.49	4.90

Thermal diffusivity changes can be attributed to adsorbed water content, indicated by TGA (Figure 3.7), and chemical groups on fiber surfaces [142]. Thus, it can be assumed that branched hydrophilic xylan molecules would promote water adsorption compared to more hydrophobic lignin. This is reflected in Table 3.2, where all compositions based on xylan show a significant increase in diffusivity values. The best comparison can be made with X1 and L1 samples, where xylan NP shows a 2-fold increase and lignin NP shows almost no change in thermal diffusivity compared to CNP. The high content of modifiers introduces various structural defects that negate the water adsorption effect, and surface groups strongly influence thermal diffusivity. This could explain a significant increase in diffusivity values for L10 and X10 NPs.

In contrast, a subsequent decrease in values for X30 and L30 NPs could be attributed to substantial structural changes in NPs. Thermal diffusivity did not show strong temperature dependence. The thermal conductivity of the X10 and X30 NP samples could be attributed to the formation of separate (new) phases in higher concentrations, while X1 xylan acts more as a cellulose surface modification agent.

Figure 3.9 was used to determine E_a values utilizing the slope of the approximate straight lines in the Arrhenius plot. While λ_0 was calculated from the Arrhenius equation using the method described in [143]. The activation energy indicates the role of distributed nanoparticles in NPs for composite insulation properties as another layer blocks or promotes heat transfer [144]. Thus, λ_0 and E_a values depend on the nanoparticle's nature or formed agglomerates or layers in case of high loadings. Table 3.2 indicates a 1.9-fold decrease of activation energy was achieved for the L30 sample, while X10 saw a 1.9-fold increase. E_a did not show a strong correlation with thermal conductivity, but this can be explained by significantly altered microstructure. Most of the sample's activation energy increased similarly to thermal conductivity and diffusivity. Lignin compositions showed either negative trends or similar results to CNPs.

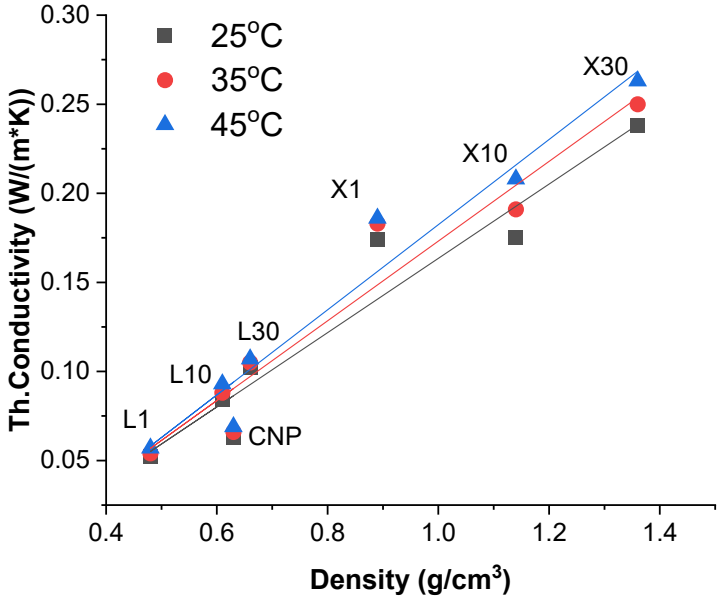

Figure 3.8. Thermal conductivity vs. bulk density of cellulose (CNP), lignin (L), and xylan (X) nanopapers.

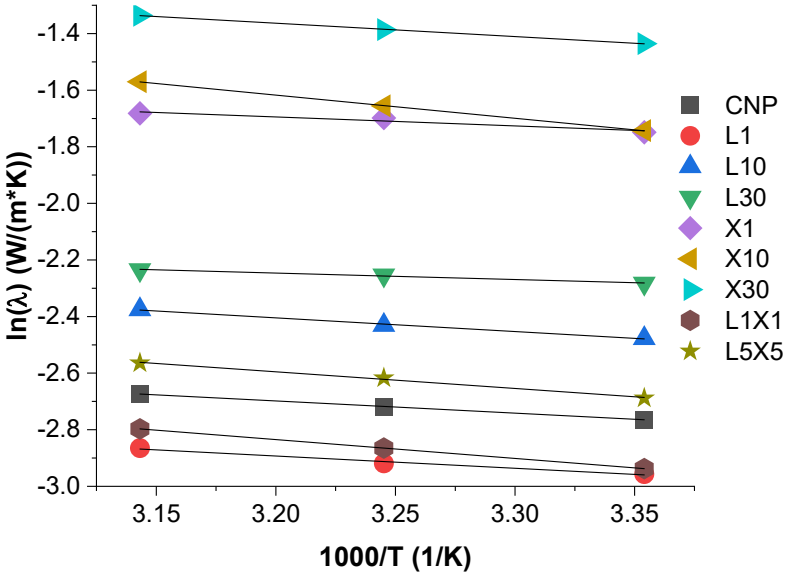

Figure 3.9. Arrhenius plot: dependence of thermal conductivity on temperature for cellulose (CNP), lignin (L), xylan (X), and hybrid (LX) nanopapers.

3.1.5. Summary

Wastepaper has huge potential to be an excellent source for nanopaper production and fits the circular economy goals. It should be noted that in addition to cellulose, wastepaper can also contain several impurities such as inorganic fillers, glues, pigments, laminated polymers, which greatly complicates recycling and the technological process of extracting pure cellulose. Water suspensions have a significant advantage over other studies implementing various organic solvents. Using lignin and xylan solutions for nanopapers shows multiple benefits as they act more as surface modification agents. Their high loadings are disadvantageous due to phase separation and the heterogeneous structure of these nanopapers. Lignin introduces defects and heterogeneous elements, while xylan fills gaps between cellulose fibrils to create a more homogenous system. The structural changes induced by adding xylan reduce light scattering and yield transparent nanopaper. Defects caused by lignin remain in the structure, while xylan seems to lower the size of formed voids and isolate them. The use of lignin can increase stiffness, resulting in decreased tensile strength and elongation values. The densification of the structure leads to an increase in thermal conductivity. The obtained nanopaper with tunable morphology has shown great perspectives as packaging materials and filters. They would also benefit from developing clean manufacturing routes from waste sources.

3.2. Lignin and xylan as interface engineering additives for improved environmental durability of sustainable cellulose nanopapers

Environmental factors such as light, temperature, and humidity frequently affect cellulose materials and products. Simulated UV irradiation, heat, and moisture exposure were comprehensively used to characterize cellulose nanopaper tensile properties changes. For the preparation of NP, high-purity cellulose from old, unused filter paper waste was used. Lignin and xylan were used as sustainable green interface engineering modifiers for NP due to their structural compatibility, low price, nontoxic nature, and abundance as a byproduct of biomass processing. As well as their ability to protect cellulose fibers from UV irradiation. Nanofibrillated cellulose suspension was obtained by microfluidizing cellulose suspension, and NP was produced by casting films from water suspensions. The use of filler from 1 to 30 wt% significantly altered NP properties. All nanopapers were tested for their sensitivity to water humidity, which reduced mechanical properties from 10 to 40% depending on the saturation level. Xylan addition significantly increased the specific elastic modulus and specific strength by 1.4- and 2.8-fold, respectively. Xylan containing NPs had remarkable resistance to UV irradiation, retaining from 50 to 90% of their initial properties. Lignin-modified NPs resulted in a decreased mechanical performance due to the particle structure of the filler and the agglomeration process, but it was compensated for by good property retention and enhanced elongation. The UV oxidation process of the NP interface was studied with UV-Vis and FTIR spectroscopy, which showed that degradation of lignin and xylan preserves cellulose fiber structure. Scanning electron microscopy images revealed the structural formation of the interface and supplemented the understanding of UV ageing impact on the surface and penetration depth in the cross-section. The ability to overcome premature aging in environmental factors can significantly benefit the wide adaptation of NP in food packaging and functional applications.

3.2.1. UV irradiation and heat effect on the tensile properties

Figure 3.10 depicts sample stress-strain curves, and Figure 3.11 illustrates tensile properties for UV-irradiated samples. For the reference samples, the effects of lignin and xylan modifiers can be examined for their tensile properties, which indicate that the addition of xylan enhances all tensile properties. In contrast, lignin reduces the elastic modulus and tensile strength but increases the elongation at break values (Figure 3.11). The addition of xylan to CNP showed an increase in NPs properties even with high loading up to 20 wt% for the specific elastic modulus and specific tensile strength, achieving up to 1.4-fold and 2.8-fold improvements, respectively. Elongation values reach a maximum value at 10 wt% xylan loading, showing a 2.8-fold improvement compared to CNP. In comparison, lignin addition resulted in a 2.6-fold increase in the elongation values, while specific elastic modulus exhibited a 1.1 to 3.6-fold decrease for lignin content up to 10 wt%. Specific tensile strength showed similar values to CNP with loadings up to 5 wt% lignin, but further addition resulted in almost a 2-fold decrease.

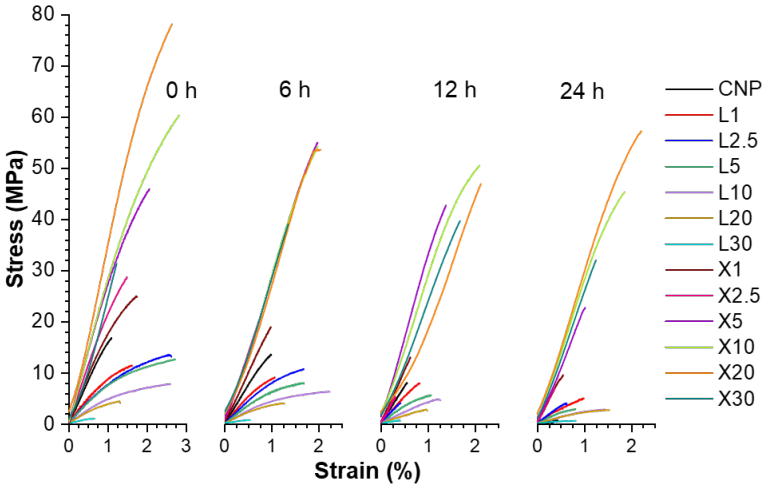

Figure 3.10. Representative stress-strain curves of NP for pristine and aged samples at different times of UV irradiation at 80 °C temperature.

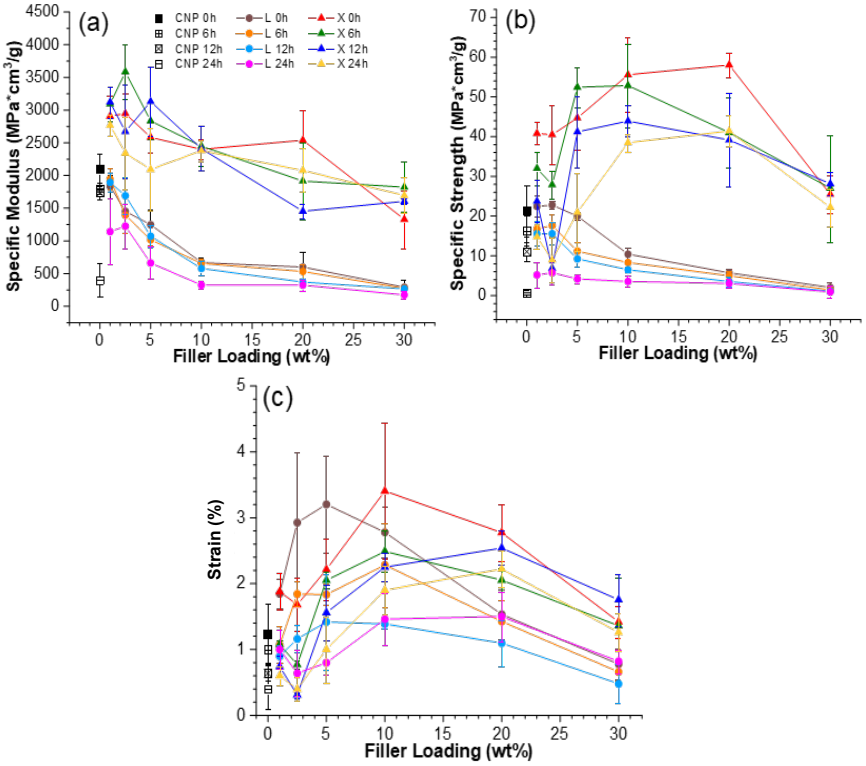

Figure 3.11. Tensile properties: (a) specific elastic modulus, (b) specific ultimate tensile strength and (c) elongation at break for nanopapers before and after exposure to intensive UV irradiation at 80 °C.

At higher lignin loadings, samples were fragile and showed a further drop in properties. It was observed that modifier loading of 10 wt% corresponds to the xylan critical threshold concentrations for the developed interface structure. It could be explained that the biopolymer phase was segregated at higher loadings, while a single highly enhanced interface was produced with 2.5 wt% of lignin and 10 wt% of xylan modifier concentrations. For example, adding 2.5-10 wt% of xylan could result in complete cellulose surface modification, i.e., coating.

Berglund et al. reported that hemicelluloses could control cellulose fibril aggregation and complement interface with a combination of rigid and flexible interactions [74]. While at high loadings, segregated xylan biomolecules can form separate bulk interphases characterized by flexible molecular chains. Filler concentration at 10 wt% reaches critical threshold content values for a noticeable shift in different structural interactions. This is expressed as an almost linear increase of 2.5 to 10 wt% loadings for several affected compositions.

Kontturi et al. compared NFC NPs to bacterial cellulose (BC) NPs and found that their only difference was the presence of hemicellulose in the interface between the fibrils of NFC and no hemicellulose for BC [145]. The authors reported that NFC NPs had higher mechanical properties and concluded that hemicellulose significantly improves the interface adhesion between individual fibrils. As xylan is a type of hemicellulose with a more branched structure, it can form more hydrogen bonds on the interface, acting as an efficient glue and improving overall mechanical properties. It has also been reported that xylan NPs have much lower mechanical properties than cellulose NPs [123,146]. Thus, at higher loadings like the X30 sample, the cellulose fibril network is disrupted significantly, reducing mechanical properties. Similar observations about hemicellulose interface “glue” properties have been reported by other authors [127,128]. In comparison, the lignin remains as particles, forming the segregated interphase in the NP films. The distorted NFC mesh networks decreased interface adhesion and mechanical performance of those lignin NP samples.

UV-irradiated CNP showed a catastrophic decrease in properties, and after 24 hours of UV exposure, its properties were the lowest of any NP. The literature has reported that cellulose is very unstable in UV light without stabilization additives [147-149]. The aged xylan NP samples demonstrated a shift to lower filler loadings that achieved the best properties. For xylan NPs, the best values after aging were for loadings from 5 to 20 wt%. Lignin-modified NPs showed a slight increase in elongation values and decreased elastic modulus and tensile strength compared to CNP. In addition, it was also observed that xylan loadings up to 5 wt% benefited from exposure to UV, resulting in the stiffening of NP. Figure 3.12 shows a proposed visual schematic illustration of the oxidation process at the interface of the obtained NPs. The illustration is used to complement the following discussion and UV-vis section.

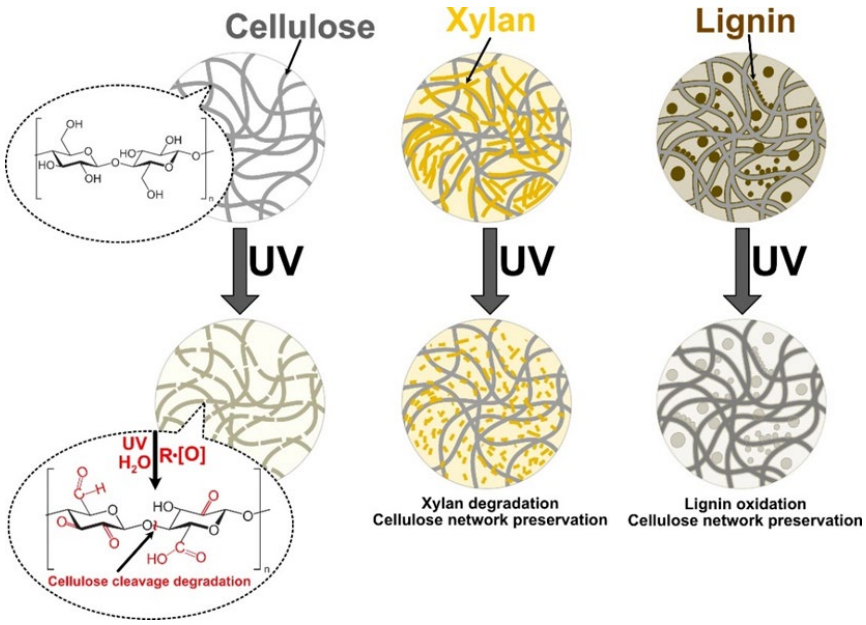

Figure 3.12. Visual representation of the oxidation process.

The increase in the elastic modulus was observed for an exposure time of 6 hours and partly for 12 hours. This could be directly related to thermal oxidation and degradation processes, supported by a visible decrease in elongation values. Thus, smaller, more rigid sections are formed. As xylan fills gaps between cellulose fibrils, adsorbs and protectively coats their interface (Figure 4), the aging process shifts more from volume to the interface, enhancing the materials' durability [150]. In addition, it is known that more branched and lower molecular weight biomolecules degrade before cellulose [151,152]. A significant property decrease was obtained for lignin NP after 24 hours of UV exposure, while a milder effect was obtained after 12 hours. We observed that after 12-hour irradiation, a critical time was reached for the inhibition of the thermal oxidation process in modified nanopaper. At 24 hours, the modifiers do not fully shield the cellulose fibers from UV light; the cellulose degrades intensively. It is observed as a drop in stiffness and strength. The xylan NP showed a remarkable ability to retain most of its properties after UV irradiation, which is related to the stabilization effect of the modified NP.

The changes were also visual (Figure 3.13), as NP samples with longer exposure times had their color shift to a darker brown than reference samples. The color shift was very pronounced for xylan NP and correlated with higher xylan content. The high intensity of UV radiation oxidized oxygen to ozone, which assisted in the sample oxidation process. The oxidation process creates radicals that can induce chain scission, thus reducing components' molecular weight and mechanical strength [153]. In addition, heat exposure has been reported to induce chain relaxation, promoting cellulose crystallization and the reformation of hydrogen bonds [154]. Thus, two opposing effects take place during the sample's exposure to UV and heat.

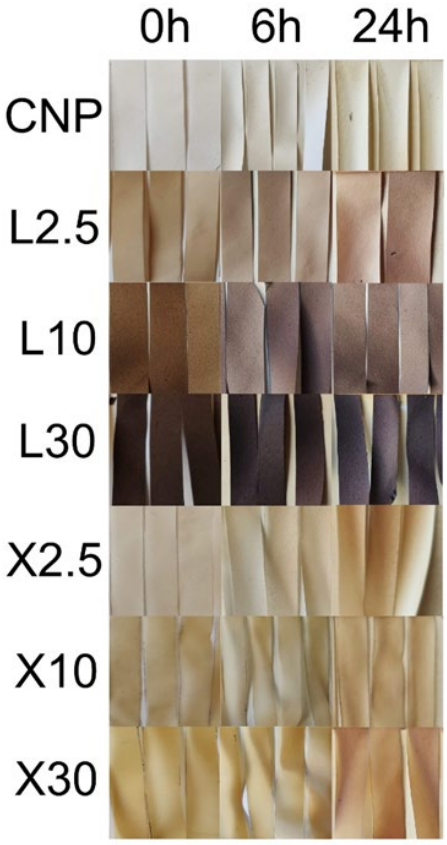

Figure 3.13. The visual appearance of NP before and after exposure to intensive UV irradiation at 80 °C.

3.2.2. Structural analysis

Figure 3.14 shows a typical scanning electron micrograph of selected NP compositions. SEM images revealed closely packed cellulose fibrils with an interconnected network that showed visible porosity and no structural deformations. The introduction of lignin in L5 NP shows that a small layer of lignin nanoparticles has been accumulated on the surface of cellulose fibrils and in the previously visible pores. The addition of lignin has contributed to visible layer delamination and the formation of microscale voids. This explains the decreased mechanical performance observed for lignin NP. The L30 NP SEM images reveal a strongly disrupted cellulose fibril network with a chaotic structure that includes large voids. In high loadings, lignin appears to thoroughly coat cellulose fibrils, contributing to a significant decrease in hydrogen bonding between fibers and a subsequent drop in mechanical properties. While the lignin NP structure revealed the inherent issue of compatibility between components, it also yielded unique changes in structure. These voids could be used to deliver biologically active components for wound treatment [155].

In contrast, the addition of xylan to CNP showed a densely packed structure with no visible pores or voids in the structure of X10. Our observations coincide with the literature, where xylan shows the ability to fill gaps between cellulose fibers and improve properties in low loadings [75,156]. The smaller molecular weight and more branched structure contribute to xylan's ability to insert itself into gaps between cellulose fibers and coat them. In addition, xylan effectively enhances the hydrogen bond network of cellulose, thus, there is no visible separation between xylan and cellulose in X10 NP. At the same time, X30 NP shows clear phase separation, and xylan forms visible interphase layers. Individual cellulose fibrils are almost indistinguishable, while the highly dense structure remains. Thus, thick interphase layer formation results in poor mechanical performance due to disrupted load transfer in the cellulose network [124,157]. Xylan's ability to form dense structures with no visible pores could be used to improve gas barrier properties by adding or coating [123].

The surface morphologies of unaged and aged NP have been studied by SEM (Figure 3.15). The 24-hour irradiation and heat treatment were chosen to maximize differences between the compositions. The unaged NP surface yields similar observations to those previously discussed above. Before aging, all NPs showed a relatively smooth surface with interconnected cellulose fibers. After aging, the CNP surface becomes very rough, and individual fibers become more pronounced, which indicates that small fibrils connecting large fiber formations have degraded. The observed catastrophic failure of mechanical performance properties reflects the loss of interconnected fibre networks. The higher magnification images provided in supplementary (Supplementary 2 and Supplementary 3) reveal intensive cracking of cellulose fibers. Cracking indicates the breaking of (1→4) β-glycosidic bonds, effectively reducing the molecular weight of cellulose [158,159]. In addition, cracks serve as stress concentrations that contribute to low tensile properties after UV aging.

The L5 NP, after aging, shows a rather interesting change with the introduction of small holes throughout the surface. The interconnected network of cellulose fibers is severely damaged, but it remains in better condition than CNP. Lignin particles could coat cellulose fibers and significantly reduce the cracking due to efficient irradiation absorption as indicated by higher magnifications in the supplementary (Supplementary 2 and Supplementary 3). Overall L5 composition follows a similar route to CNP, with the drastic increase in surface roughness and separation of individual fibers. Lignin could not last full 24 hours and seemed to fail between 12 and 24 hours as indicated by tensile tests. In the case of xylan NP, it can be observed that the surface remained relatively smooth, with the top layer experiencing significant degradation, revealed by no visible fibers in the aged surface. This could be explained by cellulose and xylan degradation products remaining on the surface and forming a protective layer.

The depth of UV irradiation damage can be seen in Supplementary 4. CNP had almost complete penetration with UV, significantly damaging the cellulose fiber network, seen as a loss of dense structure. The L5 crosscut showed a much lower penetration depth compared to CNP. While the smooth surface of the L5 composition has degraded, the damage has been contained close to the surface. Similarly, the X10 composition preserved the structural integrity of CNP and limited UV structural damage to the surface of NP. The surface of X10 has a

disrupted structure, and a visible difference is seen as an almost different layer for the exposed surface.

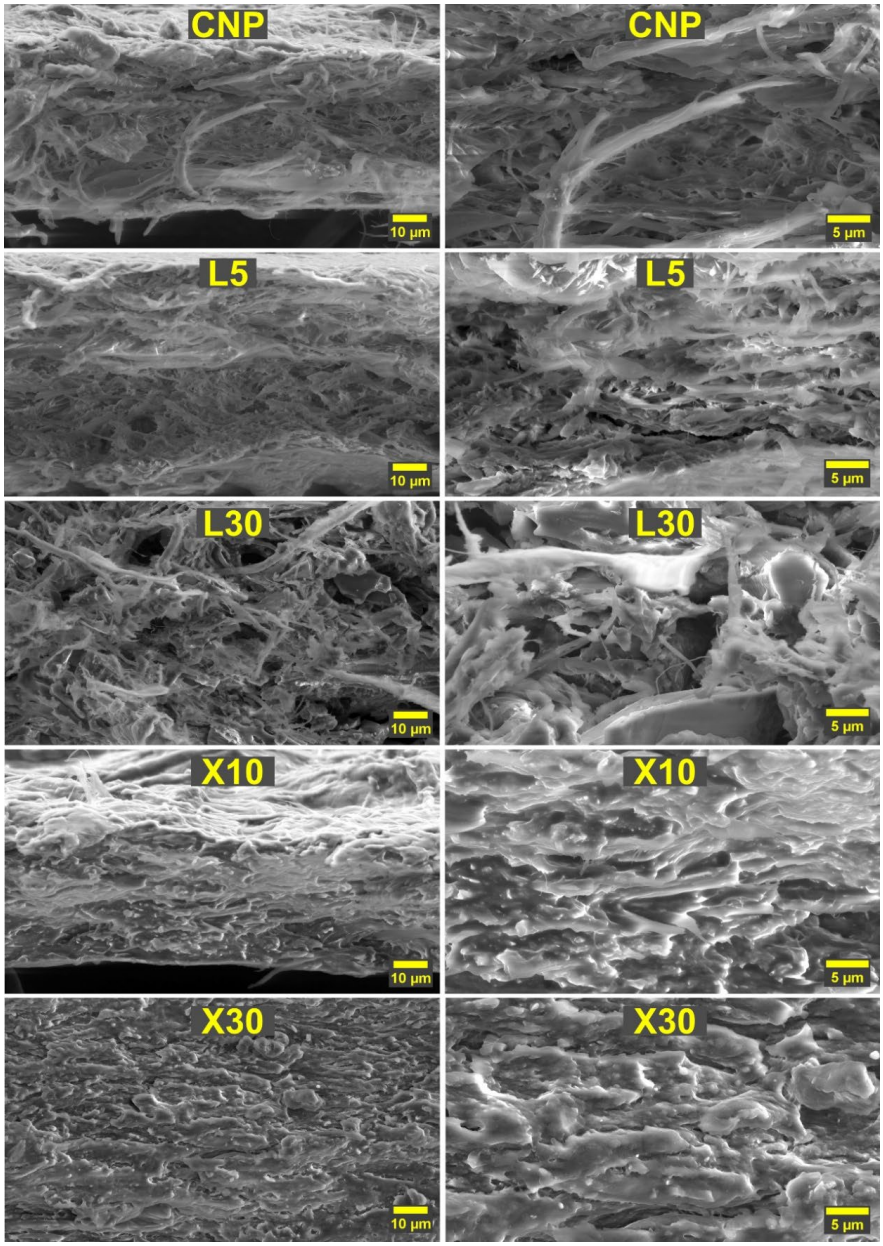

Figure 3.14. Cross-section scanning electron micrographs of selected NP compositions.

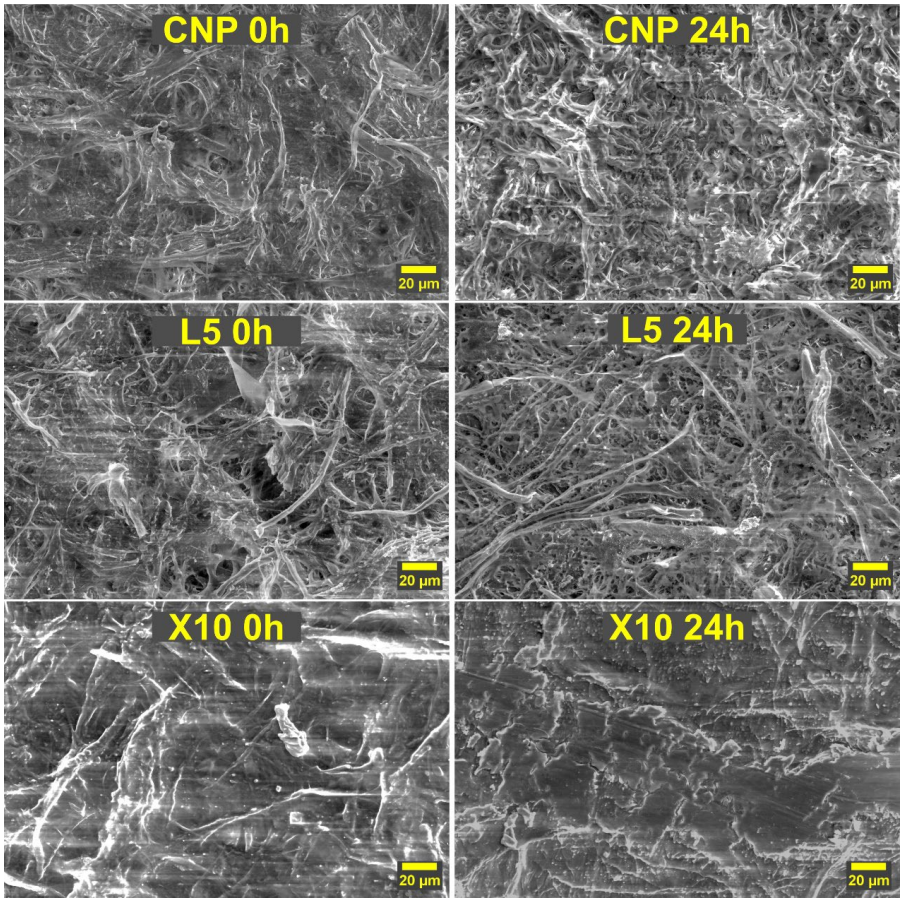

Figure 3.15. The impact of 24 hours of UV irradiation on the surface morphologies of selected NP compositions.

3.2.3. UV-VIS and FTIR spectroscopy

As shown in Figure 3.13, UV-VIS spectroscopy takes advantage of induced color changes in NPs after aging them in UV irradiation and heat. The presence of oxidizable groups results in color change [160,161]. Visual changes show CNP changed color from white to white with a yellow tint, brown lignin NPs experienced whitening, and xylan NPs changed from yellow to a light brown color. This loss of color (whitening) for cellulose materials has been reported in the literature and indicates lignin degradation [162-164]. The yellow tint observed for CNP indicated oxidation of cellulose [165,166].

The absorbance spectra of tested NPs are shown in Figure 3.16. The spectra are relatively simple and have absorbance at around 280 nm for all compositions and an extended absorbance up to 600 nm for lignin NPs. The absorbance from 250 to about 350 nm is relatively weak for Xylan NP and CNP before UV exposure. No absorption peaks in visible light are seen for CNP and xylan NP, which indicates a lack of chromophore groups in xylan and cellulose structures. After aging, there is a visible shift to around 300 nm and an increase in absorption intensity.

This is attributed to the formation of various cellulose and xylan oxidation products, like carbonyl, aldehyde, and carboxyl groups [149]. This is observed as a loss of whiteness for these NPs.

UV-vis spectra indicate the increase in lignin concentration. Lignin is known for its aromatic structure, which contains mainly conjugated double bonds, which show very high absorbance in UV-vis spectra compared to non-conjugated double bonds [148]. Lignin NP spectra (L10 and L30) show a decrease in absorption intensity, which is the opposite of CNP and xylan NP observations. This is commonly explained as a breakdown of the lignin structure (formation of low molecular weight compounds), resulting in a decrease of conjugated systems [167]. Lignin acts as a barrier to the UV light that protects cellulose in natural structures like wood and plants [168]. Protection from UV is achieved by absorption of light and degradation of lignin's structure.

In the case of L2.5, UV degradation results are comparable to CNP, indicating that lignin cannot effectively shield UV rays from cellulose fibers at this concentration due to the non-homogeneous coating of cellulose fibers. The absorption of xylan NPs drops significantly above 350 to 400 nm when compared to CNP. This confirms that xylan effectively coats the surfaces of cellulose fibers, thus reducing the absorption of visible light.

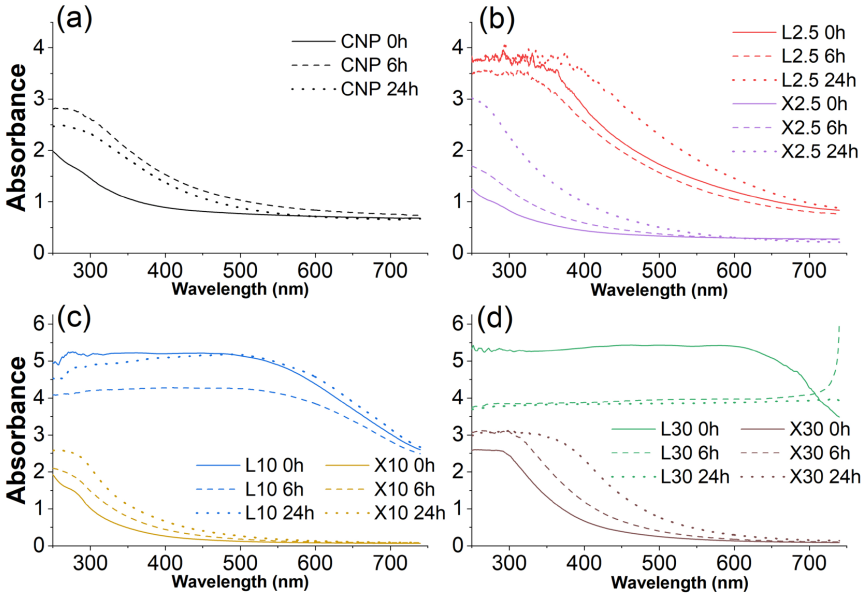

Figure 3.16. UV-vis spectra of NPs before and after aging 6 h and 24 h: (a) CNP, (b) L2.5 and X2.5, (c) L10 and X10, (d) L30 and X30.

Figure 3.17 shows the FTIR spectra of NP samples before and after 24 h of UV irradiation, while Table 3.3 summarizes the absorption band assignments. L5 and X10 samples were selected for the FTIR analysis due to their mechanical property preservation compared to CNP. The spectra for CNP show the highest absorption at 1000 to 1100 cm^{-1} region, indicating

characteristic cellulose peaks for C-O linkages. The addition of lignin reduces the intensity of these peaks, indicating partial surface coating. At the same time, lignin aromatic ring C=C double bond stretching (7) is introduced in the L5 spectra [169]. In contrast, adding xylan alters the characteristic double C-O peak intensities and introduces a new C-O peak at 976 cm^{-1}, which is commonly used for xylan identification [170]. Both modifiers influenced the -OH group absorption, further proving changes in surface structure and hydrogen bond formation.

After 24 hours of aging, CNP showed a significant decline in tensile properties, which is reflected in the decreased absorbance of C-O and C-O-C groups. The mechanical properties of cellulose are mainly determined by the ability to form hydrogen bonds and molecular weight [171]. As C-O-C cleavage occurs, the molecular weight of cellulose is reduced, while the reduction in C-O absorbance could be attributed to surface oxidation. In addition, a new peak (5) representing C=O is observed in the CNP spectra, testifying to the surface oxidation process.

In the L5 composition, the absorbance of characteristic cellulose peaks increases after aging. This could be attributed to the breakdown of lignin, which coated the surface of cellulose fibers and is supported by the shift observed for C=C peak absorbance (7) and matches the data from the literature, where lignin degradation leads to the breakdown of the structure and conjugated double bond systems [167]. Thus, a shift to lower conjugation of double bonds is seen as a shift in the absorbance peak. The loss of the characteristic lignin peak at 837 cm^{-1} on the surface further proves lignin degradation.

The absorbance intensity for X10 NP almost halved after 24 h of UV irradiation, indicating significant structural degradation. Although SEM analysis (Figure 3.14) shows that xylan effectively coats cellulose fibers, the literature has reported that xylan has poor UV resistance [172]. There are no visible indications of FTIR spectra changing to match with cellulose, indicating that degradation is partial and degraded xylan remains on the surface of NP. Thus, while xylan significantly degraded, the rigid cellulose fibers were mainly protected, as indicated by the tensile properties. The FTIR observations match the visual changes, where CNP and xylan NPs showed visible signs of oxidation while lignin degraded and lost its distinct brown color. Similarly, xylan samples had the highest decrease in absorbance spectra and the most pronounced color shift after UV aging.

Table 3.3.

Assignments of the infrared absorption bands

Band	Wavenumber (cm^{-1})	Assignment	Reference
1	3333	Intramolecular hydrogen bonding of -OH group	[173]
2	3276	Intermolecular hydrogen bonding -OH group	[173]
3; 4	2915, 2850	CH symmetrical and asymmetrical stretching	[173]
5	1738	C=O stretching of acetyl or carboxylic acid in hemicellulose	[162]
6	1640	C=O stretching in the carboxyl group	[174]
7	1582-1560	C=C stretching of lignin aromatic ring	[169]
8	1458	CH bending of Xylan	[170]
9	1427	CH_2 scissoring	[173]
10	1372	C-H bending	[173]
11, 22	1315, ~700	CH_2 rocking	[149,173]
12, 13, 15, 16, 17	1242, 1202, 1110, 1055, 1030	C-O stretching	[170,173,174]
14	1160	C-O-C asymmetric bridge	[162]
18	976	C-O stretching in Xylan	[170]
19	895	β-Linkage of cellulose	[173]
20, 21	837, 776	C-H out of plane deformation in lignin aromatic ring	[170,175]

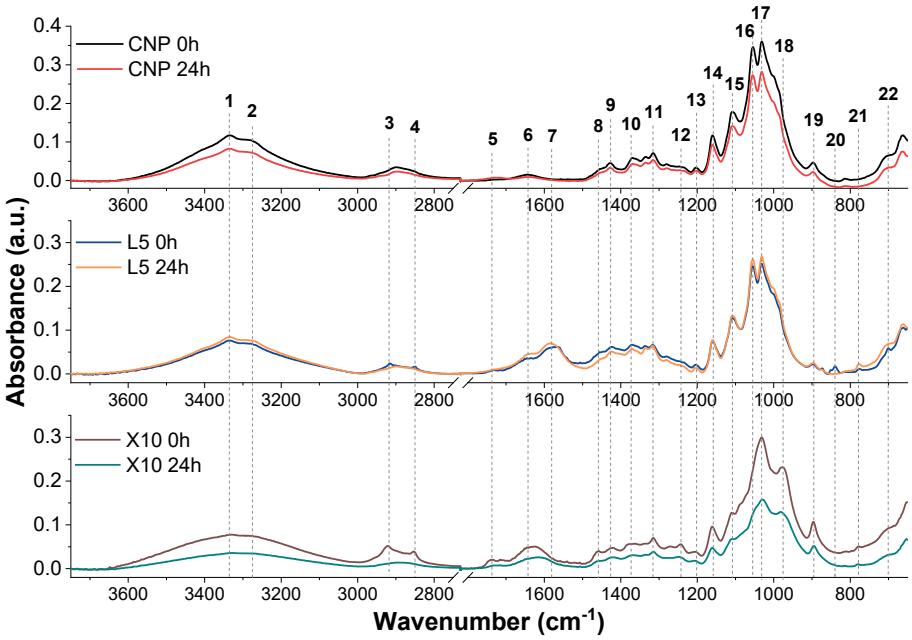

Figure 3.17. FTIR spectra of CNP, L5 and X10 samples before and after 24h UV irradiation. The FTIR region between 1800 and 2800 cm-1 is emitted because it lacks any significant bands.

3.2.4. Moisture effect on the tensile properties

The hydrophilic nature of cellulose-based materials results in highly sensitive properties to humidity variations. This should be considered when evaluating their performance properties. The equilibrium moisture contents w_∞ for all measured compositions are listed in Table 3.4. The amount of absorbed moisture in CNP and modified NP films significantly increases with RH. For CNP, the increase in w_∞ is about 26% (from 2 to 28%) for samples conditioned at RH24% and RH97%, respectively. The moisture absorption capacity of lignin-modified NPs is significantly higher: w_∞ of L5 and L10 samples conditioned under RH97% exceeds 70%. Xylan NP compositions demonstrate up to a 40% weight increase, almost 2-fold lower than w_∞ for lignin-modified NPs.

Higher lignin concentration promoted moisture absorption, but the lowest concentration (X1) showed the highest absorption values in the case of xylan. The lack of synergy between cellulose and lignin particles resulted in agglomeration and phase segregation, which could explain the high moisture absorption for lignin NP compositions. Österberg et al. described the importance of particle shape and size for lignin composites to achieve good packing and mechanical and thermal properties [176]. This could explain high water absorption as the lignin phase could induce defects and cavities in the cellulose fiber mesh network by increasing the voids and the surface that interacts and absorbs moisture. Xylan is a more branched molecule than cellulose. Thus, more side chains contain many more OH groups that can form hydrogen bonds with cellulose and water.

In addition, hemicellulose (xylan) tends to fill gaps between cellulose fibrils, thus creating a denser interface coating under high loadings of up to 10 wt% [150]. In this regard, the low xylan concentration in the X1 and X2.5 samples contributes to significant enhancement of the NP interface. Still, unlike higher loadings, it cannot pack fibrils in such a dense manner. This is seen in the RH 75% and RH97% results, where X5 and X10 NPs are within the margin of error, but X1 has a significantly higher relative weight gain.

Samples with filler loadings of 20 wt% and 30 wt% showed a significant increase in water absorption capacity due to the disruption of the cellulose fiber mesh network, which dramatically affected the mechanical properties. Thus, they were not further analyzed. The higher moisture absorption capacity of lignin-modified nanopaper resulted in a more significant hygrothermal impact on the mechanical properties than CNP and xylan NP.

Table 3.4.

The moisture content at saturation for NPs measured at different RH.

Sample	**w_∞, %**		
	RH24%	**RH75%**	**RH97%**
CNP	2.1 ± 0.5	7.1 ± 0.6	28.0 ± 3.0
L1	2.2 ± 0.3	8.7 ± 0.4	55.6 ± 5.5
L5	2.3 ± 0.1	13.6 ± 2.0	73.8 ± 4.1
L10	2.9 ± 0.5	16.0 ± 3.5	76.6 ± 4.0
L20	2.5 ± 0.2	-	-
L30	2.6 ± 0.4	-	-
X1	2.2 ± 0.1	19.6 ± 1.0	42.6 ± 5.1
X5	2.3 ± 0.2	11.4 ± 0.7	31.7 ± 4.3
X10	2.5 ± 0.2	12.2 ± 1.2	34.4 ± 4.0
X20	2.4 ± 0.2	-	-
X30	2.3 ± 0.2	-	-

Tensile tests were conducted after stabilising the sample weight under three selected RH values: 24, 75, and 97%. A comparison of tensile properties in different RHs for NPs is presented in Figure 3.18. Moisture absorption greatly affected the mechanical behaviour of the NPs, resulting in a decrease in the elastic and strength characteristics with higher water saturation. Lignin-modified NPs are characterized by lower tensile properties and a higher sensitivity to moisture than the CNP. This results in a complete loss of operation properties of highly loaded lignin NPs, making these compositions almost unusable at high RH. The addition of xylan, on the contrary, improved the mechanical characteristics of CNP.

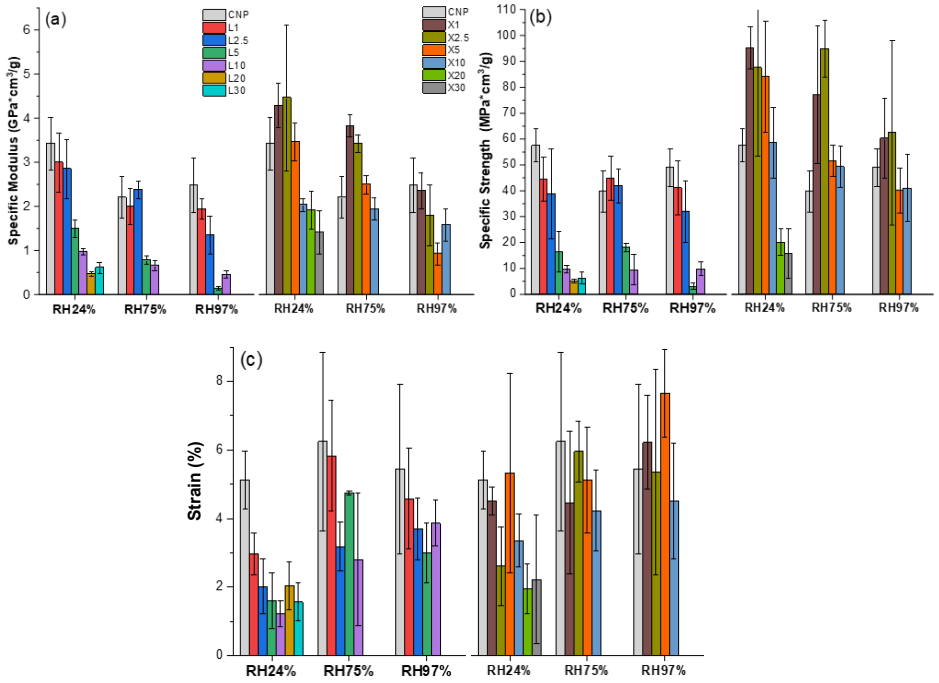

Figure 3.18. Tensile properties: (a) specific elastic modulus, (b) specific ultimate tensile strength and (c) elongation at break for NPs saturated under different RH.

Specific elastic modulus values increase by 32% and 55% for X2.5 NP compared to CNP at RH24% and RH75%, respectively. Absorbed moisture plasticized the material, although the elastic modulus and strength of moisture-saturated (RH 97%) xylan NPs are comparable to CNP. For lignin NPs, a decrease in the elastic modulus and tensile strength was observed. Correspondingly, Xylan NPs showed a remarkable 2.3-fold increase in specific tensile strength at RH 75% for X2.5 composition. Tensile strength was comparable to CNP at RH97%, similar to changes observed for elastic modulus. Elongation values showed an opposing trend and increased with moisture content. Lignin NPs still had lower values than CNP, but xylan NPs showed comparable values. All strain measurements showed relatively large data scatter, as indicated by error bars.

The hydrophilic nature of cellulose results in strong interactions with water molecules. This interaction yields strong plasticizing and swelling effects on cellulose-based structures [177-179]. As a result, intermolecular bonds between cellulose and cellulose or fillers are reduced and replaced with hydrogen bonds formed with water molecules. Plasticizing leads to reduced stiffness (elastic modulus) and decreased intermolecular bonds between components, lowering the tensile strength. But in the case of elongation, slippage between fibers is improved, yielding higher strain values [126]. High moisture content promotes swelling, and as a result, the volume of NPs is affected by the internal expansion that results in a significant decrease in all tensile (mechanical) properties. This was observed for samples L5 and L10 at RH97%. Cazón et al. also reported that bacterial cellulose films showed a strong dependence on moisture content

[180]. According to the authors, Guo et al. studied 4 types of nanocellulose and their equilibrium moisture content, which can significantly vary and depend on cellulose structure and crystallinity [179].

Decreased properties can be expected with higher moisture content for hydrophilic materials, but the ability to recover initial properties must be studied. After the removal of excess water, it is essential to understand changes in durability. Figure 3.19 shows the selected composition's ability to recover mechanical properties after water desorption. In this case, samples exposed to RH75% and RH97% were conditioned back to RH24%. Absorbed moisture results in irreversible structural changes in all compositions. Retention of the elastic modulus is in the range of 60%, 75%, and 60% for CNP, lignin NPs, and xylan NPs, respectively. The tensile strength of the compositions was retained to a greater extent, around 80%, 95%, and 70%. Variations of the strain at failure for all samples were in the data scatter range. It is interesting to note that despite the significant difference in moisture saturation levels at RH75% and RH97% (Table 3.4), irreversible impacts after moisture desorption are similar for both groups of samples (the relative retention is almost the same for RH75-->24% and RH97-->24%). The loss of tensile properties can be explained by defects induced by sample swelling that leave various voids and structural defects after the desorption of excess water. Water migration has been shown to have a negative impact on cellulose reinforcement in composite structures when exposed to artificial weathering [181]. As discussed by Dufresne in his review of cellulose-based material applications, extensive exposure to water should be avoided to prevent the degradation of nanostructure [182]. High moisture content increased tensile properties in hot-pressed cellulose films, according to Liu et al. [127], because the structure was relieved of internal stresses. The tensile characteristics of bacterial cellulose films drop by up to 50% and 75% for tensile strength and elastic modulus, respectively, when RH50% is elevated to RH75% [183].

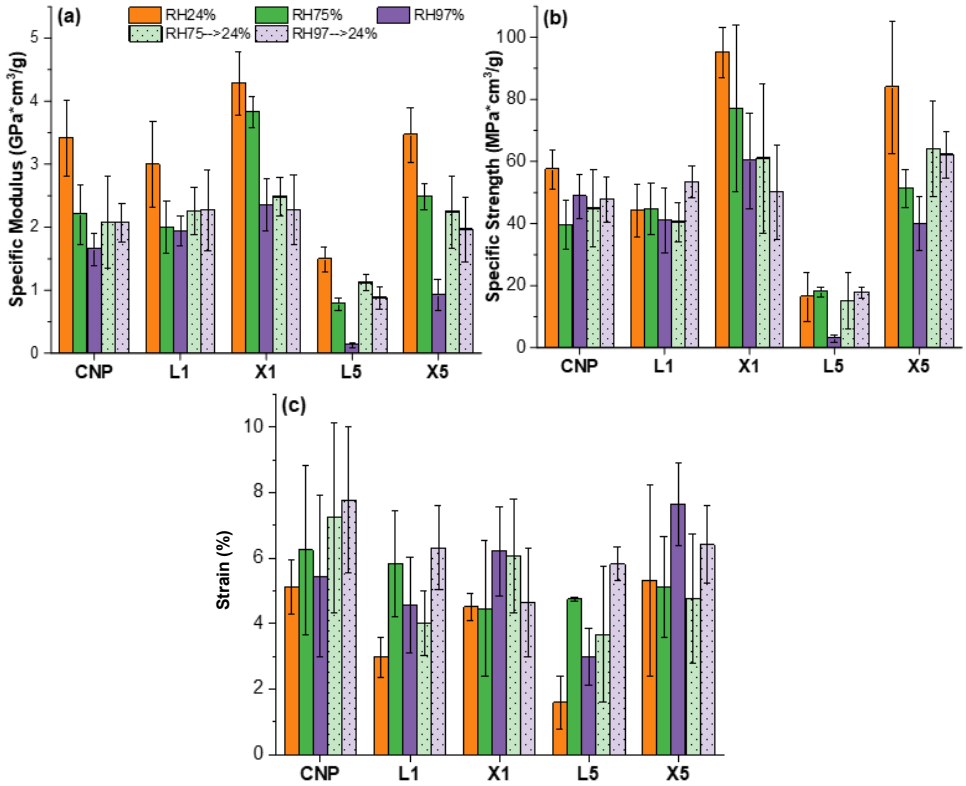

Figure 3.19. Tensile properties: (a) specific elastic modulus, (b) specific ultimate tensile strength and (c) elongation at break of CNP, L1, L5, X1, X5 NPs at different RH (24, 75, 97%) and their properties retention after moisture desorption.

3.2.5. Nanopaper performance quality analysis

The literature has a large discrepancy in the tensile properties of NPs. NPs mechanical performance is characterized by Figure 3.20, which summarizes the tensile properties of NP from various studies. Hasen et al. (3) demonstrated a very high elastic modulus, reaching 7.6 GPa for carboxymethylated NFC/Xylan NP prepared 50/50 (w/w) [124]. Pistachio shells (6) were mildly treated to process them into dimensions closer to microfibrillated cellulose than NFC [121]. The authors obtained a relatively high elastic modulus, but the dimensions of cellulose contributed to lower stress and elongation values. Xiong et al. used a combination of cellulose nanowhiskers (CNW) and NFC to produce NP (7) [184]. Rigid rods like CNW provided high elastic modulus and yielded relatively brittle NP, which could be compensated for with the addition of NFC but at a loss of elastic modulus. In general, xylan NPs demonstrate poor mechanical performance, but at the same time, acetylated arabinoxylan films (8) can achieve high properties comparable to cellulose NPs [185]. Tedeschi et al. combined hydrolyzed lignin with xylan and microcellulose compositions using a solvent system to cast bioplastics [75]. As seen by the properties of films (2), using solvents does not guarantee higher properties than conventional casting from suspensions. Due to the lack of density values and chemical

composition data in some studies, it is hard to compare various NPs directly. For accurate comparison, specific elastic modulus and strength values would be preferable, as well as a similar level of room humidity.

The NPs produced in this study show a wide range of mechanical properties. As seen from the literature data, NP properties can be improved with chemical modification by changing the chemical composition of NFC (the amount of lignin and hemicellulose) and by combining NFC with different types of fillers. In contrast, the proposed NCs' interface engineering using lignin and xylan additives could provide a sustainable and straightforward route to control the mechanical properties. The higher quality of NFC provides more significant tensile strength (stress) and elongation values but has decreased elastic modulus. At the same time, the elastic modulus is improved by the addition of smaller, more rigid particles or reduced chemical treatment of the cellulose source, but these NPs can be brittle. As our source cellulose is already highly purified and, thus, has a damaged structure from chemical pretreatment, lower elastic modulus values can be expected.

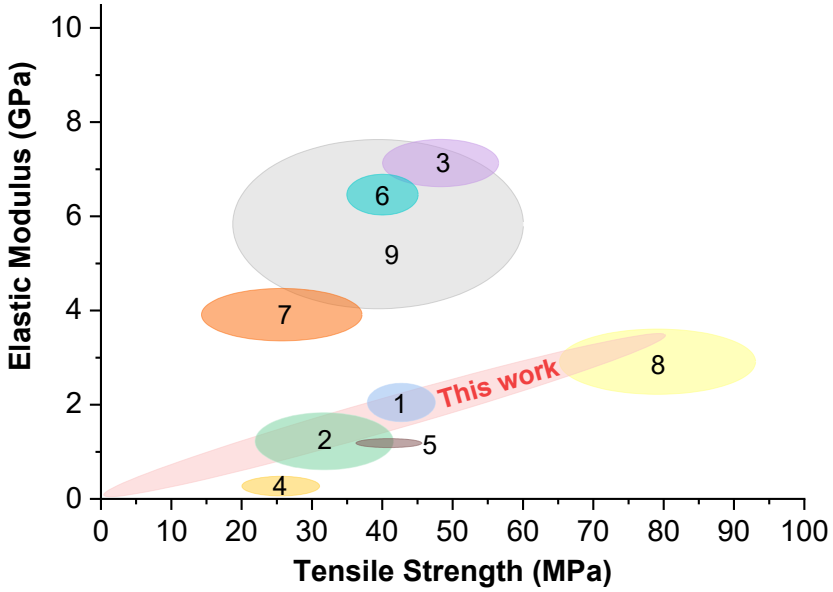

Figure 3.20. Elastic modulus and Tensile strength map to compare CNPs prepared by similar studies from the literature. (1) MFC/lignin/xylan film [127]. (2) Microcellulose/hydrolysed lignin/xylan film [75]. (3) Carboxymethylated NFC/Xylan NP [124]. (4) Xylan/carboxymethyl cellulose (CMC), oxidized carboxymethyl cellulose (OCMC) and cellulose nanofibers (CNFs) film [72]. (5) Bacterial cellulose nanofibrils and nanocrystals film [183]. (6) Bleached and unbleached pistachio shell MFC film [121]. (7) Cellulose nanowhiskers (CNW) and NFC nanopapers [184]. (8) Acetylated rye arabinoxylan (AcAX)/NFC films [185]. (9) Sugarcane bagasse NFC films [186].

As shown in Figure 3.21, a radial plot displays NP performance multivariate observations with the most desirable variables of durability characteristics – stiffness (modulus), strength, and ductility (elongation) at 24 hours of UV-light and RH75% aging. The relative changes in tensile properties for modified NPs before and after aging are shown, where UV-irradiated dry samples and samples saturated at RH24% were chosen as the reference. The unaged NP represents value 1 on the plot. The performance quality of the NP was enhanced after cellulose interface modification with the bio-based additives of xylan and lignin.

The impact of UV light irradiation is more critical to the CNP, resulting in a substantial decrease in mechanical properties. The chosen bio-based modifiers significantly enhanced the mechanical performance. Both modification methods provide enhanced moisture resistance with low loadings of 2.5 wt%. Unfortunately, low loadings did not demonstrate significant UV resistance. Xylan's impact on the strength, stiffness, and ductility (UV 24 h) properties was superior to lignin's. The xylan modification of the cellulose interface with 10 wt% showed the overall best performance. In contrast, the lignin modifier shows almost a 3-fold improvement in the NP's ductility (RH75%) and provides good moisture resistance at low loadings. Considering the food packaging application, the optimal NP samples are X10 and L2.5, which present the highest performance characteristics considering the durability in the UV-light and humidity aging tests.

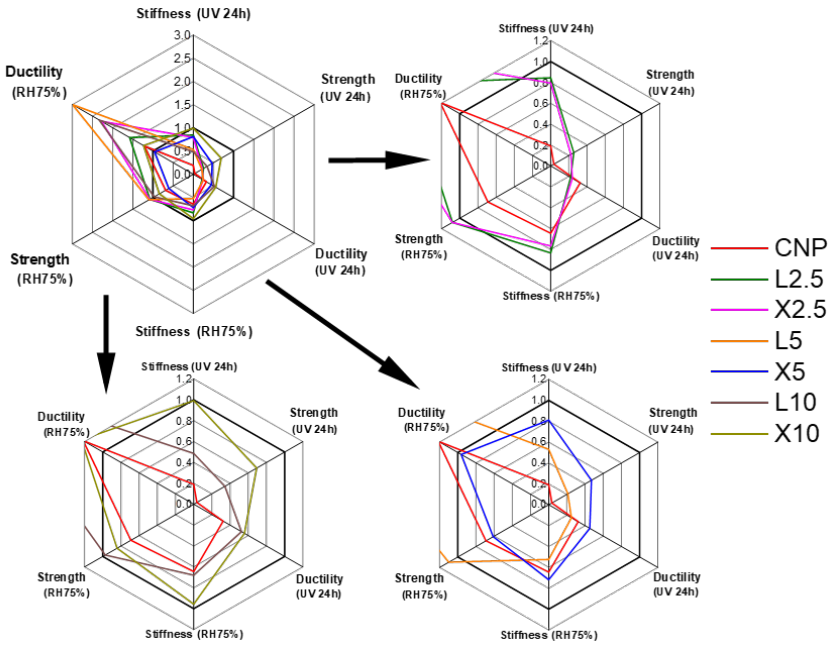

Figure 3.21. Relative changes of performance properties for NPs before and after aging. For reference dry samples were used for UV and samples saturated at RH24% for water adsorption impacts. Value 1 represents the sample before aging.

3.2.6. Summary

The proposed cellulose nanopaper modification, using lignin and xylan additives, provides a simple and sustainable route to engineer the interface in the developed mesh material and control the material's durability to the UV irradiation, moisture, and temperature. The tensile properties are significantly enhanced with the addition of xylan and lignin interface modifiers. The UV irradiation showed a milder impact on the cellulose modifications with 5 and 10 wt% xylan concentrations. The moisture absorption test showed the overall best performance for xylan's 2.5 wt% compositions. Xylan interface development in all sample concentrations showed remarkable improvements in NP UV and heat resistance. Lignin also enormously improved the UV resistance of NP. Cellulose NP without interface modifiers exhibited a catastrophic decrease in tensile properties after UV exposure. The UV irradiation damage is revealed in SEM analysis.

The oxidation and depolymerization of lignin and xylan at the protective interface for the cellulose was indicated by UV-VIS spectroscopy as a shift in absorption peak intensities and regions. Similar observations were made from FTIR spectra analysis. The moisture sorption capacity of the NP increases with moisture level and with lignin and xylan loadings. High moisture content promoted NP swelling, which failed samples with 20 and 30 wt% loadings of lignin and xylan. Absorbed moisture significantly affects the elastic modulus and strength characteristics of CNP, but resistance was improved for modified NP. The Lignin modifier resulted in higher moisture absorption capacity and, as a result, higher properties' sensitivity to humidity changes due to the strong agglomeration and phase segregation effect. But remarkably, lignin NP showed better property retention even at high moisture content compared to CNP. Retention of the elastic modulus and strength after moisture desorption is in the range of 60-95%; lignin-modified compositions show the highest property retention.

The NP films of X10 and L2.5 have presented the highest durability performance characteristics against UV-irradiation and humidity aging. The improvements were achieved by improving the interface (xylan) while the developed interphase layer covered the cellulose mesh. These completely sustainable NP film compositions are being considered for the food packaging application, which is now underway as validation for berries, fruits, and vegetables.

3.3. Sustainable hemp-based bioplastics with tunable properties via reversible thermal crosslinking of cellulose.

Modern bioplastics and biocomposites frequently contain non-biodegradable or non-sustainable components and require complex recycling routes. Sustainable materials require integrating bio-based, cheap, widely available, recycled, or waste components. To incorporate these concepts, hemp stalk waste, the industrial byproducts glycerol, xylan (hemicellulose), and citric acid were selected as key components. Hemp stalks were processed into cast papers using only mechanical processes and no chemical modifications or pre-treatments. Cast papers were impregnated with a crosslinking mixture of glycerol, xylan, citric acid, and the plasticizer polyethylene glycol (PEG). Thermal crosslinking was performed as a single-step reaction by curing materials at 140 °C. All prepared bioplastics were washed in water for 48 hours and extensively tested for water resistance and water absorption. A recycling route with depolymerization (for pulp recovery) in sodium hydroxide is demonstrated. A comprehensive analysis of crosslinking reaction is provided via FTIR and rheology, supplemented by structure analysis via SEM. As a result of component ratio variation, bioplastics achieve a high tunability of properties ranging from brittle to ductile. Dielectric analysis indicates that bioplastics have the potential for application in electric insulation. A three-layer laminate is demonstrated as a concept for potential application as an adhesive for bio-based composites.

3.3.1. Thermal stability and crosslinking characterization

As chemical crosslinking was performed at relatively high temperatures, selected compositions were tested for thermal stability in the air. Thermogravimetric weight loss and derivative weight loss curves are presented in Figure 3.22. The initial weight loss that occurs between 80 to 120 °C is attributed to the evaporation of the remaining water [49]. Around 220 °C, the initial decomposition of the main components starts. This initial step is attributed to the degradation of hemp and xylan components, especially hemp, which consists of various carbohydrates and lignin [187].

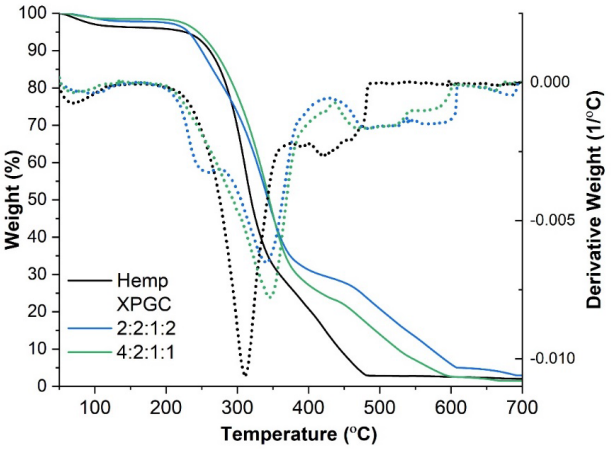

Figure 3.22. Thermogravimetric curves of hemp paper and selected bioplastics.

The impregnated components and formation of a crosslinked network contribute to the shifting of the main degradation peak by around 40 °C. The cross-linking process increases the molecular weight of carbohydrates, thus increasing the time needed for the polymer network degradation. In addition, impregnated components coat the hemp fibre network and help shield it from thermal exposure. Prolonged thermal degradation of cellulose (also xylan) can start in relatively low temperatures (around 70-80 °C), which mainly contributes to the decreased degree of polymerization [188]. Thermal crosslinking for all compositions was performed for 12 h at 140 °C, so thermal degradation was a concern for this crosslinking reaction. Nevertheless, in our case, chemical crosslinking counters degradation by forming new ester bonds. This further confirms the successful crosslinking reaction, as thermally treated samples had higher thermal stability than hemp.

For composition 2:2:1:2, the initial degradation step occurs before hemp and 4:2:1:1. The presence of low molecular weight components can explain the difference between the initial degradation step for compositions. The difference is only 20 °C, indicating that the impregnated composition 4:2:1:1 is slightly more stable due to different ratios. At the same time, both bioplastics show main degradation peak T_{max} (temperature with maximum weight loss) at around 350 °C.

The formation of the polymer network can be evaluated from dynamic rheological parameters, such as G′ (storage modulus), G″ (loss modulus), and η* (complex viscosity). The rheological properties were determined during isothermal curing with a fixed temperature of 140 °C (same as sample curing temperature) as a time sweep measurement. Graphs of log G′, log G″, and tan δ versus time were recorded for selected compositions (impregnated mixtures). Figure 3.23 shows G', G'', and tan δ curves for 2:1:2:2 and 4:4:1:2, while compositions 4:2:1:1 and 4:8:1:1 are shown in Supplementary 5. 2:1:2:2 was somewhat of an exception between prepared compositions as it shows paste-like behaviour, while others are more gel-like. This seems to be related to PEG's content and ability to retain water and form gels. PEG (or PEO) is also commonly used as the basis for hydrogels [189-191].

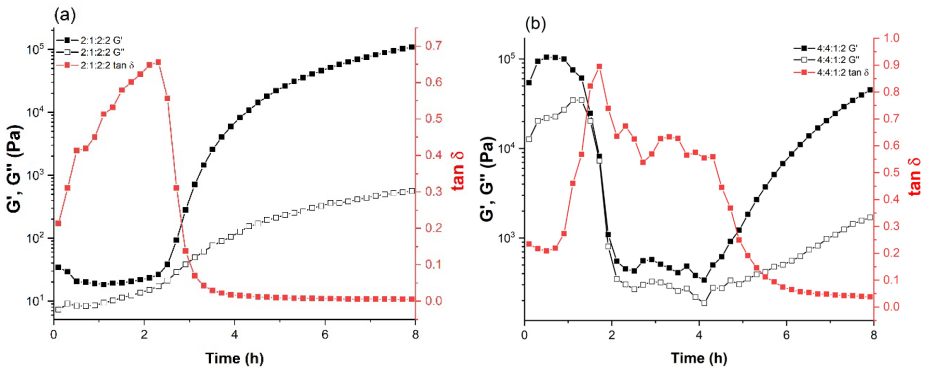

Figure 3.23. Rheological parameters G', G'', and tan δ for (a) 2:1:2:2 and (b) 4:4:1:2 impregnated mixtures.

At the start, the moduli decrease slowly, which might seem a bit strange behaviour but can be explained by water evaporation, thus delaying the start of the reaction. For 2:1:2:2, the water evaporation lasted about 20 min, while for other compositions, it occurred for 1 to 2 hours. The confined nature of the parallel plates of the rheometer significantly influences evaporation time. In Figure 3.23(b), tan δ does not show any systematic variation until 1 h, further indicating that the reaction does not occur till that point. After water evaporates, G' and G'' curves are relatively close to each other, thus indicating a region where the formation of a 3D network occurs. The third region in the graphs represents the separation of G' and G'' curves, where G' values significantly exceed G''. As the reaction approaches the complete state, the elastic properties dominate, more energy is stored, and less energy is dissipated ($G' > G''$).

According to the literature, the gelation process generally occurs at the crossover point for moduli in the case of stoichiometrically balanced compositions and with an excess of crosslinkers [192,193]. The kinetics of curing between oligomeric (polymeric) thermosetting components is not instantaneous and lasts over an extended period. Thus, it can be expected that the crossover point does not appear as distinct as with some faster reactions. In this specific system, we define it as the point where G' and G'' curves separate. Thus, for 2:1:2:2 it is around 2 h 40 min mark, and for 4:4:1:2, around 4 h 10 min. G', G'' curves reach a plateau between 4 and 5 h for 2:1:2:2, while for 4:4:1:2, it is around the end of the experiment after 8 hours. Tan δ indicates the most active phase of the crosslinking reaction, which lasts for 3 to 4 h, while G', G'' curves indicate that the reaction lasts longer, at least 6 hours. This can be expected due to the large molecules and functional groups involved in the reaction. Thus, the mobility of molecules is low, while reactions require specific orientation between functional groups. It has been reported that the reaction of glycerol, citric acid and hemicellulose can take up to 24 h above 100 °C and up to 1 h at 170 °C [194]. Thus, rheology was examined at a higher temperature, where gelation occurred under 20 min and full crosslinking under 2 hours for 2:1:2:2 at 170 °C (Supplementary 6).

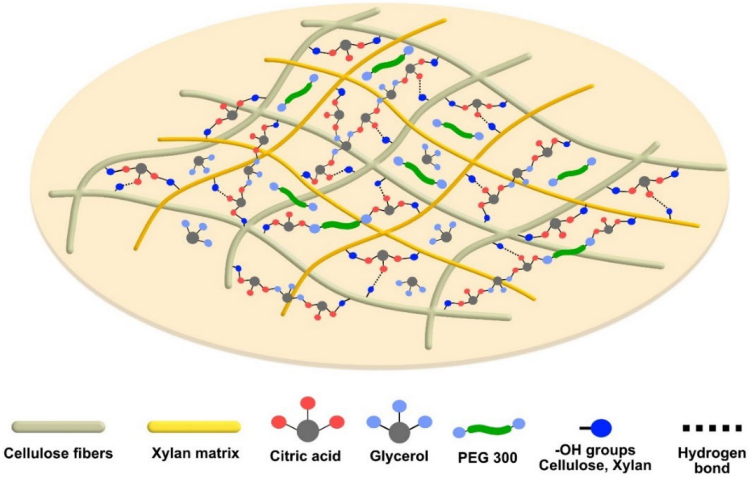

Figure 3.24. Schematic representation of proposed interactions during the formation of the crosslinked network.

The complex interactions that form crosslinked networks are presented as a scheme in Figure 3.24. The molecular characterization of the initial reactive composition and the final crosslinked network was characterized by FTIR analysis. Figure 3.25 shows the FTIR spectra of hemp, not crosslinked 2:1:2:2, and selected bioplastics (the FTIR spectra for other bioplastics is presented in Supplementary 6). Figure 3.25(a) shows spectra overlays indicating several key shifts, which indicate that the crosslinking reaction was successful. The decrease in intensity for hydroxyl group (OH) stretching vibrations with a broad peak at around 3330 cm^{-1} and a shifted peak at 1732 cm^{-1} representing the formation of ester's carbonyl group (C=O) can be considered signature peaks for the crosslinking reaction [195]. Thus, it confirms a successful crosslinking reaction for prepared bioplastics. All components, except PEG, contain a large number of hydroxyl groups. The peak intensity may not directly correlate with an overall crosslinking degree. Thus, the analysis should be focused on the carbonyl group peak. PEG seems to limit the crosslinking that occurs for composition 4:8:1:1 due to the low probability of participating in crosslinking. This is visible as low intensity for the 1732 cm^{-1} peak. This further affects the retention of other components during water treatment, resulting in high sol content (Table 3.5), and the spectra of 4:8:1:1 are relatively similar to hemp spectra.

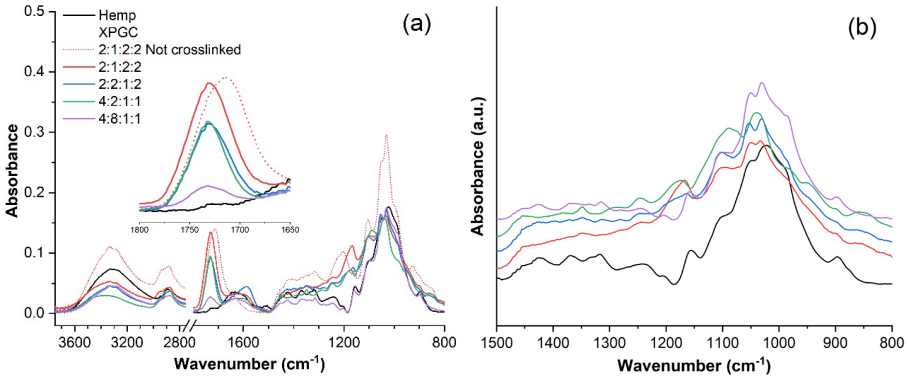

Figure 3.25. FTIR spectra of hemp paper and bioplastics: (a) spectra overlay showing a full range of scans and (b) stacked spectra showing region from 1500 to 800 cm^{-1}.

Figure 3.25(b) shows stacked spectra for the region between 1500 to 800 cm^{-1}. While this region is relatively saturated, it can be split into several parts. Most notable is the region from around 1200 to 1020 cm^{-1}, representing various stretching vibrations of the C-O bond [48]. The observable peak shift and the emergence of new peaks can be attributed to hemp fibre surface coating and chemical interactions originating from intermolecular and intramolecular bonding. The peak at around 1180 to 1170 cm^{-1} can be attributed to asymmetrical C-O-C bridge stretching [173]. The region from 1500 to 1300 cm^{-1} gets smoothed due to hemp fibre coating and signals at 1424, 1370, and 1314 cm^{-1}, which can be attributed to CH and CH_2 bending and stretching vibrations [173,196] are less pronounced or not visible. Similarly, the peak at 895 cm^{-}

[1], attributed to the β-linkage of cellulose [197], significantly losses intensity due to coated cellulose fibre surface.

3.3.2. Structure and morphology

Four distinct bioplastics and hemp paper were selected for SEM analysis based on tensile properties. Figure 3.26 shows cross-cut micrographs of selected samples with 500x and 2500x magnifications. Additional SEM micrographs showing the cross-cut and surface of selected materials are visible in Supplementary 7 and Supplementary 8. Hemp paper's structure shows a relatively dense fiber structure with visible porosity. The porosity for all samples and their respective density values are shown in Table 3.6. After impregnation, most bioplastics show half or 1/3 of their porosity compared to hemp paper. Composition 4:2:1:1 showed pronounced deposition of the impregnated mixture on the surface of hemp paper; thus, porosity is not given. The decrease of porosity was accompanied by an increase in density of up to 66 % (except for 4:2:1:1). Compositions 4:4:1:1 and 4:8:1:1 showed relatively small changes in density and porosity values. This indicates that crosslinking was limited and that most of the impregnated composition was washed out after 48 h in water.

SEM micrographs show that the nanofibrillated structure has been rearranged into larger fibres with a diameter of around 1 μm, while the length is in the tens to hundreds of micrometres. Bioplastics undergo several processes, including impregnation, thermal crosslinking, washing in water, swelling, and drying. The dimensional changes of samples showing an increase in thickness are attributed to sample swelling. Most notable in the formation of structure is washing in water, which results in the leaching of weakly bound impregnated molecules and swelling of the original structure. Composition 4:8:1:1, which showed the lowest crosslinking degree from the analysed FTIR spectra, matches well with the expectations of the described processes. The structure has large pores and visible swelling, which can be seen as the separation of hemp fibres. The other three selected compositions show relatively dense structures with coated hemp fibres that are hard to distinguish in images. Even 4:2:1:1 with a lower amount of citric acid shows a relatively dense structure, thus further indicating that PEG is the main component that limits cross-linking. The structure of 4:2:1:1 retains visible porosity, and it is also the only bioplastic with a separate layer of impregnated composition deposited on the surface. The structures of 2:1:2:2 and 2:2:1:2 are relatively similar, showing uniform impregnation and dense structure, which was retained after 48 h in water. The observed structures align with the FTIR results, showing denser packing with a higher crosslinking degree.

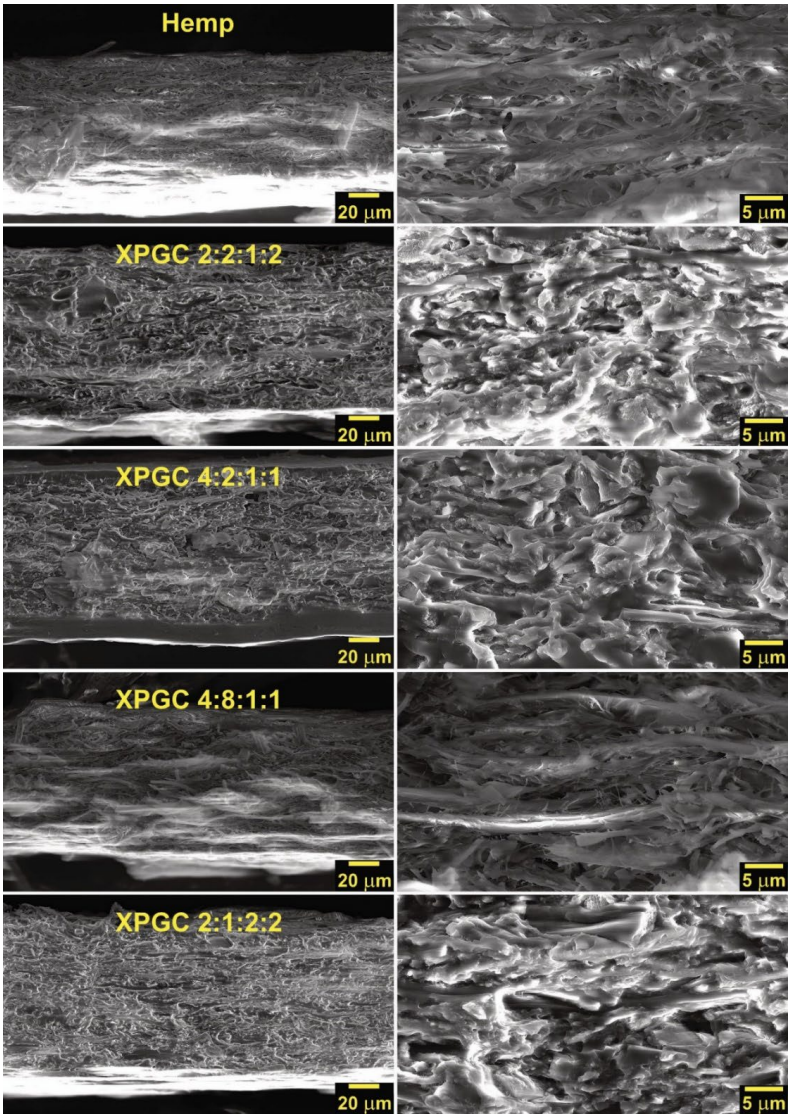

Figure 3.26. SEM micrographs of hemp paper and selected bioplastics shown in 500x and 2500x magnifications

3.3.3. Tensile properties and water uptake

Water absorption and swelling in water are often considered the biggest issue for various cellulose-based materials. As water molecules migrate into the structure, they disrupt existing intermolecular bonds, thus plasticizing the structure. As a result, the high stiffness of cellulose fibres is lost, and the material becomes soft and moldable. Furthermore, if hemp paper is left in water, it swells, the fibres separate, and any mechanical interaction easily breaks the paper into pieces. Thus, to confirm the durability and concept of our proposed bioplastics, all seven

compositions were submerged in water (also referred to as washed-in water) for 48 h and dried afterwards.

Table 3.6 shows measured elastic modulus, tensile strength, and elongation values. Figure 3.27(a) shows tensile stress-strain curves for selected three compositions before and after being submerged in water. Neat denote compositions as they were before washing in water. After being submerged in water and dried, all three tested compositions showed a significant increase in elastic modulus and tensile strength, while strain values were relatively unchanged. The enhanced mechanical properties could be attributed to the removal of small mobile molecules and PEG, which work as plasticizers. This would explain the increase in elastic modulus and tensile strength. At the same time, the remaining PEG can enhance the elongation values, and it can be observed that an excessive amount of PEG yields mainly adverse effects on elastic modulus and tensile strength. The elongation also depends on the crosslink density, which was not examined in this research.

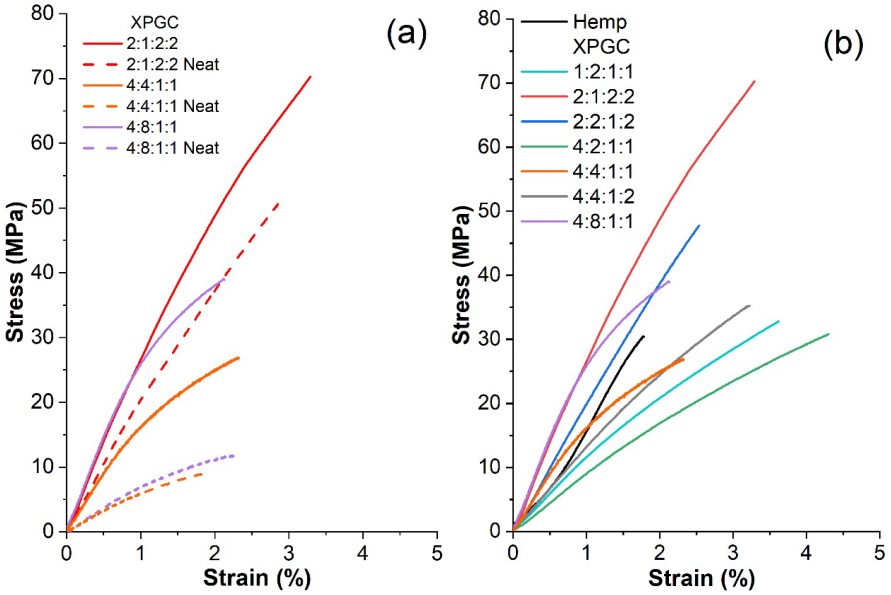

Figure 3.27. Tensile stress-strain curves for (a) selected bioplastics before and after washing in water (b) hemp paper and bioplastics.

Figure 3.27(b) compares stress-strain curves for all seven impregnated compositions and hemp paper, and Table 3.6 shows their respective elastic modulus values. The data indicate that bioplastic properties can be significantly tuned compared to hemp paper, achieving up to 2.3-fold improvement in tensile strength value, up to 1.8-fold for elastic modulus, and up to 2.4-fold for elongation. In addition, six compositions showed enhanced tensile strength values, and all seven had enhanced elongation values. In our previous research, we demonstrated that small amounts of xylan could enhance the properties of cellulose networks by densifying them and adding extra intermolecular bonding [48,49].

Compositions 4:4:1:1 and 4:8:1:1 show the overall most similar properties to hemp paper, indicating that the ratio of components restricted the crosslinking reaction but was enough to achieve bioplastics that retain dimensional stability after being submerged in water. As a result, it matches well with SEM observations where 4:8:1:1 was closest to hemp paper and most of the impregnated components were washed out (leached). Thus, crosslinking yielded only a significantly stiffer structure with the highest observed elastic modulus of 2927 MPa. Two of the highest tensile strength values were obtained for compositions 2:1:2:2 and 2:2:1:2. Compared to other compositions, these have smaller xylan and/or PEG ratios to citric acid, thus resulting in a stiffer crosslinked network. The high tensile strength values indicate good compatibility between components and strong chemical bonding. The remaining compositions somewhat complement this observation. 4:2:1:1, 4:4:1:1, and 4:4:1:2 again confirm that too much PEG in impregnated composition results in an opposite effect, interrupting the formation of the dense crosslinked network. 1:2:1:1 shows that PEG can yield a significant positive impact on elongation, but then xylan content should be reduced. Molecule sizes could explain this, as both xylan and PEG are larger molecules competing for special positions between hemp fibrils and fibres.

Table 3.6.

Apparent density, porosity, sol content, water uptake, and tensile test parameters for hemp paper and bioplastics

Sample	Apparent density (g/cm^3)	Porosity (%)	Sol content (wt%)	Water uptake (%)	Elastic modulus (MPa)	Ultimate tensile strength (Mpa)	Strain at break (%)
Hemp	0.73 ± 0.04	51.3	-	143.0 ± 3.2	1660 ± 190	30 ± 3	1.8 ± 0.2
XPGC							
1:2:1:1	1.08 ± 0.02	25.4	15.4 ± 3.2	63.2 ± 2.1	1176 ± 128	33 ± 4	3.6 ± 0.3
2:1:2:2	1.07 ± 0.07	27.5	6.7 ± 2.1	20.4 ± 1.3	2828 ± 348	70 ± 7	3.3 ± 0.6
2:2:1:2	1.21 ± 0.05	17.3	10.2 ± 1.6	73.1 ± 9.4	2040 ± 339	48 ± 6	2.5 ± 0.4
4:2:1:1	1.34 ± 0.17	-*	18.8 ± 2.5	63.1 ± 1.6	913 ± 156	31 ± 3	4.3 ± 0.1
4:4:1:1	0.82 ± 0.04	44.7	24.3 ± 2.8	78.8 ± 1.8	1840 ± 236	27 ± 2	2.3 ± 0.4
4:4:1:2	1.19 ± 0.02	18.0	22.4 ± 2.2	56.9 ± 3.4	1350 ± 120	35 ± 2	3.2 ± 0.3
4:8:1:1	0.78 ± 0.03	47.5	54.7 ± 4.1	100.2 ± 7.6	2927 ± 271	39 ± 2	2.1 ± 0.2

* Precise calculation was not possible due to the unique morphology of the sample.

Water uptake was further tested for material durability. Thin bioplastic samples achieved equilibrium water uptake after 24 h and retained similar values for 30 days. Water uptake percentage and sol content are shown in Table 3.6. All bioplastics have significantly reduced water uptake compared to hemp paper. This is because hemp paper slowly swells in water, while bioplastics retain their shape due to chemical crosslinking. Most notable is composition

2:1:2:2, which achieved a 7-fold decrease in water uptake. Sol content represents a mass of composition that was washed out from the composition after thermal curing. These values correlate well with water uptake and SEM microstructure, where 2:1:2:2 and 4:8:1:1 represent both ends of property dispersion. Some impregnated compositions stick better to the surface and form denser structures; this could explain variations in sol values.

3.3.4. Dielectric properties

Bioplastics were tested for their dielectric properties to examine their potential application in the field of electric insulators. Plots showing ε' (dielectric permittivity), tan δ (dielectric loss tangent), and σ (electrical conductivity) dependence on frequency (10^{-3} to 10^{8} Hz) in double logarithmic scale are presented in Figure 3.28. The dipole orientation polarization and interfacial polarization are the two main processes that occur in this frequency range and are characterized by dielectric permittivity plots. The duration required for orientation is shortened by increased frequency. As a result, bioplastics permittivity is reduced. In addition, interfacial polarization due to the polar dipoles arising from the abundant hydroxyl groups can enhance dielectric permittivity [198]. On the other hand, with dense crosslinking, the amount of hydroxyl groups is reduced, thus reducing dielectric permittivity.

Hemp paper electric conductivity values match those reported in the literature for cellulose [199]. Similarly, electric conductivity is influenced by mobility and the number of charge carriers that mainly originate from the polar groups [198,200]. Which, in the case of dense crosslinking, should reduce the conductivity. The observations for compositions show that 2:1:2:2 had enhanced dielectric properties, while 4:2:1:1 and 4:8:1:1 had enhanced conductivity and permittivity compared to hemp paper. Hemp paper is a porous material that limits charge carrier movements, while impregnation crates denser bioplastic structures. As a result, in the case of 2:1:2:2, the dense crosslinking reduces the number of polar groups and their mobility, while for compositions 4:2:1:1 and 4:8:1:1, the added charge carriers counter the effects of crosslinking and slightly enhance conductivity. All tested materials are suitable as dielectric insulators, especially 2:1:2:2, which show the best water resistance and lowest water uptake values, as discussed above.

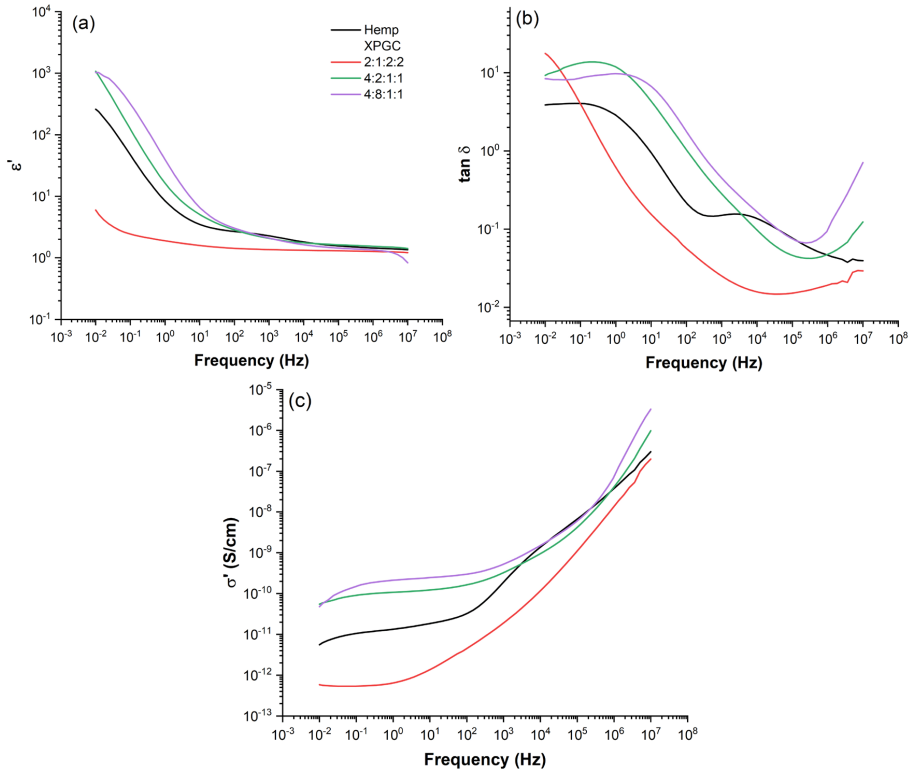

Figure 3.28. Dielectric properties of hemp paper and selected bioplastics: (a) dielectric permittivity (ε'), (b) dielectric loss tangent (tan δ), and (c) electrical conductivity (σ') dependence on frequency.

3.3.5. Depolymerization and recycling

The depolymerisation route was examined as an alternative to the biodegradation route to promote sustainable material management and incorporate a circular approach to generated waste. Bioplastics were inserted in alkaline and acidic solutions and neutral water. While testing water uptake and leaching, we observed that bioplastics stay stable at 20 °C for at least one month in water environments. Alkaline ester hydrolysis was tested with NaOH (0.5 mol/L) solution at 20 °C, and it was observed that surface-impregnated compositions degrade rapidly between 10 min to 1 hour, yielding hemp-cellulose pulp. The sample loses colour and shifts to an off-white colour, and fibres separate over time, resulting in a pulp-like mass formation. The pulp can then be filtered, recovered, and used for new material preparation. Acidic ester hydrolysis was tested with HCl (0.5 mol/L) solution, but even heating at 80 °C for 6 h did not depolymerize the bioplastic's structure. Treatment with an HCl solution slightly changed the surface colour of the sample. The images of depolymerized samples and the proposed recycling route are shown in Figure 3.29.

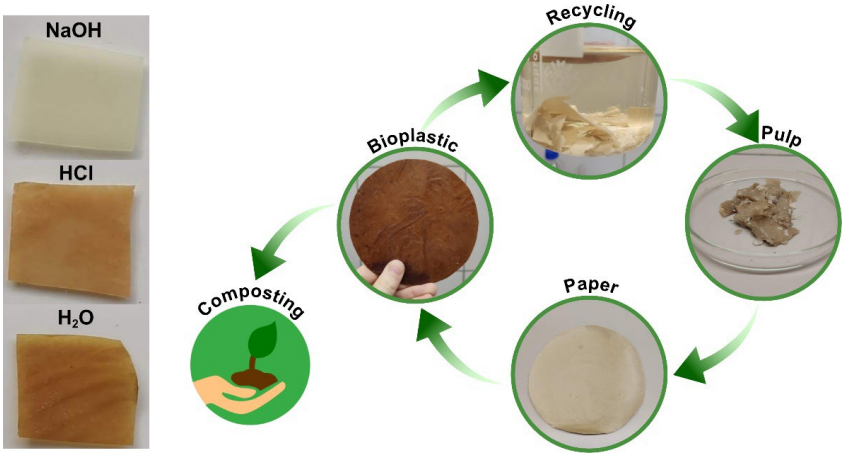

Figure 3.29. Proposed recycling route and pictures showing alkaline and acidic solution impact on bioplastics.

3.3.6. Implications

The global necessity of innovative sustainable materials and technologies is rising exponentially, particularly in tandem with the expanding demand for the replacement of petroleum-based commodities due to the anticipated lack of oil feedstock and growing environmental responsibility. As a result, forestry and agricultural waste are increasingly viewed as resources, particularly as a viable route to solving these issues. So, bio-based waste is continually developed to generate high-value products and materials through novel and sophisticated technologies.

Petroleum-based polymers are the main component of contemporary polymer-based materials and composites, and they are also commonly used as adhesives in wood and paper products. With the current state of affairs, the forestry and agricultural-based sectors face a considerable lack of innovative development in terms of 100% green bioplastics and bioplastics. Manufacturers of bioplastics and wood-like composite products (see Figure 3.30) should examine circular alternatives to replace fossil-based plastics and adhesives. Hemp stalks used in this research are underutilized agricultural waste products with high cellulose content (69 wt%) and total carbohydrate content of 80 %. This contributes to high reactivity towards crosslinking reactions and excellent inherited mechanical properties.

Xylan (hemicellulose) is often considered and treated as a waste product in the wood processing industry as it has a relatively limited field of applications. Glycerol is a known byproduct of biodiesel production, which is still underutilized due to the large amounts produced. Citric acid is one of the essential organic chemicals produced in large volumes. It is also one of the few fully produced from bio-based sources using fermentation. This paper shows how to use the specified sustainable raw materials.

To summarize, the suggested bioplastics contain mostly bio-based components, and the utilized components are fully biodegradable. By varying the xylan, PEG, glycerol, and citric acid content in the bioplastic, we could modify the material's structure and exploitation properties. The proposed bioplastics are not restricted to impregnation; they may also be used

to make laminates by employing impregnated mixtures as paper and woody material adhesives. The tunable properties and morphology indicate various applications, such as construction materials, furniture, insulators, membranes, adhesives, and more.

Figure 3.30. (a) Three-layer laminate prepared with 4:2:1:1 as an adhesive for hemp paper sheets. (b) Optical microscopy image showing 3 layers of laminate composite.

3.3.7. Summary

This study investigates the performance of hemp bioplastics, consisting of hemp paper impregnated with seven varied ratio compositions of xylan, PEG, glycerol, and citric acid. In addition, three-layer laminate was prepared to demonstrate adhesive properties. Based on the experimental results, the following conclusions are presented:

I. FTIR indicates the formation of ester bonds and successful crosslinking reaction; at the same time, reduction in hydroxyl group signal intensity complements this observation. Rheology studies at 140 °C show that the initial crosslinking reaction starts after water evaporation and that around 2 to 3 h are needed after water evaporation to reach gelation, while for complete crosslinking, more than 6 h are needed. Increasing the reaction temperature to 170 °C significantly lowers the reaction time to around 1 h. Kinetics were studied with the impregnated mixture, and, according to the author's experience, crosslinking occurs faster with the presence of hemp paper. The optimization and in-depth kinetics research are part of an ongoing study.

II. The bioplastics show exceptional resistance to water, preserving their dimensional stability. While submerged in water, bioplastics lost 7 to 55 wt% (sol content). Surprisingly, after washing samples in water for 48 h, tensile strength and elastic modulus significantly increased while retaining about the same enhanced elongation values. The highest achieved tensile values show an elastic modulus of 2.9 GPa, a tensile strength of 70 MPa, and an elongation of 4.3 %. Tensile failure indicates a high degree of tunable properties as materials range from brittle to ductile.

III. Impregnation results in a very dense structure resistant to water uptake, showing up to a 7-fold reduction. The excess amount of PEG results in the porous structure of hemp

paper being preserved while gaining crosslinked stability. This opens a research direction that could be exploited to prepare membranes and filters.

IV. It is possible to use the impregnated mixture as an adhesive to prepare laminates and other composite-type materials. The prepared 3-layer hemp paper laminate showed excellent bonding in optical microscopy. The reversal of crosslinking was tested and achieved in an alkaline water solution, presenting a recovery route for paper pulp. All used materials are biodegradable; thus, the adaption of presented bioplastics would preserve a clean environment.

3.4. From wood and hemp biomass wastes to sustainable nanocellulose foams

Transition to the circular economy requires the implementation of recycling and reuse routes for waste products. This research addresses one of the leading emerging areas, i.e., the development of sustainable materials and natural waste processing, namely wood and hemp byproducts. The cellulosic nanomaterials derived from these under-utilized waste residues and byproducts also serve as promising natural precursors for advanced applications, e.g., biomedical, pollution filtering, and thermal insulation. The wood and hemp fibrils were prepared by microfluidic processing of 0.2 – 1.0 wt% cellulose water suspensions. After freeze-drying, the resulting foam materials were characterized with a bulk density of 2 – 36 mg/cc. Key characteristics of the obtained hemp and wood nanocellulose (NC) foams were examined by the mechanical response, porosity, thermal conductivity, thermal degradation, chemical composition, and morphology. Hemp NC foams showed higher performance characteristics that coincide with almost twice the length of the fibrils, 1.5 times higher cellulose content, and a more homogeneous mesh-like structure compared to wood NC foams. In addition, the thermal performance of obtained NC foams was in the range of 34 – 44 mW/m·K, which makes their application comparable to commonly used insulation materials.

3.4.1. Structural characterization

Figure 3.31(a-b) shows the optical microscopy micrographs of the prepared microcellulose powders, while Figure 3.31(c-d) shows STEM micrographs of nanocellulose fibrils obtained from wood and hemp microcellulose powders. The measured length of hemp fibers is 372 μm which is twice as long as raw wood fibers, which is 181 μm (Table 3.7). Wood particles are shorter in length (L) and narrower in fiber diameter (D). Thereto, their calculated L/D ratio is smaller. The NFC parameters are summarized in Table 3.8, evidence that the nanofibrils' average diameter is 123 and 70 nm for wood NFC and hemp NFC, correspondingly. The coagulation stability of the prepared dispersions of the hemp and wood NC fibrils in water was evaluated employing the zeta potential (ζ) [201,202]. The obtained ζ are also represented in Table 3.8. Reported data are average values of all measured NFC suspension concentrations. The zeta potentials received for wood and hemp NFC samples are -23.6 mV and -22.6 mV, respectively. The cellulose fibrils have an anionic charge due to the acidic groups (-COOH) originating from the remains of cell wall constituents (lignin and xylan) [203]. The attractive Van der Waals force between the particles dominates over the repulsive force for ζ absolute values below 25 mV. Therefore, individual NFC particles tend to attract each other and form aggregates [204,205]. Besides, zeta potential higher than 25 mV generates greater electrostatic repulsion that resists nanoparticle agglomeration and further promotes the formation of a stable aqueous suspension [206].

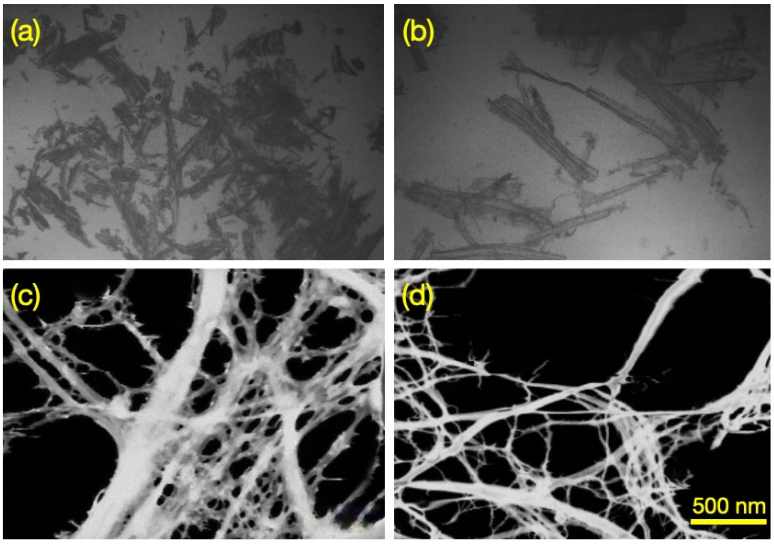

Figure 3.31. Optical microscopy micrographs (a, b) of microcellulose powders and TEM (c, d) micrographs of NC obtained from wood (c) and hemp (d) waste.

Table 3.7.

Geometrical dimensions and aspect ratio of wood and hemp waste powders

Sample	Length (µm)	Diameter (µm)	Aspect ratio (L/D)
Wood	181 ± 86	30 ± 16	7 ± 5
Hemp	372 ± 183	48 ± 23	9 ± 5

Table 3.8.

STEM measured fibril diameter and zeta potential of obtained wood and hemp NFCs' water suspensions

Sample	Diameter (nm)	Zeta potential (mV)
Wood NFC	123 ± 50	-23.6 ± 8.6
Hemp NFC	70 ± 32	-22.6 ± 8.2

3.4.2. Fourier transform infrared spectroscopy (FTIR)

The chemical structure of the various cellulose waste was evaluated by FTIR spectroscopy. Figure 3.32 compares the FTIR spectra of wood and hemp before and after alkaline treatment with NaOH. The absorption bands at approximately 3330 and 2900 cm^{-1} are attributed to O-H and C-H groups stretching vibrations, respectively [207]. The band at 1730 cm^{-1} is attributed to the C=O valance vibration of the hemicellulose acetyl group or the ester linkage of the ferulic carboxylic groups' p-coumaric acids of lignin and hemicellulose [208]. This band absorption is higher in raw wood samples than in raw hemp samples. According to FTIR spectra, hemp

samples have a lower amount of hemicellulose/lignin than wood samples, which is also testified by the chemical analysis of components (Table 2.1). The present absorption band is absent in both spectra ranges of wood and hemp samples obtained after chemical treatment with NaOH, indicating the removal of hemicelluloses and lignin from the surface [208]. In contrast, the chemical analysis revealed their full content in the samples. The band at 1640 cm^{-1} was attributed to C=O stretching in the carboxyl group and can also be associated with the H–O–H stretching vibrations of absorbed water in carbohydrates [207,209]. Bands approximately at 1422 cm^{-1} represent -CH, -CH_2 group bending; other absorption bands, i.e., 1030 cm^{-1} and 890 cm^{-1}, are associated with the C–O stretching and C–H deformation vibrations of cellulose [205,208].

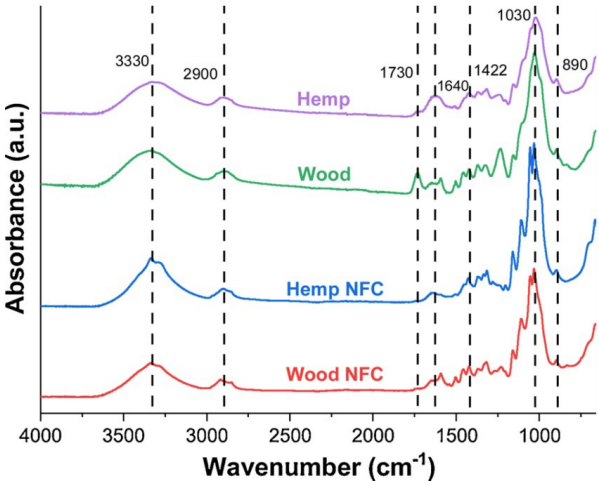

Figure 3.32. FTIR spectra of wood and hemp and wood NFC and hemp NFC.

3.4.3. X-ray diffraction (XRD) analyses

Figure 3.33 shows the XRD pattern and the calculated corresponding crystallinity indices (CI) of raw samples (without alkaline treatment) and for wood and hemp fibrils. All NFC samples show typical cellulose I structure with the characteristic diffraction peaks of 2θ angles at around 16 ° and 22 ° corresponding to the (101) and (002) planes. According to literature, it is expected to see three peaks at about 15 °, 16 ° and 22 ° corresponding to (101), ($10\bar{1}$), and (002) planes, respectively [119], but as it can be observed, the presence of non-cellulosic substances such as hemicellulose and lignin causes the merging of two distinct diffraction peaks at 15 and 16 ° into a single diffraction peak at 16 ° [205]. Besides, the hemp NFC sample with very low hemicellulose and lignin content has two distinct diffraction peaks at 15 ° and 16 °. Pacaphol et al. also reported very similar results of two diffraction peaks in their study for hemp fibrils [210]. The small shoulder observed at 21 ° corresponds to cellulose II polymorph [211]. The corresponding CI of cellulose shows a significant increase in crystallinity from 34.0 % for raw wood up to 55.2 % for wood NFC. Hemp NFC crystallinity increases from 61.6 % up to 74.0 %, correspondingly. Initially, hemp is more crystalline than wood material, and CI increases even more after processing. The removal of hemicellulose and lignin in amorphous regions leads to increased hemp and wood cellulose crystallinity.

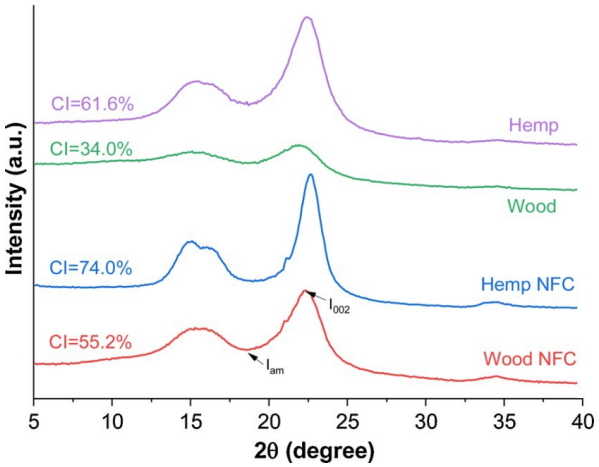

Figure 3.33. XRD curves of raw wood and hemp and wood NFC and hemp NFC: purple – raw hemp; green – raw wood; blue – hemp NFC; red – wood NFC.

3.4.4. Thermal analysis

The TGA and DTG curves obtained from the thermogravimetric analysis of the wood and hemp samples are shown in Figure 3.34 (a) and (b), respectively. All the samples show two pronounced characteristic steps of weight loss. The first one is detected in the range 40 – 130 °C with 5 – 6 % of weight loss, which corresponds mainly due to the evaporation of adsorbed water in the NC [212]. The calculated onset and main degradation temperature data are represented in Table 3.9.

The process of the degradation of the samples starts at a range of 250 – 260 °C, which shows as a small shoulder in DTG curves for wood samples, indicating degradation of hemicellulose following literature [134]. A significant weight loss is observed in the second step, with the main degradation temperature at around 333 °C, which corresponds mainly to NC degradation [212]. All NC samples show roughly the same degradation onset degradation temperature at about 255 – 260 °C, and the TGA weight loss curve difference is not significant at the degradation temperature either, except for hemp NFC. NFC hemp shows higher degradation onset temperature at around 274 °C, and the weight loss after 350 °C is significantly higher than other NC samples, which is also seen in the DTG graph (Figure 3.34(b)). Rapid weight loss above 350 °C could be explained by significantly lower lignin content in hemp samples. It was reported that lignocellulose components resulted in enhanced thermal stability [132,133]. The higher onset of degradation for hemp NFC could correspond to a higher NC crystallinity index, confirmed by XRD analysis. The comparison of degradation temperatures is presented in Table 4, which includes residues at 450 °C and 600 °C. Hemp NFC sample has better overall thermal stability when compared to the main degradation step, while wood NFC sample retain more residue after maximum degradation temperature. Thermal degradation ends around 550 °C for all samples, where a small percentage of residue charcoal is observed, and complete degradation can be considered to have taken place.

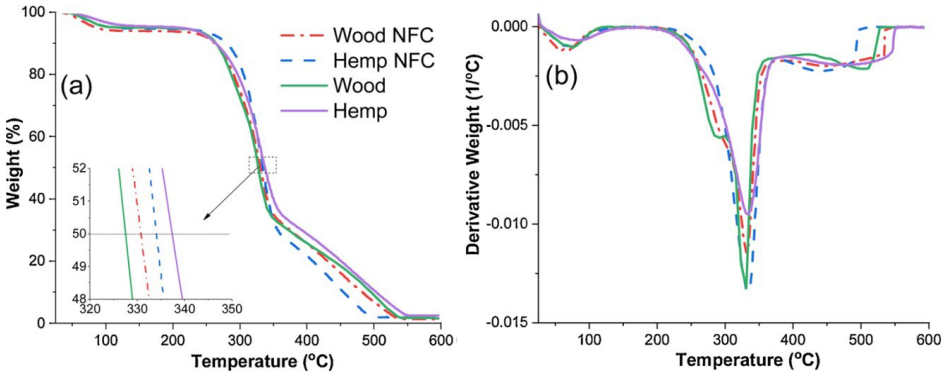

Figure 3.34. Thermogravimetric weight loss (a) and differential thermogravimetric (b) curves.

Table 3.9.

Thermal degradation characteristics of wood and hemp waste powders and wood and hemp NFC

Sample	The onset of degradation temp. (°C)	Main degradation temp. (°C)	Residue at 450 °C (%)	Residue at 600 °C (%)
Wood	254	328	18.10	1.63
Wood NFC	259	332	16.18	1.39
Hemp	253	333	20.19	2.42
Hemp NFC	274	333	10.98	1.82

3.4.5. Foam material morphology characterization

The physical characteristics of the obtained wood and hemp NC foams are provided in Table 3.10. The bulk density was in the range of 2 – 11 mg/cc for hemp NFC foams, while values were higher at 4–36 mg/cc for wood NFC samples produced from comparable concentrations. The porosity for all samples was above 99%.

SEM micrographs of wood and hemp foams with their respective bulk densities in the range of 2 – 36 mg/cc are shown in Figure 3.35. The obtained wood and hemp foams have an obvious mesh-like network porous structure made of entangled cellulosic nanofibrils. Comparing the structure of wood and hemp foams, the experimentally measured and reported bulk density of the hemp and wood foams significantly affected the observed porosity. The increase of the density yields a decrease in porosity, as shown in Figure 3.35 and Table 3.10. The hemp foam samples have a less pronounced increase in density and agglomeration of fibrils compared to wood foams. The hemp also has a higher overall geometrical size aspect ratio of individual fibrils. While hemp fibrils are longer and thinner than wood fibrils, thus web-like entanglement is more pronounced. Wood foams also contain occasional larger (denser) formations, which could correspond to the fibril bundles or agglomerates induced by lignin and hemicellulose traces [213]. It also correlates well with the other results obtained from XRD and FTIR that suggested a higher lignin and hemicellulose content remains in wood foam than in hemp foam

samples. An additional bleaching process of the wood samples could probably remove remaining lignin and hemicellulose traces and enhance the defibrillation process to a greater extent.

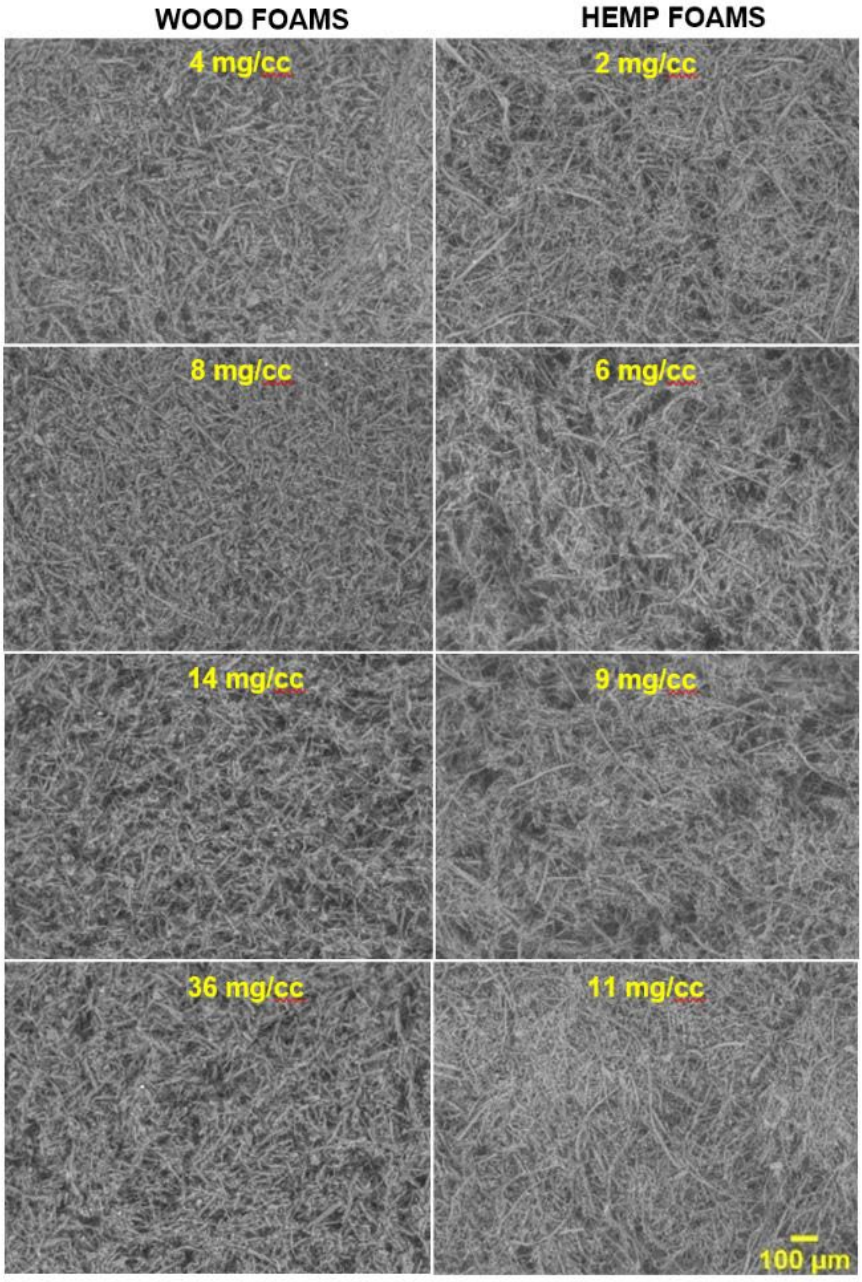

Figure 3.35. SEM micrographs of wood and hemp foams at 100x magnification.

3.4.6. Compression properties

The mechanical behavior of obtained highly porous NC foams was studied by compression loading, which can be challenging, mainly due to the high fragility and low load-bearing behavior of highly randomized solid skeleton mesh structures [214]. Experimental characteristic compression stress-strain response curves are shown in Figure 3.36, while the corresponding elastic modulus values $E_{5\%}$, $E_{25\%}$, $E_{50\%}$, $E_{75\%}$ calculated at strain 5, 25, 50, and 75 % correspondingly and strength values $\sigma_{50\%}$ calculated at strain 50 % are summarized in Table 3.10. The obtained stress-strain diagrams exhibit three distinct deformation regions – the linear elastic range, followed by an almost horizontal stress plateau and rapid stress increase range at high strain intensities due to the material's densification [215]. As seen in Table 3.10, the samples measured tensile properties, such as the compressive elastic modulus and strength, increase with density increment [216]. Moreover, Figure 3.37(a) and (b) show that the elastic modulus reveals a power-law relationship with its density, and specific strength shows a linear dependence from the NC content. The hemp NFC foam provided a 4-fold higher elastic modulus at an absolute bulk density of 8 – 9 mg/cc than the wood NFC foam sample (Figure 3.37 (a)). While Figure 3.37(b) reveals a similar tendency observed for the specific strength (σ/ρ) it testified 6-fold higher values for hemp foam compared to the wood foam prepared from 1 wt% NFC suspension. The observation could relate to the complex effect of a more extensive crystallinity index of NC fibrils, the higher length/diameter aspect ratio observed in hemp NFC.

Table 3.10.

Physical properties of the obtained NC foams: bulk density, porosity, compressive modulus and strength for various strain levels and densities.

Sample	Bulk density (mg/cc)	Porosity (%)	$E_{5\%}$ (kPa)	$E_{25\%}$ (kPa)	$E_{50\%}$ (kPa)	$E_{75\%}$ (kPa)	$\sigma_{50\%}$ (kPa)
Wood NFC							
0.2 wt%	4	99.8	0.17	0.27	0.27	6.61	0.13
0.5 wt%	8	99.5	1.16	0.71	1.32	7.89	0.66
1.0 wt%	14	99.2	2.03	2.01	4.05	22.2	2.02
3.0 wt%	36	97.8	28.2	35.6	52.8	164.6	26.5
Hemp NFC							
0.2 wt%	2	99.9	1.04	0.47	0.36	0.97	0.18
0.5 wt%	6	99.6	2.93	2.63	4.00	10.8	2.04
1.0 wt%	9	99.4	7.59	6.96	10.7	50.5	5.34
3.0 wt%	11	99.3	16.1	16.1	23.1	90.1	11.6

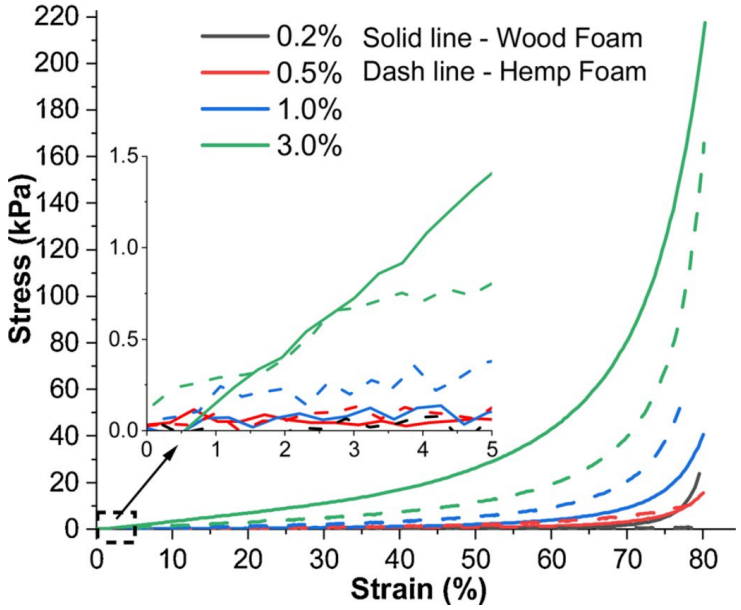

Figure 3.36. Compressive stress-strain curves of wood and hemp foam samples till up to 80% strain: solid line – wood foams and dash line – hemp foams.

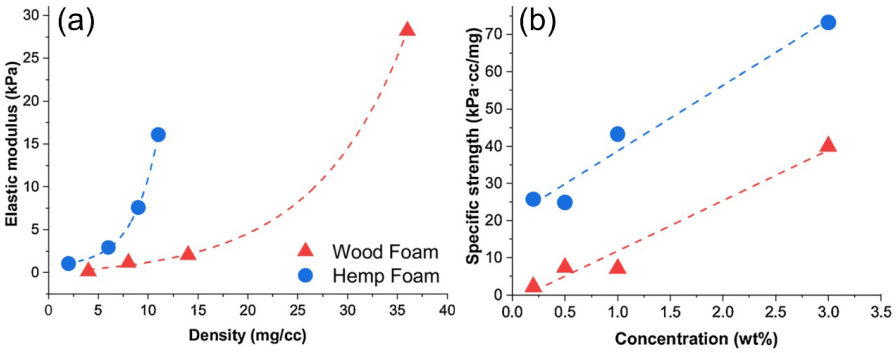

Figure 3.37. Elastic modulus dependence from foams density (a), specific strength dependence from the suspension concentration (b): red – wood samples; blue – hemp samples.

3.4.7. Thermal conductivity properties

The thermal conductivity of NC foam materials was investigated by the transient plane source method. The experimentally measured effective thermal conductivity of the produced foams as a function of porosity (pore volume fraction) is shown in Figure 3.38. Thermal conductivity decreases with the increasing porosity of samples. The data for both wood and hemp NFC foams follow the same trend. Error bars for k are comparable with symbol sizes, while data scatter for porosity is more noticeable, particularly for wood NFC foams. The measured values (0.033 – 0.044 W/m·K) are well in the range of 0.015 – 0.07 W/m K of other studies on cellulose nanomaterial-based foams [216,217]. The low thermal conductivities could be achieved independently of pore sizes [218].

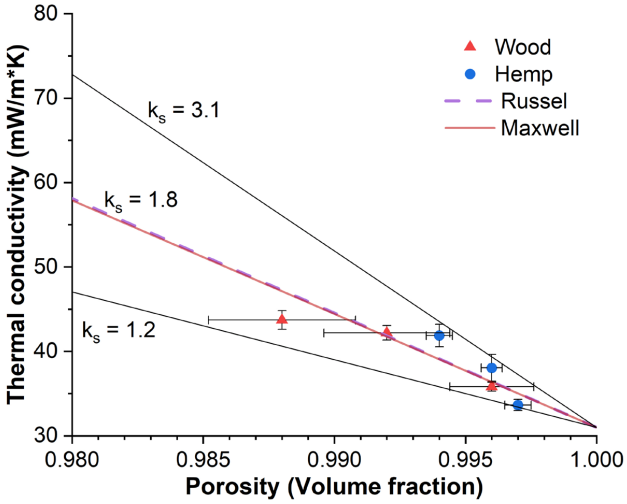

Figure 3.38. Thermal conductivity of obtained foams as a function of porosity. Symbols are experimental data; lines are calculations by Eq. (3.4) and Eq. (3.5).

The effective thermal conductivity of NC foams was calculated by four different models: two based on effective medium approximations (Maxwell-Eucken Eq.(3.4) and Russel Eq.(3.5)) and two-unit cell models given by Eq.(3.6) and Eq.(3.7). For relatively large pores of mm sizes (as determined by SEM), contributions from the Knudsen effect Eq.(3.8)–(3.99) and radiative component Eq.(3.10) were evaluated as negligible and, thus, neglected. The characteristic sizes of pores were taken as D ≈ L = 5 mm and 2t = 0.24 mm. These values are selected based on SEM structural analysis. SEM analysis has shown the highly irregular morphology of foams with pores sizes from tens of nm to μm.

Maxwell-Eucken model for spherical inclusions (pores) that is equivalent to the Hashin-Strickman upper bond [219-221] is given by the following Eq:

$$k_c = k_s \frac{k_g+2k_s+2V_p(k_g-k_s)}{k_g+2k_s-V_p(k_g-k_s)}, \quad (3.4)$$

where V_p is the volume fraction of pores k_g and k_s are the thermal conductivity of the gaseous and solid phases, respectively.

Russel's Eq. for thermal conductivity of a system with cubic pores [221]:

$$k_c = \frac{k_s\left[k_s + V_p^{2/3}(k_g - k_s)\right]}{k_s + (k_g - k_s)\left(V_p^{2/3} - V_p\right)} \tag{3.5}$$

The parametric open-cell model derived based on the fractal theory is described in [222]. The skeletal structure of foams is mimicked as a simple cubic lattice formed by the framework of fibrils (struts) with thickness $2t$ and length L. The effective thermal conductivity of the framework is given by Eq. [222]:

$$k_c = \frac{4k_s t^2 + k_g(L-2t)^2}{L^2} + \frac{4k_s k_g t^2 + k_g(L-2t)t}{2Lk_g t + Lk_s(L-2t)} \tag{3.6}$$

Similarly, Zeng modeled foams as intersecting square rods aligned in a cubic array with thermal conductivity given by the following Eq [223,224]:

$$k_c = k_s\left(\frac{2t}{2t+L}\right)^2 + 2\left[\left(k_s\frac{L}{2t+L}\right)^{-1} + \left(k_g\frac{2t}{2t+L}\right)^{-1}\right]^{-1} + k_g\left(\frac{L}{2t+L}\right)^2 \tag{3.7}$$

The gas conduction depends on the pore size and the mean free path of air molecules in the porous structures [217]. Due to the Knudsen effect, gas conduction decreases significantly if the pore size is smaller than the mean free path of air molecules. The true gaseous conduction k_g used in Eq.(3.8) should be calculated according to Eq [216,222]:

$$k_g = \frac{k_g^0}{1 + 2\beta K_n}, \tag{3.8}$$

where k_g^0 is the thermal conductivity of air in free space, β is a parameter considering the energy transfer between gas molecules and the limiting structure (for air β = 2 [216,225]). The Knudsen number K_n is given by the ratio of the free path of air Λ to the characteristic length, i.e., pore diameter D:

$$K_n = \frac{\Lambda}{D} \tag{3.9}$$

The mean free path of air particles at atmospheric pressure is Λ = 70 – 80 nm [216,219]. Then, according to Eq.(3.6)-(3.7), $K_n \to 0$ for D >> Λ and $k_g \approx k_g^0$.

The thermal conductivity of air was measured using the same method and testing conditions with a free-standing sensor. Its value k_g = 0.0310 ± 0.0007 W/m·K is slightly overestimated compared to the theoretical value of 0.025 W/m·K related to the specificity of the method and ambient conditions. The k_s value found by indirect estimations and parametric fit by the Maxwell-Eucken model Eq.(3.4) is found to be in the range of 1.2 – 3.1 W/m·K. The mean k_s value for both wood and hemp is 1.8 W/m·K. It is found that approximations by Eq.(3.4) and Eq.(3.5) fully coincide, indicating the indifference of the models to the shape of pores at high-volume fractions. Calculations by the unit-cell models given by Eq.(3.4) and Eq.(3.5) with parameters L = 5 mm, 2t = 0.24 mm, k_s = 1.8 W/m·K resulted into k_c values of 0.0327 and 0.0348 W/m·K, respectively. These values are slightly underestimated but still are in reasonable agreement with the experimental data. Differences in measured and calculated k_c values could be related to uncertainties in determining the sizes of the structural elements due to irregular pore size distribution in foams. At the same time, k_c increases with growing k_s. At k_s = 6.0 W/m·K, k_c calculated by Eq.(3.6) and Eq.(3.7) is 0.0421 and 0.0437 W/m·K, respectively. These values are closer to the experimental data.

Radiative heat transfer between the pore walls could significantly contribute to the total heat flow through foams. Due to modelling complexity, the macroscale effective radiative conductivity is often replaced by its microscale equivalent incorporating radiation locally at the pore scale. Considering heat radiation across a spherical pore of diameter *d*, i.e., an air cavity surrounded by a solid material wall boundary, the radiative thermal conductivity can be described with the following Eq. [221]:

$$k_{r,pore} = \frac{8}{3}\varepsilon\sigma d T^3, \tag{3.10}$$

where ε is the radiative emissivity of the matrix walls, and σ is the Stefan-Boltzmann constant. This $k_{r,pore}$ can subsequently be added to the thermal conductivity of gas inside the respective pore (i.e., given by Eq.(3.10)). As seen from Eq.(3.10), the radiation component contribution will significantly increase with the growing temperature. Taking e = 0.9 for natural wood [221] at the ambient temperature of 295 K, $k_{r,pore}$ takes the values of $1.75 \cdot 10^{-8}$ and $1.75 \cdot 10^{-5}$ W/m·K for 5 nm and 5 mm large pores, respectively. The radiation component is more than three orders of magnitude lower than the thermal conductivity of air k_g, thus its contribution is reasonably considered very low. Similar notes on the low contribution of k_r are made in [217,223,225]. In other studies [222], the radiative component contribution is comparable with that for solid conduction, although gas conduction remains the dominant heat transfer mechanism in most low-density foams.

To summarise this discussion, the thermal conductivity of the solid NC network (foam) estimated through a parametric fit with four different models is in the range of 1.2 – 6 W/m·K. These values are well in the range of other studies, e.g., 1.47 W/m·K found from a parametric fit and 0.9 – 5.7 W/m·K found by molecular dynamic simulations for single fibrils [222]. The value also fits well with the averaged value for axial and radial thermal conductivities of different NC-based films [140,217].

3.4.8. Summary

Birchwood and hemp biomass wastes were used and processed into sustainable NC foam materials. The freeze-drying process can achieve controlled density between 2 to 36 g/cc and porosity of 99.7 to 99.9%, resulting in foam materials with enhanced mechanical and thermal insulation properties.

The effect of the NFC content in suspension used for freeze-drying and resulting material density was studied to understand these sustainable foams' compression, thermal degradation, and thermal conductivity. The usage of the hemp NCF for foam preparation strongly enhanced the mechanical properties and thermal conductivity compared to the similar foams obtained from wood NC fibrils, as determined by compression and hot-plate measurements. Thermal degradation analysis showed good thermal stability for both raw and alkaline-treated hemp and wood samples. The elastic modulus reveals a power-law relationship with density increment, and specific strength shows a linear dependence from the cellulose content in suspension used for the freeze-drying process for both types of foams. Accordingly, the thermal conductivity of the obtained NC foams estimated through a parametric fit with four different models is in the range of 34 – 44 mW/m·K.

3.5. Sustainable Foams from Hemp, Lignin, Xylan, Pectin, and Glycerol: Tunable via Reversible Citric Acid Crosslinking for Absorption and Insulation Applications (accepted)

This study investigates the development of sustainable multifunctional foams utilizing hemp stalk waste, lignin, xylan, pectin, glycerol, and citric acid. Using the freeze-drying method for foam formation in combination with industrial waste products and renewable resources, we emphasize a green, scalable material development approach. In total, 25 distinct formulations were prepared and methodically examined, particularly focusing on the roles of citric acid, pectin, and glycerol. Thermal crosslinking, conducted at 140 °C, was analyzed using FTIR, confirming the formation of ester bonds. The microstructural characterization of the foams revealed distinct variations from nanofibrillar to microfibrillar structures based on composition. The bulk density of the foams ranged from 13 to 152 mg/cm^3, and porosity values varied from 97% to 99% for most of the compositions. Foams showed up to 50 g/g water, 51 g/g rapeseed oil, and 46 g/g kerosine absorption. Foam absorption capacity changes were examined through 10 iterative cycles in water, demonstrating that most compositions retained near-original absorption capacities. The addition of glycerol conferred exceptional hydrophobic properties to the foam surfaces, as evidenced by water contact angles ranging between 140° and 150°. The thermal conductivity of foams ranged from 0.040 to 0.046 W/m·K. The mechanical properties of foams were assessed using compression testing, which showed highly tunable structures ranging from soft to rigid. This study illustrates the broad applicability of these foams, emphasizing their utility in thermal insulation, filtration systems, and environmental cleanup, among other potential uses.

3.5.1. Chemical interactions

Figure 3.39 gives insights into the chemical interactions leading to the formation of a crosslinked network for the H- and WM- foams. A detailed investigation of cellulose, xylan, and lignin is provided elsewhere [226-229]. In brief, the stacked fingerprint region from 900 to 1500 cm-1 shows the impact of various component introductions, revealing the creation of a hybrid network surrounding hemp fibrils due to strong intermolecular bonding between components. The reduced intensity of the region from 900 to 1100 cm-1 matches with the changes attributed to various stretching vibrations of the C-O bonds [173]. Moreover, it is clearly seen that the region from 1225 to 1480 cm-1 appears smoother, and the peak intensities for -CH and -CH2 bending and stretching vibrations (1315, 1368, and 1424 cm-1 [226]) are decreasing due to the presence of other components in the formulation. This is visible for all sets of samples, but it is more obvious for H-foams because WM-foams contain high concentrations of lignin and hemicellulose, which interact strongly with the NFC.

H-foams show strongly pronounced characteristic crosslinking peak changes (Figure 3.39(a)), which is reflected in the evident decrease of the broad -OH peak intensity (3040 to 3600 cm-1) and increase in the carbonyl C=O peak intensity (1733 cm-1) representing formed ester bonds [230]. Although this effect is less pronounced in the spectra of WM-foams due to the much larger amount of -OH bonds introduced by lignin and hemicellulose. The WM-foams spectra in Figure 3.39(b) indicate a noticeable shift of the peak assigned to lignin aryl ring

stretching (from 1590 to 1605 cm^{-1}), indicating an electron balance shift caused by the changes of the -OH groups to newly created crosslinks with CA and other components. Due to the substantially lower concentration of lignin, this shift is not pronounced for the H-foams.

Because both introduced components (pectin and glycerol) can covalently crosslink with CA, the maximum peak intensity is found for WM-P0.5-G2-CA1 and H-P0.5-G2-CA1 (Figure 3.39). This could be related to CA being able to achieve a higher conversion of carbonyl groups to esters with a higher amount of available hydroxyl groups. This discovery is consistent with changes in porosity (Table 3.11), where a steady increase in bulk density (Figure 3.41) with the addition of more components and higher concentrations of CA implies that samples become increasingly cross-linked. The tendency toward higher CA concentrations can be seen in Supplementary 10. A similar observation can be reached from mechanical test findings (Figure 3.42), where samples with larger component amounts attained higher modulus and strength values.

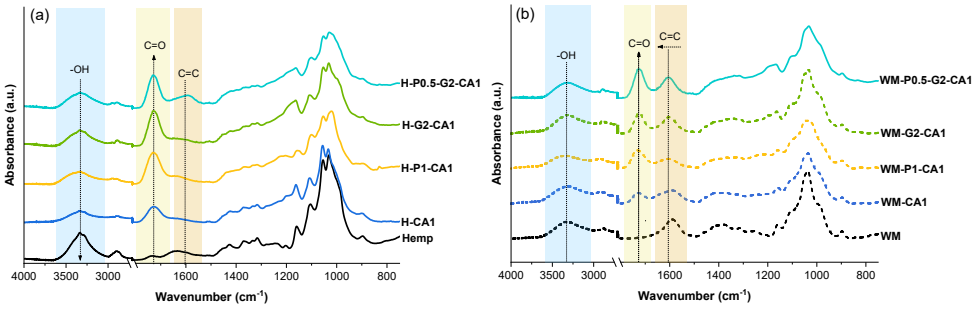

Figure 3.39. FTIR spectra of selected samples for Hemp foams (a), and WM foams (b).

3.5.2 Morphology

The morphologies of foam samples are shown in Figure 3.40. NFC forms robust physical gels in aqueous media due to its elongated fiber length, which culminates in an interwoven network characterized by extensive hydrogen bonding. Existing literature demonstrates that the freeze-drying of NFC tends to yield a sheet-like morphology [231,232], a consequence of the aggregation phenomena inherent to NFC. This particular morphology is heavily influenced by the cooling conditions, a critical factor that poses significant challenges in terms of optimization, especially at an industrial scale [232,233]. While methods such as rapid cooling using liquid nitrogen [234], liquid propane [235], and supercritical drying [234] have been effective in retaining some degree of the fibrillar structure, their practical application on a large scale remains limited. Rapid liquid cooling techniques were avoided in favor of a more scalable and cost-efficient solution, employing a combination of a cooling chamber, capable of reaching temperatures as low as -80 °C, and the addition of tert-butyl alcohol. This strategy facilitated the partial preservation of the nanostructure.

A coexistence of sheet-like and nanofibrillar structures was observed in the context of H- and WM-foams. Previous analyses indicate that hemp comprises approximately 69 wt% cellulose [174], whereas the WM composition is characterized by about 31 wt% cellulose (45

wt% hemp). This compositional difference is instrumental in defining the mixed structure of the foams. Lower cellulose concentrations (WM-foams) promoted a more pronounced sheet-like structure with increased fiber and sheet thickness, a feature that becomes more evident under lower magnification (refer to Supplementary 11 and Supplementary 12).

Incremental increases in the crosslinker (CA) concentration resulted in a morphological transition, introducing micro-sized fiber structures, particularly pronounced in CA5-foams. As the CA concentration increased, there was a noticeable reduction in nanostructured elements, leading to a decrease in the specific surface area of the foams. Comparative analyses of CA0.5-, CA2.5- and CA5-foams leads to the conclusion that the preservation of nanostructured elements is preferable for absorption applications. Thereby favoring a lower concentration of CA. Consequently, CA1-foams were selected over CA0.5-foams for subsequent experiments involving pectin and glycerol additives based on their superior structural rigidity and enhanced shape recovery during absorption cycling, as evidenced in preliminary results (discussed in the following sections).

The integration of pectin into the foams induced significant structural transformations. It is noteworthy that the proportion of pectin utilized is substantial, with the NFC and pectin ratio maintained at 6:1 and 3:2 for H-P0.25-CA1 and H-P1-CA1, respectively. Consequently, pectin constitutes a significant portion of the foam's structural network. Pectin achieved an exceptional distribution through a dissolution process, resulting in a nanofibrillar structure with diameters less than 100 nm. These nanofibrillar networks of pectin efficiently occupied the larger pores between cellulosic structures, contributing to a denser and more refined nanostructured network. For H-P0.25-CA1, the pectin threshold was not fully met, in contrast to H-P1-CA1, which exhibited more comprehensive structural changes. Notably, the structural similarities between H- and WM-foams suggest that pectin's synergistic interactions are not confined to cellulose but extend to its efficacy with xylan and lignin networks. The ability of pectin to fill larger pores with its nanofibrils was also evident in lower SEM magnifications (Supplementary 11 and Supplementary 12). Research by Groult and Budtova on pectin aerogels corroborates the formation of nanofibrils of comparable size [236].

Glycerol acts as a surface coating for biopolymers, thickening existing structural elements and consequently transforming the foam structure into a microfiber-sized network with diameters predominantly exceeding 1 µm. This effect stands in stark contrast to that of pectin. A fibrillar structure emerged in H-G-foams, whereas WM-G-foams also exhibited agglomerates exceeding 5 µm in size. The addition of glycerol effectively nullified the presence of sheet-like structural elements, functioning akin to a “glue”. Distinguishing between G0.5- and G2-foams proved challenging, underscoring glycerol's significant impact on the cohesion of structural elements. Interestingly, the combined application of pectin and glycerol yielded a denser and more agglomerated structure compared to the use of glycerol alone. This phenomenon may be attributed to pectin expanding the surface area of the biopolymer network, thereby promoting a more uniform “coating” distribution of glycerol, which culminates in a densely packed structure.

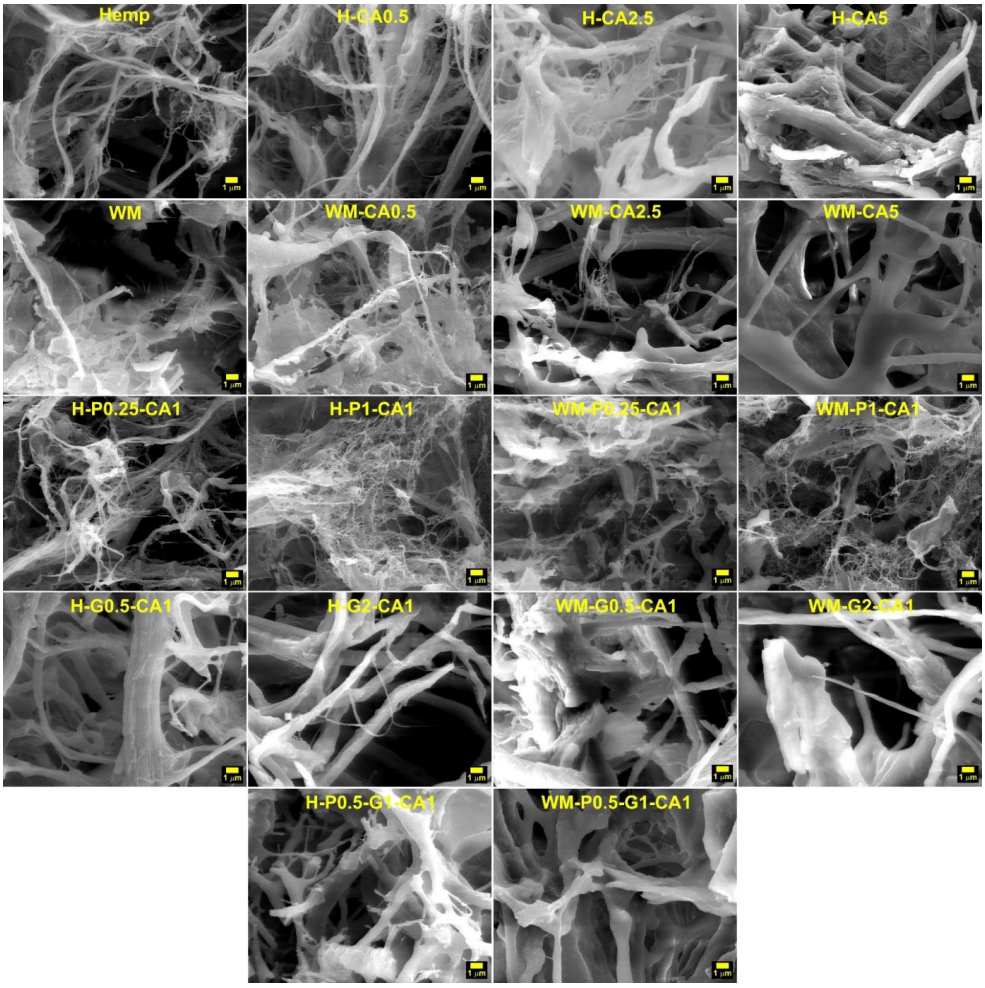

Figure 3.40. SEM micrographs of selected foam samples shown at 5000x magnification.

3.5.3. Mechanical performance

Figure 3.41 graphically represents the bulk density of the foam samples, with observed values spanning from 13 to 152 mg/cm^3. Hemp foam exhibits the lowest bulk density at 13 mg/cc, while WM foam shows a substantial increase, approximately 100% higher, with a density of 27 mg/cm^3. For hemp foam, the crosslinking process with citric acid (CA) results in a nearly linear increase in density, yet the effect on WM foam exhibits a distinctly non-linear pattern. The incorporation of pectin (P) and glycerol (G) into the H-foam formulation results in an approximate 50% increase in density. In contrast, the impact on the WM foam structure shows only a marginal increase in density. Notably, the combined use of pectin and glycerol as hybrid modifiers induces significant structural changes, as evidenced by more than a 2-fold increase in bulk density compared to systems modified with a single additive. A higher glycerol content in the glycerol-to-pectin ratio subsequently reduces the bulk density of both H- and WM-foams.

Table 3.11 shows that most foam samples exhibit porosity ranging from approximately 97% to 99%, underscoring the formation of a highly open and porous structure. These porosity values are in correlation with the observed densities. It is noteworthy that lower porosity values, ranging between 90% and 94%, were exhibited in WM-CA5 and the pectin-glycerol hybrid foams. This reduction in porosity is indicative of a denser and less porous structure, attributable to the increased crosslinking and the synergistic effects of the combined modifiers. These values also correlate well with the volume shrinkage (Table 3.11), measured between gel volume and freeze-dried foam dimensions. Notably, hybrids exhibited shrinkage around 80%, while for other foams, values are around 40%. Like with porosity, WM-CA5 was the exception, with a shrinkage of 64%.

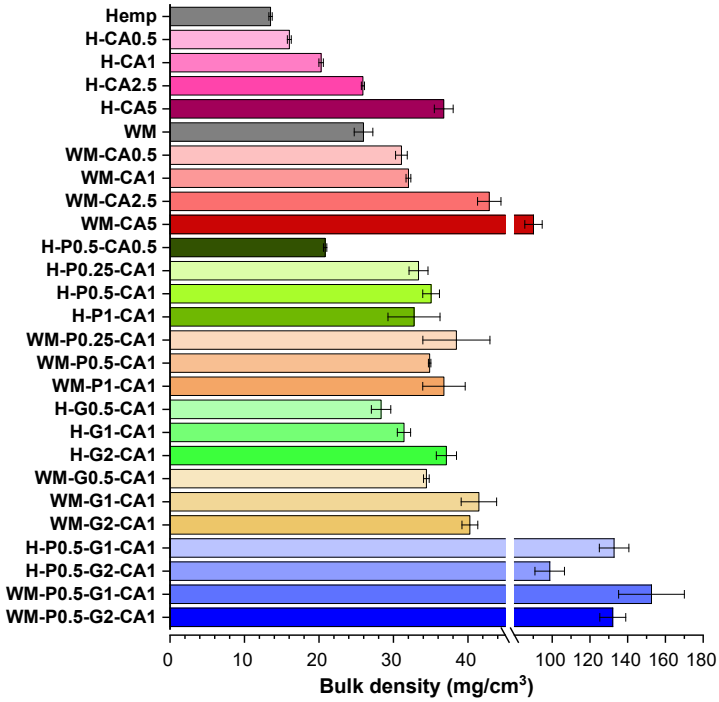

Figure 3.41. Bulk density of all prepared foam samples.

To investigate the impact of crosslinker citric acid, pectin, and glycerol on the mechanical properties of the foams, a series of compressive stress–strain (σ–ε) tests were conducted. Supplementary 13 illustrates the influence of increasing CA concentrations in H- and WM-foams, while Figure 3.42 depicts the compression curves for foams with varied pectin and glycerol contents. Table 3.11 provides a comprehensive summary of the compressive modulus, specific compressive modulus, and specific strength of these foams. The significant differences in foam density required the use of specific values for comparison. Nearly all compositions adhered to cellulose-based lightweight materials' typical compression curve profile [237]. During the initial linear phase, stress increased linearly (up to 10% deformation), indicative of elastic deformation. This was followed by a plateau phase, where stress remained relatively

constant, signifying plastic deformation, observable from 15 to 50% (and in some cases up to 60%) deformation. The final phase, densification, was marked by a significant rise in stress as the foam walls compressed tightly against each other beyond 70% deformation. Notably, hybrid foams with added pectin and glycerol began densification at approximately 60% deformation.

Table 3.11.

Physical properties of the obtained foams: porosity, volume shrinkage, compressive modulus, and specific strength for various strain levels.

Sample	Porosity (%)	Volume shrinkage (%)	$E_{5\%}$ (kPa)	Spec. $E_{5\%}$ (kPa·cm^3/g)	Spec. strength at 5% strain (kPa·cm^3/g)	Spec. strength at 10% strain (kPa·cm^3/g)	Spec. strength at 50% strain (kPa·cm^3/g)
Hemp	99.1±0.01	34.1±1.1	0.096±0.003	7.1±0.2	35.6±1.1	94.9±3.0	709±22
H-CA0.5	98.9±0.02	31.7±0.5	0.109±0.002	6.8±0.1	39.3±0.7	89.7±1.6	749±14
H-CA1	98.6±0.02	42.3±1.8	0.188±0.004	9.3±0.2	70.4±1.5	171±4	1245±26
H-CA2.5	98.3±0.01	35.9±2.4	0.376±0.032	14.5±1.2	139±12	312±27	1727±147
H-CA5	97.5±0.08	37.0±2.4	1.554±0.146	42.3±4.0	576±54	1038±98	2639±248
WM	98.3±0.08	41.6±0.6	0.368±0.042	14.2±1.6	141±16	326±37	1942±222
WM-CA0.5	97.9±0.05	38.0±2.6	0.486±0.058	15.6±1.9	182±21	425±51	3239±387
WM-CA1	97.9±0.02	34.6±0.9	0.982±0.022	30.7±1.7	368±10	738±17	3284±74
WM-CA2.5	97.1±0.11	39.7±2.1	1.515±0.335	35.3±7.8	567±125	1282±284	4592±1015
WM-CA5	94.0±0.31	64.4±1.2	4.559±1.035	50.6±11.5	1716±389	3780±858	11585±2630
H-P0.5-CA0.5	98.6±0.01	33.7±0.6	1.136±0.124	54.5±5.9	422±46	897±98	2928±320
H-P0.25-CA1	97.8±0.08	52.6±2.1	1.372±0.245	41.1±7.3	514±92	1060±189	3817±682
H-P0.5-CA1	97.7±0.07	58.8±2.6	1.556±0.232	44.4±6.6	577±86	1297±193	4603±686
H-P1-CA1	97.8±0.23	44.5±4.5	2.138±0.473	65.3±14.4	793±175	1794±397	6056±1340
WM-P0.25-CA1	97.4±0.30	43.9±5.1	2.060±0.134	53.6±3.5	764±49	1594±104	5248±341
WM-P0.5-CA1	97.7±0.01	35.5±2.8	2.938±0.126	84.3±3.6	1089±46	2113±91	5707±245
WM-P1-CA1	97.5±0.19	33.5±4.1	5.796±0.652	157.6±17.7	2165±243	4981±560	10822±1217
H-G0.5-CA1	98.1±0.09	41.4±5.0	0.237±0.003	8.4±0.1	87.5±4.1	245±3	1475±19
H-G1-CA1	97.9±0.07	36.0±4.0	0.407±0.024	13.0±0.8	151±10	385±23	1883±111
H-G2-CA1	97.5±0.09	34.7±2.4	0.569±0.031	15.3±0.8	212±12	465±25	2520±137
WM-G0.5-CA1	97.7±0.03	32.5±1.0	0.504±0.055	14.6±1.6	187±20	378±41	2239±244
WM-G1-CA1	97.2±0.16	38.2±6.1	0.593±0.073	14.3±1.8	211±26	497±61	2224±274
WM-G2-CA1	97.3±0.07	42.1±3.0	0.777±0.092	19.3±2.3	290±34	575±68	3269±387
H-P0.5-G1-CA1	91.1±0.52	81.7±1.3	24.800±4.342	186.7±32.7	9191±1609	14306±2505	56926±9967
H-P0.5-G2-CA1	93.4±0.52	75.5±2.3	20.000±3.457	202.6±35.0	7412±1281	16307±2819	43540±7526
WM-P0.5-G1-CA1	89.8±1.16	81.6±2.1	46.600±7.762	305.4±50.9	17270±2876	42028±7000	110443±18396
WM-P0.5-G2-CA1	91.2±0.46	79.0±0.6	30.200±5.213	228.6±39.5	11192±1932	26091±4504	74123±12795

The lowest tested amount of crosslinker (CA0.5) had a negligible impact on the mechanical properties of the H- and WM-foams. Porosity and volume shrinkage remained close to the original structure, although a slight increase in density was observed. An increased CA loading resulted in enhanced foam rigidity, as reflected by a rise in the specific compressive modulus, even after accounting for density changes. WM-foams exhibited approximately a 2-fold increase in specific compressive modulus with and without crosslinking compared to H-foams. The exception was H-CA5, which demonstrated only an 18% lower value than WM-CA5. This alignment with high CA loading correlates well with the observed densification of structure in morphological images and density data. A 10-fold increase in CA content (from CA0.5 to CA5) resulted in a 6-fold increase in the specific modulus of H-foams and approximately a 3-fold increase for WM-foams.

Additionally, the specific strength (at 5% strain) exhibited an approximate 15-fold and 12-fold increase for H- and WM-foams, respectively. Surprisingly, at 50% strain, H-foams showed about a 3.5-fold increase, while WM-foams demonstrated approximately a 6-fold increase when comparing CA0.5- and CA5-foams. These differences between compositions could be

attributed to the availability of surface hydroxyl groups (-OH), which are presumed to be more abundant in H-foams. The lower molecular weight of xylan significantly contributes to the WM-foams' ability to form a denser structure, facilitating more hydrogen bonding. Intermolecular bonding plays a pivotal role during the plastic deformation stage, while the effects of covalent crosslinking are more pronounced in the elastic deformation region. This could explain why H-foams showed a higher rigidity increase at 5% strain, while WM-foams at 50% strain.

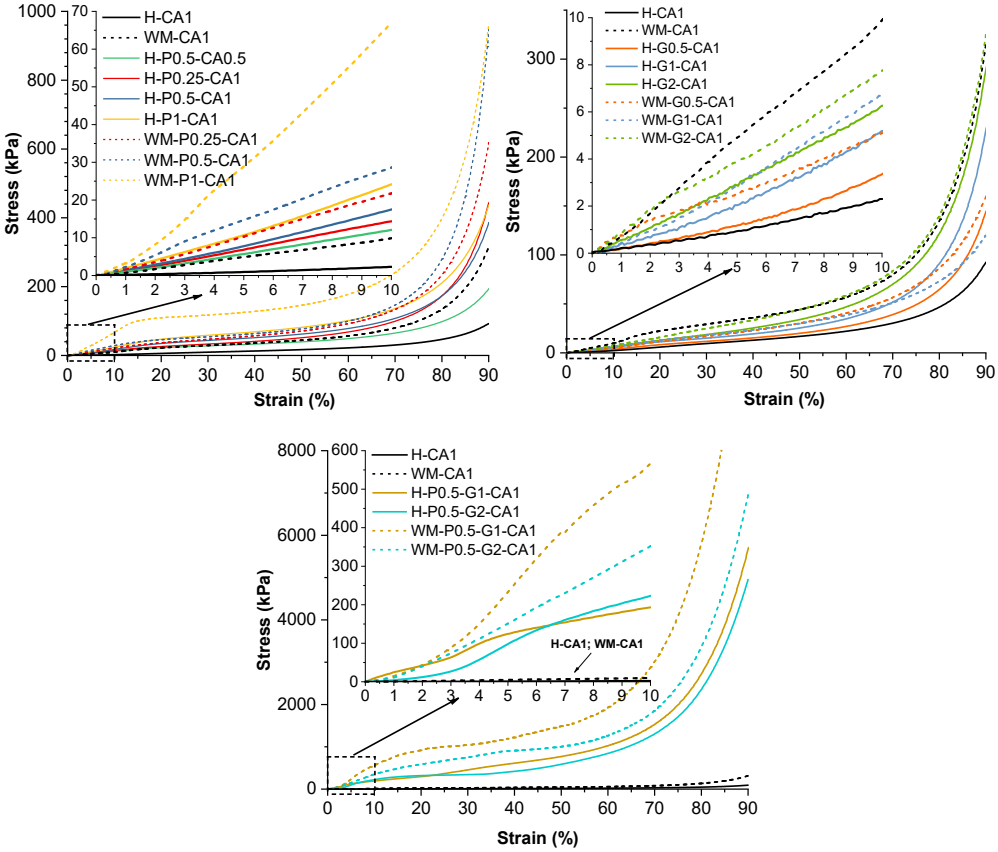

Figure 3.42. Compression curves for foams with varied pectin and glycerol contents.

Given that CA content directly influences mechanical properties, the effects of pectin and glycerol additions were comparable only to H-CA1 and WM-CA1. The significant impact of pectin on mechanical properties was evident during sample preparation. As such, the H-P0.5-CA0.5 composition was formulated more as a conceptual demonstration, showcasing the potential to use a lower CA amount, while the focus was on CA1-foams, as discussed above. H-CA0.5 showed no improvements in specific modulus (measured at 5%) and only a slight increase in specific strength compared to non-crosslinked hemp foams. The addition of 0.5% pectin resulted in an approximately 8-fold increase in specific modulus and an 11-fold

enhancement in specific strength (at 5% strain) compared to H-CA0.5. Most notably, the H-P0.5-CA0.5 foam exhibited a relatively low density compared to other crosslinked foams. The structural rigidity imparted by pectin in H-CA1-foams led to a 4- to 7-fold and 7- to 11-fold improvement in specific modulus and specific strength, respectively. In WM-P-foams, a similar degree of mechanical enhancement was observed, further supporting the SEM observations and demonstrating pectin's compatibility with xylan and lignin.

The incorporation of glycerol improved the mechanical properties of H-foams while conversely diminishing the performance of WM-foams. This differential impact is closely correlated with the observed alterations in nanostructure. In the case of WM-foams, the presence of lignin and xylan appeared to strengthen the structural connections between the nanofibrils. However, glycerol's addition disrupted these links, leading to the formation of agglomerates. Such agglomeration impairs the network's ability to uniformly distribute load, consequently affecting the mechanical performance of the foams. For H-foams, glycerol-induced densification of the fibrillar network, which contributed to increased rigidity. This enhancement, however, came at the expense of the nanostructured network, thereby limiting the potential for mechanical improvement. Given that the resulting modulus and strength values of H-foams were inferior to those of WM-CA1, it becomes evident that glycerol alone is not an optimal additive for producing mechanically robust foams.

Hybrid foam formulations exhibit exceptional rigidity. This characteristic can be partially attributed to the considerable shrinkage observed in these systems. When examining mechanical performance, a remarkable up to 22-fold increase in specific modulus and an impressive up to 131-fold increase in specific strength (measured at 5% strain) were noted when comparing H-CA1 to H-hybrid-foams. While not as impressive, WM-hybrid-foams also show a significant increase in mechanical performance. These findings underscore the significant potential for tailoring the mechanical properties of foams through strategic compositional modifications.

3.5.4. Absorption characterization

Investigating the behavior of ultralight, low-density foams in aqueous environments is crucial for their application in pollution removal from water. Their efficiency in this regard depends on a comprehensive understanding of their interaction with both hydrophobic and hydrophilic substances. In Figure 3.43 water contact angle measurements are presented. All foams were tested without any surface processing, and the contact angle values were examined after 10 s and 60 s. As a result, hydrophilic and hydrophobic foam surfaces can be distinguished.

The base composition analysis reveals that WM-foams demonstrate a pronounced affinity for water, contrasting with H-foams, which exhibit an initial contact angle of approximately 130° across varying concentrations of crosslinking agent CA. Notably, H-CA0.5 foams show a substantial decrease in contact angle over time. With a high concentration of CA, WM-foams approach the hydrophobic characteristics of H-foams, albeit with a gradual water absorption leading to a significant decrease in contact angle after 60 s. The hydrophilic nature of WM-foams is attributed to the presence of xylan, a smaller molecule than cellulose, capable of

forming robust physical crosslinks with cellulose fibrils and filling structural voids. This likely increases surface hydroxyl groups, a tendency that higher CA concentrations can moderate.

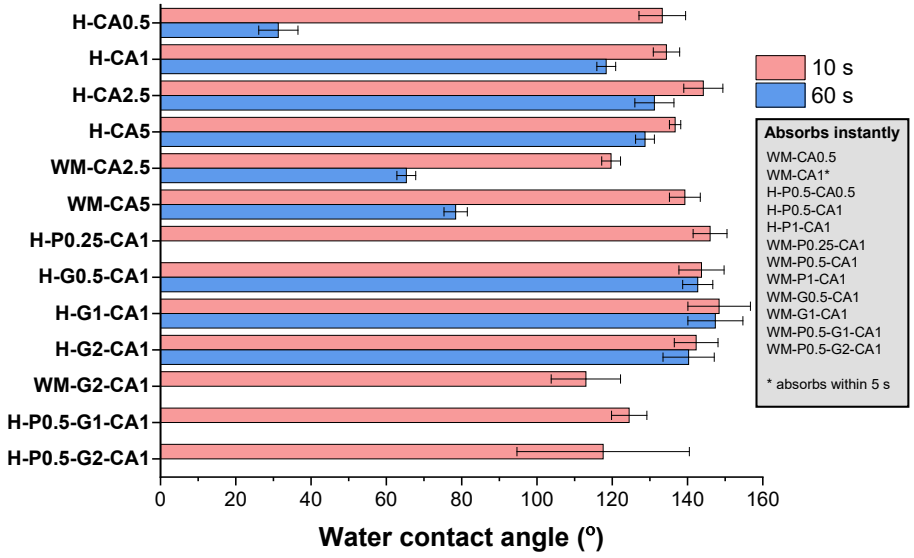

Figure 3.43. Foam water contact angle measurements.

The integration of pectin markedly enhances the hydrophilic properties of the foams, with all compositions except H-P0.25-CA1 instantaneously absorbing water droplets. The pectin's impact is akin to xylan's, with its nanofibrils distinctly visible in SEM. In contrast, glycerol stabilizes contact angles between 140° and 150° for H-G-foams by imparting a hydrophobic effect, though not enough to become superhydrophobic. WM-G-foams, however, fail to attain this stable water-repellent structure.

Figure 3.44 illustrates the differential absorption capacity and selectivity of various foam compositions towards three distinct liquids: water, rapeseed oil, and kerosene (a medium-chain hydrocarbon derived from petroleum distillation). This distinction is crucial as water absorption pertains to the removal of dyes and heavy metals. In contrast, rapeseed oil and kerosene are representative of viscous organic liquids and liquid fuel spills, respectively. Notably, certain foam formulations exhibited pronounced hydrophobicity, resisting water absorption. However, it was discovered that mechanical compression could induce absorption in these hydrophobic foams.

Among the tested compositions, H-CA0.5 demonstrated superior absorption for all three liquids, albeit with limited selectivity towards organic liquids, which it absorbed almost instantaneously, in contrast to its slower water absorption. An increase in CA content correlated with a decrease in overall absorption capacity. However, this was accompanied by an enhanced selectivity for organic liquids in H-foams, with water absorption occurring only when the samples were compressed in water. This inverse relationship between absorption capacity and foam density was consistent across all tested samples.

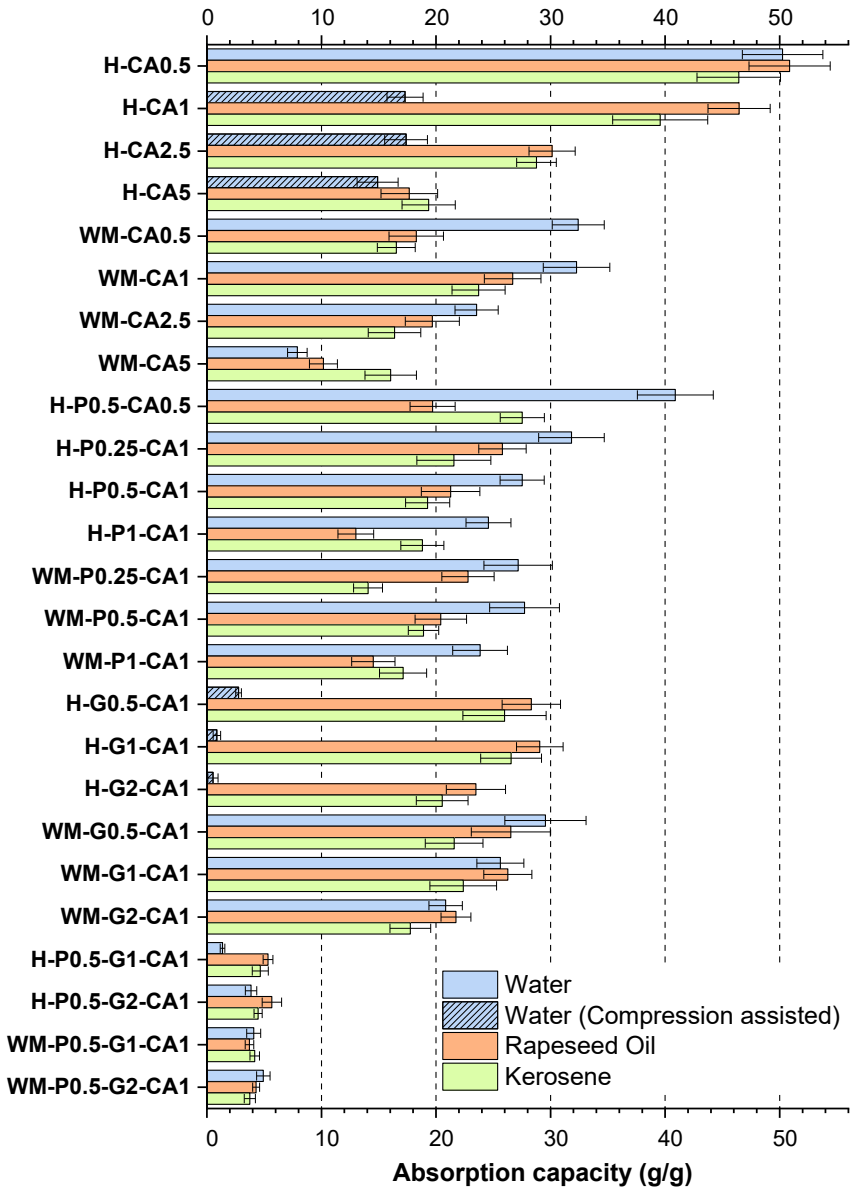

Figure 3.44. Absorption capacity of foam samples in water, rapeseed oil and kerosene.

Pectin foams were remarkable for their rapid absorption rate, which did not discriminate between the tested liquids. Conversely, H-G-foams exhibited exceptional selectivity towards organic liquids, refusing to absorb water even under compression. Hybrid foams, characterized by their high rigidity and volume shrinkage, were deemed unsuitable for absorption applications.

The recyclability of these foams as absorbents was evaluated using water and kerosene (Figures 3.45 and Supplementary 14, respectively). The recycling process entailed compressing the foams to expel absorbed liquids, followed by their re-expansion in the liquid. This approach presented challenges with rapeseed oil, as no foam composition demonstrated recycling potential. H-CA0.5 and H-P0.5-CA0.5 compositions exhibited approximately 1.5 times higher water absorption capacity. Most foams maintained remarkable stability, preserving absorption capacities close to their initial values. The water affinity of pectin foam structures influenced their recycling capacity, averaging around five cycles. H-CA5 foams, however, were too brittle for effective recycling, while others completed up to ten cycles. Notably, H-G-foams showed an increased water absorption capacity, indicating a breakdown of their hydrophobic, crosslinked surface to reveal a more hydrophilic internal structure. Hybrid foams, although recyclable (due to the water plasticization effect), still exhibited relatively low absorption capacities (around 5 to 6 g/g).

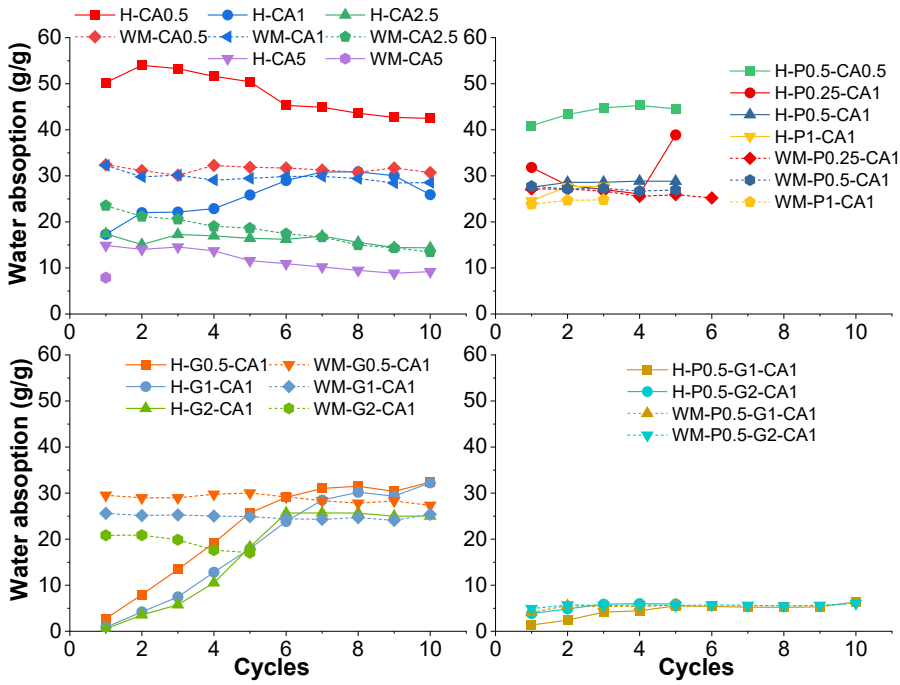

Figure 3.45. Foam recovery capabilities and cycle performance in water.

In the context of kerosene absorption (Supplementary 14), the same H-CA0.5 and H-P0.5-CA0.5 compositions stood out, with similar variants closely following in performance. None of the foams completed ten recycling cycles, with H-P-foams showing the best performance, achieving up to five cycles, followed by H-CA0.5 and H-CA1 with four cycles each. WM- and WM-P-foams were unable to recycle with kerosene, and all glycerol-based foams reached their limit at 2 cycles.

3.5.5. Thermal conductivity

Table 3.12 presents the thermal conductivity, diffusivity, and specific heat of various foam compositions to evaluate their insulation application potential. The highlight of foams is their hydrophobic performance, suggesting their viability as long-term stable thermal insulators. The thermal conductivity of these foams ranges from 0.040 to 0.046 W/m·K, which aligns them with materials like industrial polyurethane foam [238], wool [239], and other high-performance insulation materials [240]. Notably, these values are about 2-fold higher than the best-reported figures for cellulose aerogels [109], reflecting morphological distinctions between foams and aerogels. Intriguingly, foam density showed no significant correlation with thermal conductivity. The thermal diffusivity and specific heat measurements align with expected performance parameters, including their error margins.

Table 3.12.

Thermal conductivity, diffusivity, and specific heat of various foam compositions.

Sample	Th. Conductivity (W/m·K)	Th. Diffusivity (mm^2/s)	Specific Heat (MJ/m^3K)
Hemp	0.044 ± 0.001	0.91 ± 0.17	0.050 ± 0.011
H-CA1	0.041 ± 0.001	0.97 ± 0.19	0.044 ± 0.011
H-CA2.5	0.040 ± 0.000	0.80 ± 0.13	0.052 ± 0.010
WM	0.044 ± 0.001	0.74 ± 0.19	0.064 ± 0.018
WM-CA1	0.045 ± 0.001	0.73 ± 0.16	0.065 ± 0.014
WM-CA2.5	0.045 ± 0.001	1.16 ± 0.23	0.041 ± 0.010
H-P0.25-CA1	0.046 ± 0.002	0.80 ± 0.25	0.063 ± 0.019
H-P1-CA1	0.045 ± 0.001	0.69 ± 0.13	0.068 ± 0.013
WM-P0.25-CA1	0.044 ± 0.002	1.28 ± 0.28	0.036 ± 0.008
WM-P1-CA1	0.044 ± 0.002	0.60 ± 0.16	0.079 ± 0.021
H-G0.5-CA1	0.040 ± 0.001	0.77 ± 0.20	0.055 ± 0.014
H-G2-CA1	0.046 ± 0.002	0.40 ± 0.10	0.124 ± 0.033
WM-G0.5-CA1	0.041 ± 0.001	0.68 ± 0.16	0.063 ± 0.013
WM-G2-CA1	0.045 ± 0.001	0.89 ± 0.20	0.054 ± 0.017

3.5.6. Summary

The study demonstrates the preparation of multifunctional foams with highly tunable properties based on composition. Biobased, biocompatible, and renewable components were selected as the basis for the preparation of thermally crosslinked foams. The investigated properties relate to applications such as insulation, filtration, and environmental cleanup, while areas such as biomedical and sound dampening are applicable but were not explored in this study. Based on the experimental results, the following conclusions are presented:

1. FTIR spectroscopy confirms the formation of a crosslinked hybrid network around hemp fibrils characterized by the formation of ester bonds, particularly pronounced in H-foam spectra.
2. H- and WM-foams exhibit structures ranging from sheet-like to nanofibrillar. Pectin creates a dense network of nanofibrillar structures below 100 nm, while glycerol transforms the structure into a microfiber network with diameters predominantly above 1 μm. The bulk density of foams varies from 13 to 152 mg/cm^3, with H-based ones being the least dense. Porosity values range from 97% to 99%, decreasing to 90%–93% in certain hybrid foams.
3. The specific compressive modulus and specific strength significantly increase with higher CA concentrations. A 10-fold increase in CA concentration results in a 6-fold increase in specific modulus and a 16-fold increase in specific strength (at 5% strain) for H-foams. Pectin improves specific modulus up to 9-fold and specific strength up to 22-fold at 5% strain in H-foams.
4. H-CA0.5 demonstrated the highest absorption capacity for water (50 g/g), rapeseed oil (51 g/g), and kerosene (46 g/g). Pectin integration enhances rapid absorption across all liquids, while glycerol increases hydrophobicity, stabilizing water contact angles between 140° and 150° for H-G-foams. Foams demonstrate good recyclable performance, retaining a high absorption capacity for water after 10 cycles of testing. Kerosene recycling was limited to 5 cycles, while rapeseed could not undergo repeated cycling.
5. The thermal conductivity of the foam's ranges from 0.040 to 0.046 W/m·K, positioning them as viable thermal insulators, especially highly hydrophobic foams.
6. Pectin and glycerol hybrid foams demonstrated exceptional rigidity and mechanical performance, but their structure and shrinkage also limited their potential in the examined application scenarios.

CONCLUSIONS

1. The advanced extraction and manipulation of lignocellulose from diverse biomass sources, including wood pulp, wood dust, and agricultural residues, and its combination with externally sourced hemicellulose and lignin, can create bioplastics and foams which mimic structural and mechanical properties of natural wood.

2. The integration of hybrid modifiers, such as lignin and xylan, into the structure of nanofibrillated cellulose significantly enhances the performance of cellulose nanopapers and foams, and the structure can be regulated by fine-tuning the content of lignin and xylan and by utilizing green chemical functionalization and crosslinking approaches.

3. Through the mechanical processing of hemp stalks and subsequent thermal crosslinking using natural additives, it is possible to develop sustainable bioplastics whose properties range from brittle to ductile (elastic modulus 913-2927 MPa) by systematically adjusting the varying ratios of xylan, citric acid, and other components, highlighting the possibility of creating customizable, eco-friendly materials suitable for various applications.

4. Creating eco-friendly nanolignocellulose foams from wood dust and hemp stalk waste yields lightweight materials with customizable mechanical strength ($E_{5\%}$ 0.17-28.2 kPa), porosity (97.8-99.9 %), and thermal insulation (0.033-0.044 W/m·K). Fine-tuning the nanofibril content allows for tailored properties to meet specific industry needs, while environmentally friendly functionalization methods enable the creation of foams with adjustable properties spanning from soft to rigid (spec. $E_{5\%}$ 6.8-305.4 kPa·cm^3/g). These versatile foams find applications in thermal insulation, filtration systems, environmental cleanup, and more.

5. Cellulose nanopapers display varying degrees of resilience to environmental stressors such as UV radiation, heat, and humidity, with UV-Vis and FTIR spectroscopy revealing that while lignin and xylan components undergo degradation, the core cellulose fibers maintain their structural integrity, demonstrating the potential for cellulose-based plastics in environmentally sensitive applications.

6. The resulting wood mimic materials exhibit a notable array of properties, including high tensile strength, stiffness, thermal stability, and biodegradability. Moreover, they can be tailored to meet specific application requirements, such as packaging materials, construction components, and sorption or separation materials. Furthermore, the sustainable nature of these materials aligns with the principles of the circular economy. By harnessing the abundant resources of cellulose, hemicellulose, and lignin, this thesis represents a step forward in the development of environmentally friendly biomaterials, potentially fostering a greener and more sustainable future.

REFERENCES

1. Rosenboom, J.-G.; Langer, R.; Traverso, G. Bioplastics for a circular economy. *Nature Reviews Materials* **2022**, *7*, 117-137, doi:10.1038/s41578-021-00407-8.
2. Dziuba, R.; Kucharska, M.; Madej-Kiełbik, L.; Sulak, K.; Wiśniewska-Wrona, M. Biopolymers and Biomaterials for Special Applications within the Context of the Circular Economy. *Materials (Basel)* **2021**, *14*, doi:10.3390/ma14247704.
3. Rana, A.K.; Guleria, S.; Gupta, V.K.; Thakur, V.K. Cellulosic pine needles-based biorefinery for a circular bioeconomy. *Bioresource Technology* **2023**, *367*, 128255, doi:https://doi.org/10.1016/j.biortech.2022.128255.
4. Geyer, R.; Jambeck, J.R.; Law, K.L. Production, use, and fate of all plastics ever made. *Science Advances* **2017**, *3*, e1700782, doi:doi:10.1126/sciadv.1700782.
5. Pan, X.; Li, J.; Ma, N.; Ma, X.; Gao, M. Bacterial cellulose hydrogel for sensors. *Chemical Engineering Journal* **2023**, *461*, 142062, doi:https://doi.org/10.1016/j.cej.2023.142062.
6. Lan, Z.; Wang, Y.; Hu, K.; Shi, S.; Meng, Q.; Sun, Q.; Shen, X. Anti-swellable cellulose hydrogel for underwater sensing. *Carbohydrate Polymers* **2023**, *306*, 120541, doi:https://doi.org/10.1016/j.carbpol.2023.120541.
7. Han, X.; Ding, S.; Zhu, L.; Wang, S. Preparation and characterization of flame-retardant and thermal insulating bio-based composite aerogels. *Energy and Buildings* **2023**, *278*, 112656, doi:https://doi.org/10.1016/j.enbuild.2022.112656.
8. Wang, Y.; Yang, J.; Song, Y.; Yang, Q.; Xiong, C.; Shi, Z. Porous and three-dimensional carbon aerogels from nanocellulose/pristine graphene for high-performance supercapacitor electrodes. *Diamond and Related Materials* **2023**, *132*, 109626, doi:https://doi.org/10.1016/j.diamond.2022.109626.
9. Jamróz, E.; Kulawik, P.; Kopel, P. The Effect of Nanofillers on the Functional Properties of Biopolymer-Based Films: A Review. *Polymers* **2019**, *11*, 675.
10. Tyuftin, A.A.; Kerry, J.P. Gelatin films: Study review of barrier properties and implications for future studies employing biopolymer films. *Food Packaging and Shelf Life* **2021**, *29*, 100688, doi:https://doi.org/10.1016/j.fpsl.2021.100688.
11. Temesgen, S.; Rennert, M.; Tesfaye, T.; Nase, M. Review on Spinning of Biopolymer Fibers from Starch. *Polymers* **2021**, *13*, 1121.
12. Gough, C.R.; Rivera-Galletti, A.; Cowan, D.A.; Salas-de la Cruz, D.; Hu, X. Protein and Polysaccharide-Based Fiber Materials Generated from Ionic Liquids: A Review. *Molecules* **2020**, *25*, 3362.
13. Song, B.; Lin, R.; Lam, C.H.; Wu, H.; Tsui, T.-H.; Yu, Y. Recent advances and challenges of inter-disciplinary biomass valorization by integrating hydrothermal and biological techniques. *Renewable and Sustainable Energy Reviews* **2021**, *135*, 110370, doi:https://doi.org/10.1016/j.rser.2020.110370.
14. Burla, F.; Mulla, Y.; Vos, B.E.; Aufderhorst-Roberts, A.; Koenderink, G.H. From mechanical resilience to active material properties in biopolymer networks. *Nature Reviews Physics* **2019**, *1*, 249-263, doi:10.1038/s42254-019-0036-4.
15. Gregory, D.A.; Tripathi, L.; Fricker, A.T.R.; Asare, E.; Orlando, I.; Raghavendran, V.; Roy, I. Bacterial cellulose: A smart biomaterial with diverse applications. *Materials Science and Engineering: R: Reports* **2021**, *145*, 100623, doi:https://doi.org/10.1016/j.mser.2021.100623.
16. Noremylia, M.B.; Hassan, M.Z.; Ismail, Z. Recent advancement in isolation, processing, characterization and applications of emerging nanocellulose: A review.

International Journal of Biological Macromolecules **2022**, *206*, 954-976, doi:https://doi.org/10.1016/j.ijbiomac.2022.03.064.
17. Feng, P.; He, J.; Peng, S.; Gao, C.; Zhao, Z.; Xiong, S.; Shuai, C. Characterizations and interfacial reinforcement mechanisms of multicomponent biopolymer based scaffold. *Materials Science and Engineering: C* **2019**, *100*, 809-825, doi:https://doi.org/10.1016/j.msec.2019.03.030.
18. Pei, Y.; Wang, L.; Tang, K.; Kaplan, D.L. Biopolymer Nanoscale Assemblies as Building Blocks for New Materials: A Review. *Advanced Functional Materials* **2021**, *31*, 2008552, doi:https://doi.org/10.1002/adfm.202008552.
19. Abdul Khalil, H.P.S.; Davoudpour, Y.; Islam, M.N.; Mustapha, A.; Sudesh, K.; Dungani, R.; Jawaid, M. Production and modification of nanofibrillated cellulose using various mechanical processes: A review. *Carbohydrate Polymers* **2014**, *99*, 649-665, doi:https://doi.org/10.1016/j.carbpol.2013.08.069.
20. Ma, H.; Zhou, B.; Li, H.-S.; Li, Y.-Q.; Ou, S.-Y. Green composite films composed of nanocrystalline cellulose and a cellulose matrix regenerated from functionalized ionic liquid solution. *Carbohydrate Polymers* **2011**, *84*, 383-389, doi:https://doi.org/10.1016/j.carbpol.2010.11.050.
21. Fukuzumi, H.; Saito, T.; Iwata, T.; Kumamoto, Y.; Isogai, A. Transparent and high gas barrier films of cellulose nanofibers prepared by TEMPO-mediated oxidation. *Biomacromolecules* **2009**, *10*, 162-165.
22. Moon, R.J.; Martini, A.; Nairn, J.; Simonsen, J.; Youngblood, J. Cellulose nanomaterials review: structure, properties and nanocomposites. *Chemical Society Reviews* **2011**, *40*, 3941-3994, doi:10.1039/C0CS00108B.
23. Kalia, S.; Boufi, S.; Celli, A.; Kango, S. Nanofibrillated cellulose: surface modification and potential applications. *Colloid and Polymer Science* **2014**, *292*, 5-31, doi:10.1007/s00396-013-3112-9.
24. Zhang, J.; Song, H.; Lin, L.; Zhuang, J.; Pang, C.; Liu, S. Microfibrillated cellulose from bamboo pulp and its properties. *Biomass and Bioenergy* **2012**, *39*, 78-83, doi:https://doi.org/10.1016/j.biombioe.2010.06.013.
25. Kargarzadeh, H.; Mariano, M.; Gopakumar, D.; Ahmad, I.; Thomas, S.; Dufresne, A.; Huang, J.; Lin, N. Advances in cellulose nanomaterials. *Cellulose* **2018**, *25*, 2151-2189, doi:10.1007/s10570-018-1723-5.
26. Nie, S.; Zhang, K.; Lin, X.; Zhang, C.; Yan, D.; Liang, H.; Wang, S. Enzymatic pretreatment for the improvement of dispersion and film properties of cellulose nanofibrils. *Carbohydrate Polymers* **2018**, *181*, 1136-1142, doi:https://doi.org/10.1016/j.carbpol.2017.11.020.
27. Osong, S.H.; Norgren, S.; Engstrand, P. Processing of wood-based microfibrillated cellulose and nanofibrillated cellulose, and applications relating to papermaking: a review. *Cellulose* **2016**, *23*, 93-123, doi:10.1007/s10570-015-0798-5.
28. Nechyporchuk, O.; Belgacem, M.N.; Bras, J. Production of cellulose nanofibrils: A review of recent advances. *Industrial Crops and Products* **2016**, *93*, 2-25, doi:https://doi.org/10.1016/j.indcrop.2016.02.016.
29. Iglesias, M.C.; Gomez-Maldonado, D.; Via, B.K.; Jiang, Z.; Peresin, M.S. Pulping Processes and Their Effects on Cellulose Fibers and Nanofibrillated Cellulose Properties: A Review. *Forest Products Journal* **2020**, *70*, 10-21, doi:10.13073/fpj-d-19-00038.
30. Li, T.; Chen, C.; Brozena, A.H.; Zhu, J.Y.; Xu, L.; Driemeier, C.; Dai, J.; Rojas, O.J.; Isogai, A.; Wågberg, L.; et al. Developing fibrillated cellulose as a sustainable technological material. *Nature* **2021**, *590*, 47-56, doi:10.1038/s41586-020-03167-7.

31. Eichhorn, S.J.; Dufresne, A.; Aranguren, M.; Marcovich, N.E.; Capadona, J.R.; Rowan, S.J.; Weder, C.; Thielemans, W.; Roman, M.; Renneckar, S.; et al. Review: current international research into cellulose nanofibres and nanocomposites. *Journal of Materials Science* **2010**, *45*, 1-33, doi:10.1007/s10853-009-3874-0.
32. Seddiqi, H.; Oliaei, E.; Honarkar, H.; Jin, J.; Geonzon, L.C.; Bacabac, R.G.; Klein-Nulend, J. Cellulose and its derivatives: towards biomedical applications. *Cellulose* **2021**, *28*, 1893-1931, doi:10.1007/s10570-020-03674-w.
33. Jusner, P.; Schwaiger, E.; Potthast, A.; Rosenau, T. Thermal stability of cellulose insulation in electrical power transformers – A review. *Carbohydrate Polymers* **2021**, *252*, 117196, doi:https://doi.org/10.1016/j.carbpol.2020.117196.
34. Yi, T.; Zhao, H.; Mo, Q.; Pan, D.; Liu, Y.; Huang, L.; Xu, H.; Hu, B.; Song, H. From Cellulose to Cellulose Nanofibrils—A Comprehensive Review of the Preparation and Modification of Cellulose Nanofibrils. *Materials* **2020**, *13*, 5062.
35. Thakur, V.; Guleria, A.; Kumar, S.; Sharma, S.; Singh, K. Recent advances in nanocellulose processing, functionalization and applications: a review. *Materials Advances* **2021**, *2*, 1872-1895, doi:10.1039/D1MA00049G.
36. Frank, B.P.; Smith, C.; Caudill, E.R.; Lankone, R.S.; Carlin, K.; Benware, S.; Pedersen, J.A.; Fairbrother, D.H. Biodegradation of Functionalized Nanocellulose. *Environmental Science & Technology* **2021**, *55*, 10744-10757, doi:10.1021/acs.est.0c07253.
37. da Costa, F.A.T.; Parra, D.F.; Cardoso, E.C.L.; Güven, O. PLA, PBAT, Cellulose Nanocrystals (CNCs), and Their Blends: Biodegradation, Compatibilization, and Nanoparticle Interactions. *Journal of Polymers and the Environment* **2023**, doi:10.1007/s10924-023-02899-7.
38. Luzi, F.; Torre, L.; Kenny, J.M.; Puglia, D. Bio- and Fossil-Based Polymeric Blends and Nanocomposites for Packaging: Structure–Property Relationship. *Materials* **2019**, *12*, 471.
39. Idumah, C.I.; Zurina, M.; Ogbu, J.; Ndem, J.U.; Igba, E.C. A review on innovations in polymeric nanocomposite packaging materials and electrical sensors for food and agriculture. *Composite Interfaces* **2020**, *27*, 1-72, doi:10.1080/09276440.2019.1600972.
40. Rana, A.K.; Scarpa, F.; Thakur, V.K. Cellulose/polyaniline hybrid nanocomposites: Design, fabrication, and emerging multidimensional applications. *Industrial Crops and Products* **2022**, *187*, 115356, doi:https://doi.org/10.1016/j.indcrop.2022.115356.
41. Ralph, J.; Lapierre, C.; Boerjan, W. Lignin structure and its engineering. *Current Opinion in Biotechnology* **2019**, *56*, 240-249, doi:https://doi.org/10.1016/j.copbio.2019.02.019.
42. Vermaas, J.V.; Crowley, M.F.; Beckham, G.T. A Quantitative Molecular Atlas for Interactions Between Lignin and Cellulose. *ACS Sustainable Chemistry & Engineering* **2019**, *7*, 19570-19583, doi:10.1021/acssuschemeng.9b04648.
43. Yoon, J.; Choi, H.; An, G. Roles of lignin biosynthesis and regulatory genes in plant development. *Journal of Integrative Plant Biology* **2015**, *57*, 902-912, doi:https://doi.org/10.1111/jipb.12422.
44. Terrett, O.M.; Dupree, P. Covalent interactions between lignin and hemicelluloses in plant secondary cell walls. *Current Opinion in Biotechnology* **2019**, *56*, 97-104, doi:https://doi.org/10.1016/j.copbio.2018.10.010.
45. Yu, S.; Wang, M.; Xie, Y.; Qian, W.; Bai, Y.; Feng, Q. Lignin self-assembly and auto-adhesion for hydrophobic cellulose/lignin composite film fabrication. *International Journal of Biological Macromolecules* **2023**, *233*, 123598, doi:https://doi.org/10.1016/j.ijbiomac.2023.123598.

46. Wang, X.; Xia, Q.; Jing, S.; Li, C.; Chen, Q.; Chen, B.; Pang, Z.; Jiang, B.; Gan, W.; Chen, G.; et al. Strong, Hydrostable, and Degradable Straws Based on Cellulose-Lignin Reinforced Composites. *Small* **2021**, *17*, 2008011, doi:https://doi.org/10.1002/smll.202008011.
47. Platnieks, O.; Beluns, S.; Briede, S.; Jurinovs, M.; Gaidukovs, S. Cellulose synergetic interactions with biopolymers: Functionalization for sustainable and green material design. *Industrial Crops and Products* **2023**, *204*, 117310, doi:https://doi.org/10.1016/j.indcrop.2023.117310.
48. Beluns, S.; Platnieks, O.; Gaidukovs, S.; Starkova, O.; Sabalina, A.; Grase, L.; Thakur, V.K.; Gaidukova, G. Lignin and Xylan as Interface Engineering Additives for Improved Environmental Durability of Sustainable Cellulose Nanopapers. *International Journal of Molecular Sciences* **2021**, *22*, 12939.
49. Beluns, S.; Gaidukovs, S.; Platnieks, O.; Barkane, A.; Gaidukova, G.; Grase, L.; Nabels-Sneiders, M.; Kovalovs, A.; Thakur, V.K. Clean manufacturing of cellulose nanopapers by incorporating lignin and xylan as sustainable additives. *Carbohydrate Polymer Technologies and Applications* **2022**, *3*, doi:10.1016/j.carpta.2022.100207.
50. Huang, C.; Dong, H.; Zhang, Z.; Bian, H.; Yong, Q. Procuring the nano-scale lignin in prehydrolyzate as ingredient to prepare cellulose nanofibril composite film with multiple functions. *Cellulose* **2020**, *27*, 9355-9370, doi:10.1007/s10570-020-03427-9.
51. Bian, H.; Gao, Y.; Wang, R.; Liu, Z.; Wu, W.; Dai, H. Contribution of lignin to the surface structure and physical performance of cellulose nanofibrils film. *Cellulose* **2018**, *25*, 1309-1318, doi:10.1007/s10570-018-1658-x.
52. Guo, Y.; Tian, D.; Shen, F.; Yang, G.; Long, L.; He, J.; Song, C.; Zhang, J.; Zhu, Y.; Huang, C.; et al. Transparent Cellulose/Technical Lignin Composite Films for Advanced Packaging. *Polymers* **2019**, *11*, 1455.
53. Bystrzanowska, M.; Pena-Pereira, F.; Marcinkowski, Ł.; Tobiszewski, M. How green are ionic liquids? – A multicriteria decision analysis approach. *Ecotoxicology and Environmental Safety* **2019**, *174*, 455-458, doi:https://doi.org/10.1016/j.ecoenv.2019.03.014.
54. Ma, Y.; Asaadi, S.; Johansson, L.-S.; Ahvenainen, P.; Reza, M.; Alekhina, M.; Rautkari, L.; Michud, A.; Hauru, L.; Hummel, M.; et al. High-Strength Composite Fibers from Cellulose–Lignin Blends Regenerated from Ionic Liquid Solution. *ChemSusChem* **2015**, *8*, 4030-4039, doi:https://doi.org/10.1002/cssc.201501094.
55. Le, N.-D.; Trogen, M.; Varley, R.J.; Hummel, M.; Byrne, N. Chemically Accelerated Stabilization of a Cellulose–Lignin Precursor as a Route to High Yield Carbon Fiber Production. *Biomacromolecules* **2022**, *23*, 839-846, doi:10.1021/acs.biomac.1c01226.
56. Bengtsson, A.; Hecht, P.; Sommertune, J.; Ek, M.; Sedin, M.; Sjöholm, E. Carbon Fibers from Lignin–Cellulose Precursors: Effect of Carbonization Conditions. *ACS Sustainable Chemistry & Engineering* **2020**, *8*, 6826-6833, doi:10.1021/acssuschemeng.0c01734.
57. Trogen, M.; Le, N.-D.; Sawada, D.; Guizani, C.; Lourençon, T.V.; Pitkänen, L.; Sixta, H.; Shah, R.; O'Neill, H.; Balakshin, M.; et al. Cellulose-lignin composite fibres as precursors for carbon fibres. Part 1 – Manufacturing and properties of precursor fibres. *Carbohydrate Polymers* **2021**, *252*, 117133, doi:https://doi.org/10.1016/j.carbpol.2020.117133.
58. Jiang, B.; Chen, C.; Liang, Z.; He, S.; Kuang, Y.; Song, J.; Mi, R.; Chen, G.; Jiao, M.; Hu, L. Lignin as a Wood-Inspired Binder Enabled Strong, Water Stable, and Biodegradable Paper for Plastic Replacement. *Advanced Functional Materials* **2020**, *30*, 1906307, doi:https://doi.org/10.1002/adfm.201906307.

59. Xia, Z.; Li, J.; Zhang, J.; Zhang, X.; Zheng, X.; Zhang, J. Processing and valorization of cellulose, lignin and lignocellulose using ionic liquids. *Journal of Bioresources and Bioproducts* **2020**, *5*, 79-95, doi:https://doi.org/10.1016/j.jobab.2020.04.001.
60. Dai, L.; Zhu, W.; Lu, J.; Kong, F.; Si, C.; Ni, Y. A lignin-containing cellulose hydrogel for lignin fractionation. *Green Chemistry* **2019**, *21*, 5222-5230, doi:10.1039/C9GC01975H.
61. Kumar, R.; Butreddy, A.; Kommineni, N.; Reddy, P.G.; Bunekar, N.; Sarkar, C.; Dutt, S.; Mishra, V.K.; Aadil, K.R.; Mishra, Y.K.; et al. Lignin: Drug/Gene Delivery and Tissue Engineering Applications. *Int J Nanomedicine* **2021**, *16*, 2419-2441, doi:10.2147/IJN.S303462.
62. Ali, D.A.; Mehanna, M.M. Role of lignin-based nanoparticles in anticancer drug delivery and bioimaging: An up-to-date review. *International Journal of Biological Macromolecules* **2022**, *221*, 934-953, doi:https://doi.org/10.1016/j.ijbiomac.2022.09.007.
63. Tian, D.; Guo, Y.; Huang, M.; Zhao, L.; Deng, S.; Deng, O.; Zhou, W.; Hu, J.; Shen, F. Bacterial cellulose/lignin nanoparticles composite films with retarded biodegradability. *Carbohydrate Polymers* **2021**, *274*, 118656, doi:https://doi.org/10.1016/j.carbpol.2021.118656.
64. Lobato-Peralta, D.R.; Duque-Brito, E.; Villafán-Vidales, H.I.; Longoria, A.; Sebastian, P.J.; Cuentas-Gallegos, A.K.; Arancibia-Bulnes, C.A.; Okoye, P.U. A review on trends in lignin extraction and valorization of lignocellulosic biomass for energy applications. *Journal of Cleaner Production* **2021**, *293*, 126123, doi:https://doi.org/10.1016/j.jclepro.2021.126123.
65. Bhatnagar, A.; Sain, M. Processing of Cellulose Nanofiber-reinforced Composites. *Journal of Reinforced Plastics and Composites* **2005**, *24*, 1259-1268, doi:10.1177/0731684405049864.
66. Qaseem, M.F.; Shaheen, H.; Wu, A.-M. Cell wall hemicellulose for sustainable industrial utilization. *Renewable and Sustainable Energy Reviews* **2021**, *144*, 110996, doi:https://doi.org/10.1016/j.rser.2021.110996.
67. Rao, J.; Lv, Z.; Chen, G.; Peng, F. Hemicellulose: Structure, chemical modification, and application. *Progress in Polymer Science* **2023**, *140*, 101675, doi:https://doi.org/10.1016/j.progpolymsci.2023.101675.
68. Hallac, B.B.; Ragauskas, A.J. Analyzing cellulose degree of polymerization and its relevancy to cellulosic ethanol. *Biofuels, Bioproducts and Biorefining* **2011**, *5*, 215-225, doi:https://doi.org/10.1002/bbb.269.
69. Ren, J.-L.; Sun, R.-C. Chapter 4 - Hemicelluloses. In *Cereal Straw as a Resource for Sustainable Biomaterials and Biofuels*, Sun, R.-C., Ed.; Elsevier: Amsterdam, 2010; pp. 73-130.
70. Kabel, M.A.; van den Borne, H.; Vincken, J.-P.; Voragen, A.G.J.; Schols, H.A. Structural differences of xylans affect their interaction with cellulose. *Carbohydrate Polymers* **2007**, *69*, 94-105, doi:https://doi.org/10.1016/j.carbpol.2006.09.006.
71. Arola, S.; Malho, J.M.; Laaksonen, P.; Lille, M.; Linder, M.B. The role of hemicellulose in nanofibrillated cellulose networks. *Soft Matter* **2013**, *9*, 1319-1326, doi:10.1039/C2SM26932E.
72. Abdulkhani, A.; Najd Mazhar, A.; Hedjazi, S.; Hamzeh, Y. Preparation of xylan bio-composite films reinforced with oxidized carboxymethyl cellulose and nanocellulose. *Polymer Bulletin* **2020**, *77*, 6227-6239, doi:10.1007/s00289-019-03075-5.
73. Taylor, L.; Phipps, J.; Blackburn, S.; Greenwood, R.; Skuse, D. Using fibre property measurements to predict the tensile index of microfibrillated cellulose nanopaper. *Cellulose* **2020**, *27*, 6149-6162, doi:10.1007/s10570-020-03226-2.

74. Berglund, J.; Mikkelsen, D.; Flanagan, B.M.; Dhital, S.; Gaunitz, S.; Henriksson, G.; Lindström, M.E.; Yakubov, G.E.; Gidley, M.J.; Vilaplana, F. Wood hemicelluloses exert distinct biomechanical contributions to cellulose fibrillar networks. *Nature Communications* **2020**, *11*, 4692, doi:10.1038/s41467-020-18390-z.
75. Tedeschi, G.; Guzman-Puyol, S.; Ceseracciu, L.; Paul, U.C.; Picone, P.; Di Carlo, M.; Athanassiou, A.; Heredia-Guerrero, J.A. Multifunctional Bioplastics Inspired by Wood Composition: Effect of Hydrolyzed Lignin Addition to Xylan–Cellulose Matrices. *Biomacromolecules* **2020**, *21*, 910-920, doi:10.1021/acs.biomac.9b01569.
76. Szymańska-Chargot, M.; Chylińska, M.; Cybulska, J.; Kozioł, A.; Pieczywek, P.M.; Zdunek, A. Simultaneous influence of pectin and xyloglucan on structure and mechanical properties of bacterial cellulose composites. *Carbohydrate Polymers* **2017**, *174*, 970-979, doi:https://doi.org/10.1016/j.carbpol.2017.07.004.
77. Whitney, S.E.C.; Brigham, J.E.; Darke, A.H.; Reid, J.S.G.; Gidley, M.J. In vitro assembly of cellulose/xyloglucan networks: ultrastructural and molecular aspects. *The Plant Journal* **1995**, *8*, 491-504, doi:https://doi.org/10.1046/j.1365-313X.1995.8040491.x.
78. Chibrikov, V.; Pieczywek, P.M.; Zdunek, A. Tailor-Made Biosystems - Bacterial Cellulose-Based Films with Plant Cell Wall Polysaccharides. *Polymer Reviews* **2023**, *63*, 40-66, doi:10.1080/15583724.2022.2067869.
79. Hu, W.; Chen, S.; Wu, D.; Zhu, K.; Ye, X. Physicochemical and macromolecule properties of RG-I enriched pectin from citrus wastes by manosonication extraction. *International Journal of Biological Macromolecules* **2021**, *176*, 332-341.
80. Lin, D.; Lopez-Sanchez, P.; Selway, N.; Gidley, M.J. Viscoelastic properties of pectin/cellulose composites studied by QCM-D and oscillatory shear rheology. *Food Hydrocolloids* **2018**, *79*, 13-19, doi:https://doi.org/10.1016/j.foodhyd.2017.12.019.
81. Peaucelle, A.; Braybrook, S.; Höfte, H. Cell wall mechanics and growth control in plants: the role of pectins revisited. *Frontiers in plant science* **2012**, *3*, 121.
82. Wang, T.; Park, Y.B.; Cosgrove, D.J.; Hong, M. Cellulose-Pectin Spatial Contacts Are Inherent to Never-Dried Arabidopsis Primary Cell Walls: Evidence from Solid-State Nuclear Magnetic Resonance *Plant Physiology* **2015**, *168*, 871-884, doi:10.1104/pp.15.00665.
83. Broxterman, S.E.; Schols, H.A. Interactions between pectin and cellulose in primary plant cell walls. *Carbohydrate Polymers* **2018**, *192*, 263-272, doi:https://doi.org/10.1016/j.carbpol.2018.03.070.
84. Cacicedo, M.L.; Islan, G.A.; Drachemberg, M.F.; Alvarez, V.A.; Bartel, L.C.; Bolzán, A.D.; Castro, G.R. Hybrid bacterial cellulose–pectin films for delivery of bioactive molecules. *New Journal of Chemistry* **2018**, *42*, 7457-7467.
85. Chang, L.; Chang, R.; Shen, J.; Wang, Y.; Song, H.; Kang, X.; Zhao, Y.; Guo, S.; Qin, J. Self-healing pectin/cellulose hydrogel loaded with limonin as TMEM16A inhibitor for lung adenocarcinoma treatment. *International Journal of Biological Macromolecules* **2022**, *219*, 754-766, doi:https://doi.org/10.1016/j.ijbiomac.2022.08.037.
86. Eivazzadeh-Keihan, R.; Ahmadpour, F.; Aliabadi, H.A.M.; Radinekiyan, F.; Maleki, A.; Madanchi, H.; Mahdavi, M.; Shalan, A.E.; Lanceros-Méndez, S. Pectin-cellulose hydrogel, silk fibroin and magnesium hydroxide nanoparticles hybrid nanocomposites for biomedical applications. *International Journal of Biological Macromolecules* **2021**, *192*, 7-15.
87. Lopez-Sanchez, P.; Martinez-Sanz, M.; Bonilla, M.R.; Wang, D.; Gilbert, E.P.; Stokes, J.R.; Gidley, M.J. Cellulose-pectin composite hydrogels: Intermolecular

interactions and material properties depend on order of assembly. *Carbohydrate Polymers* **2017**, *162*, 71-81.
88. Garcia, M.A.V.T.; Garcia, C.F.; Faraco, A.A.G. Pharmaceutical and Biomedical Applications of Native and Modified Starch: A Review. *Starch - Stärke* **2020**, *72*, 1900270, doi:https://doi.org/10.1002/star.201900270.
89. Abdul Khalil, H.P.S.; Saurabh, C.K.; Tye, Y.Y.; Lai, T.K.; Easa, A.M.; Rosamah, E.; Fazita, M.R.N.; Syakir, M.I.; Adnan, A.S.; Fizree, H.M.; et al. Seaweed based sustainable films and composites for food and pharmaceutical applications: A review. *Renewable and Sustainable Energy Reviews* **2017**, *77*, 353-362, doi:https://doi.org/10.1016/j.rser.2017.04.025.
90. Tavares, K.M.; de Campos, A.; Mitsuyuki, M.C.; Luchesi, B.R.; Marconcini, J.M. Corn and cassava starch with carboxymethyl cellulose films and its mechanical and hydrophobic properties. *Carbohydrate Polymers* **2019**, *223*, 115055.
91. Ek, P.; Gu, B.-J.; Saunders, S.R.; Huber, K.; Ganjyal, G.M. Exploration of physicochemical properties and molecular interactions between cellulose and high-amylose cornstarch during extrusion processing. *Current Research in Food Science* **2021**, *4*, 588-597.
92. Chen, J.; Wang, X.; Long, Z.; Wang, S.; Zhang, J.; Wang, L. Preparation and performance of thermoplastic starch and microcrystalline cellulose for packaging composites: Extrusion and hot pressing. *International Journal of Biological Macromolecules* **2020**, *165*, 2295-2302, doi:https://doi.org/10.1016/j.ijbiomac.2020.10.117.
93. Hassan, M.M.; Tucker, N.; Le Guen, M.J. Thermal, mechanical and viscoelastic properties of citric acid-crosslinked starch/cellulose composite foams. *Carbohydrate Polymers* **2020**, *230*, 115675, doi:https://doi.org/10.1016/j.carbpol.2019.115675.
94. Souza, A.G.; Ferreira, R.R.; Paula, L.C.; Mitra, S.K.; Rosa, D.S. Starch-based films enriched with nanocellulose-stabilized Pickering emulsions containing different essential oils for possible applications in food packaging. *Food Packaging and Shelf Life* **2021**, *27*, 100615.
95. Nessi, V.; Falourd, X.; Maigret, J.-E.; Cahier, K.; D'orlando, A.; Descamps, N.; Gaucher, V.; Chevigny, C.; Lourdin, D. Cellulose nanocrystals-starch nanocomposites produced by extrusion: Structure and behavior in physiological conditions. *Carbohydrate Polymers* **2019**, *225*, 115123.
96. Ghasemlou, M.; Daver, F.; Ivanova, E.P.; Murdoch, B.J.; Adhikari, B. Use of synergistic interactions to fabricate transparent and mechanically robust nanohybrids based on starch, non-isocyanate polyurethanes, and cellulose nanocrystals. *ACS Applied Materials & Interfaces* **2020**, *12*, 47865-47878.
97. Jin, H.; Zha, C.; Gu, L. Direct dissolution of cellulose in NaOH/thiourea/urea aqueous solution. *Carbohydrate Research* **2007**, *342*, 851-858, doi:https://doi.org/10.1016/j.carres.2006.12.023.
98. Fauziyah, M.a.; Widiyastuti, W.; Balgis, R.; Setyawan, H. Production of cellulose aerogels from coir fibers via an alkali–urea method for sorption applications. *Cellulose* **2019**, *26*, 9583-9598, doi:10.1007/s10570-019-02753-x.
99. Budtova, T. Cellulose II aerogels: a review. *Cellulose* **2019**, *26*, 81-121, doi:10.1007/s10570-018-2189-1.
100. Mohd, N.; Draman, S.F.S.; Salleh, M.S.N.; Yusof, N.B. Dissolution of cellulose in ionic liquid: A review. *AIP Conference Proceedings* **2017**, *1809*, doi:10.1063/1.4975450.
101. Verma, C.; Mishra, A.; Chauhan, S.; Verma, P.; Srivastava, V.; Quraishi, M.A.; Ebenso, E.E. Dissolution of cellulose in ionic liquids and their mixed cosolvents: A

review. *Sustainable Chemistry and Pharmacy* **2019**, *13*, 100162, doi:https://doi.org/10.1016/j.scp.2019.100162.
102. Chen, Y.-L.; Zhang, X.; You, T.-T.; Xu, F. Deep eutectic solvents (DESs) for cellulose dissolution: a mini-review. *Cellulose* **2019**, *26*, 205-213, doi:10.1007/s10570-018-2130-7.
103. Budtova, T.; Aguilera, D.A.; Beluns, S.; Berglund, L.; Chartier, C.; Espinosa, E.; Gaidukovs, S.; Klimek-kopyra, A.; Kmita, A.; Lachowicz, D.; et al. Biorefinery approach for aerogels. *Polymers* **2020**, *12*, 1-63, doi:10.3390/polym12122779.
104. Klein, M.; Poverenov, E. Natural biopolymer-based hydrogels for use in food and agriculture. *Journal of the Science of Food and Agriculture* **2020**, *100*, 2337-2347, doi:https://doi.org/10.1002/jsfa.10274.
105. Ahmed, E.M. Hydrogel: Preparation, characterization, and applications: A review. *Journal of Advanced Research* **2015**, *6*, 105-121, doi:https://doi.org/10.1016/j.jare.2013.07.006.
106. Cascone, S.; Lamberti, G. Hydrogel-based commercial products for biomedical applications: A review. *International Journal of Pharmaceutics* **2020**, *573*, 118803, doi:https://doi.org/10.1016/j.ijpharm.2019.118803.
107. Wei, G.; Zhang, J.; Usuelli, M.; Zhang, X.; Liu, B.; Mezzenga, R. Biomass vs inorganic and plastic-based aerogels: Structural design, functional tailoring, resource-efficient applications and sustainability analysis. *Progress in Materials Science* **2022**, *125*, 100915, doi:https://doi.org/10.1016/j.pmatsci.2021.100915.
108. García-González, C.A.; Sosnik, A.; Kalmár, J.; De Marco, I.; Erkey, C.; Concheiro, A.; Alvarez-Lorenzo, C. Aerogels in drug delivery: From design to application. *Journal of Controlled Release* **2021**, *332*, 40-63, doi:https://doi.org/10.1016/j.jconrel.2021.02.012.
109. Chen, Y.; Zhang, L.; Yang, Y.; Pang, B.; Xu, W.; Duan, G.; Jiang, S.; Zhang, K. Recent Progress on Nanocellulose Aerogels: Preparation, Modification, Composite Fabrication, Applications. *Advanced Materials* **2021**, *33*, 2005569, doi:https://doi.org/10.1002/adma.202005569.
110. Poursorkhabi, V.; Abdelwahab, M.A.; Misra, M.; Khalil, H.; Gharabaghi, B.; Mohanty, A.K. Processing, Carbonization, and Characterization of Lignin Based Electrospun Carbon Fibers: A Review. *Frontiers in Energy Research* **2020**, *8*, doi:10.3389/fenrg.2020.00208.
111. Khalid, M.Y.; Arif, Z.U. Novel biopolymer-based sustainable composites for food packaging applications: A narrative review. *Food Packaging and Shelf Life* **2022**, *33*, 100892, doi:https://doi.org/10.1016/j.fpsl.2022.100892.
112. Cui, C.; Fu, Q.; Meng, L.; Hao, S.; Dai, R.; Yang, J. Recent Progress in Natural Biopolymers Conductive Hydrogels for Flexible Wearable Sensors and Energy Devices: Materials, Structures, and Performance. *ACS Applied Bio Materials* **2021**, *4*, 85-121, doi:10.1021/acsabm.0c00807.
113. Van Vlierberghe, S.; Dubruel, P.; Schacht, E. Biopolymer-Based Hydrogels As Scaffolds for Tissue Engineering Applications: A Review. *Biomacromolecules* **2011**, *12*, 1387-1408, doi:10.1021/bm200083n.
114. Reddy, M.S.B.; Ponnamma, D.; Choudhary, R.; Sadasivuni, K.K. A Comparative Review of Natural and Synthetic Biopolymer Composite Scaffolds. *Polymers* **2021**, *13*, 1105.
115. Ambekar, R.S.; Kandasubramanian, B. Progress in the Advancement of Porous Biopolymer Scaffold: Tissue Engineering Application. *Industrial & Engineering Chemistry Research* **2019**, *58*, 6163-6194, doi:10.1021/acs.iecr.8b05334.

116. Chatterjee, S.; Hui, P.C.-l. Review of Applications and Future Prospects of Stimuli-Responsive Hydrogel Based on Thermo-Responsive Biopolymers in Drug Delivery Systems. *Polymers* **2021**, *13*, 2086.
117. Hasnain, M.S.; Ahmed, S.A.; Alkahtani, S.; Milivojevic, M.; Kandar, C.C.; Dhara, A.K.; Nayak, A.K. Biopolymers for Drug Delivery. In *Advanced Biopolymeric Systems for Drug Delivery*, Nayak, A.K., Hasnain, M.S., Eds.; Springer International Publishing: Cham, 2020; pp. 1-29.
118. Segal, L.; Creely, J.J.; Martin, A.E.; Conrad, C.M. An Empirical Method for Estimating the Degree of Crystallinity of Native Cellulose Using the X-Ray Diffractometer. *Textile Research Journal* **1959**, *29*, 786-794, doi:10.1177/004051755902901003.
119. Leung, A.C.W.; Lam, E.; Chong, J.; Hrapovic, S.; Luong, J.H.T. Reinforced plastics and aerogels by nanocrystalline cellulose. *Journal of Nanoparticle Research* **2013**, *15*, doi:10.1007/s11051-013-1636-z.
120. Henriksson, M.; Berglund, L.A.; Isaksson, P.; Lindström, T.; Nishino, T. Cellulose Nanopaper Structures of High Toughness. *Biomacromolecules* **2008**, *9*, 1579-1585, doi:10.1021/bm800038n.
121. Robles, E.; Izaguirre, N.; Martin, A.; Moschou, D.; Labidi, J. Assessment of Bleached and Unbleached Nanofibers from Pistachio Shells for Nanopaper Making. *Molecules* **2021**, *26*, 1371.
122. Hanhikoski, S.; Solala, I.; Lahtinen, P.; Niemelä, K.; Vuorinen, T. Fibrillation and characterization of lignin-containing neutral sulphite (NS) pulps rich in hemicelluloses and anionic charge. *Cellulose* **2020**, *27*, 7203-7214, doi:10.1007/s10570-020-03237-z.
123. Goksu, E.I.; Karamanlioglu, M.; Bakir, U.; Yilmaz, L.; Yilmazer, U. Production and Characterization of Films from Cotton Stalk Xylan. *Journal of Agricultural and Food Chemistry* **2007**, *55*, 10685-10691, doi:10.1021/jf071893i.
124. Hansen, N.M.L.; Blomfeldt, T.O.J.; Hedenqvist, M.S.; Plackett, D.V. Properties of plasticized composite films prepared from nanofibrillated cellulose and birch wood xylan. *Cellulose* **2012**, *19*, 2015-2031, doi:10.1007/s10570-012-9764-7.
125. Isobe, N.; Kasuga, T.; Nogi, M. Clear transparent cellulose nanopaper prepared from a concentrated dispersion by high-humidity drying. *RSC Advances* **2018**, *8*, 1833-1837, doi:10.1039/C7RA12672G.
126. Hubbe, M.A.; Tayeb, P.; Joyce, M.; Tyagi, P.; Kehoe, M.; Dimic-Misic, K.; Pal, L. Rheology of Nanocellulose-rich Aqueous Suspensions: A Review. *2017* **2017**, *12*, 106.
127. Liu, L.; Cui, B.; Tan, L.; Wang, W. Improving the combination of cellulose and lignin using xylan as a compatibilizer. *Cellulose* **2021**, *28*, 5335-5349, doi:10.1007/s10570-021-03864-0.
128. Linder, Å.; Bergman, R.; Bodin, A.; Gatenholm, P. Mechanism of Assembly of Xylan onto Cellulose Surfaces. *Langmuir* **2003**, *19*, 5072-5077, doi:10.1021/la0341355.
129. Auzins, J.; Janushevskis, A.; Janushevskis, J.; Skukis, E. Software EDAOpt for experimental design, analysis and multiobjective robust optimization. *OPT-i 2014 - 1st International Conference on Engineering and Applied Sciences Optimization, Proceedings* **2014**, 1055-1077.
130. Atmakuri, A.; Palevicius, A.; Vilkauskas, A.; Janusas, G. Review of Hybrid Fiber Based Composites with Nano Particles—Material Properties and Applications. *Polymers* **2020**, *12*, 2088.
131. Nunna, S.; Chandra, P.R.; Shrivastava, S.; Jalan, A. A review on mechanical behavior of natural fiber based hybrid composites. *Journal of Reinforced Plastics and Composites* **2012**, *31*, 759-769, doi:10.1177/0731684412444325.

132. Zhang, N.; Tao, P.; Lu, Y.; Nie, S. Effect of lignin on the thermal stability of cellulose nanofibrils produced from bagasse pulp. *Cellulose* **2019**, *26*, 7823-7835, doi:10.1007/s10570-019-02657-w.
133. I.P., M.; B., W.; Tamrin; H., I.; J.A., M. Thermal and Morphology Properties of Cellulose Nanofiber from TEMPO-oxidized Lower part of Empty Fruit Bunches (LEFB). *Open Chemistry* **2019**, *17*, 526-536, doi:doi:10.1515/chem-2019-0063.
134. Shen, D.; Zhang, L.; Xue, J.; Guan, S.; Liu, Q.; Xiao, R. Thermal degradation of xylan-based hemicellulose under oxidative atmosphere. *Carbohydr Polym* **2015**, *127*, 363-371, doi:10.1016/j.carbpol.2015.03.067.
135. Mtibe, A.; Linganiso, L.Z.; Mathew, A.P.; Oksman, K.; John, M.J.; Anandjiwala, R.D. A comparative study on properties of micro and nanopapers produced from cellulose and cellulose nanofibres. *Carbohydr Polym* **2015**, *118*, 1-8, doi:10.1016/j.carbpol.2014.10.007.
136. Sethi, J.; Visanko, M.; Osterberg, M.; Sirvio, J.A. A fast method to prepare mechanically strong and water resistant lignocellulosic nanopapers. *Carbohydr Polym* **2019**, *203*, 148-156, doi:10.1016/j.carbpol.2018.09.037.
137. Brillard, A.; Habermacher, D.; Brilhac, J.-F. Thermal degradations of used cotton fabrics and of cellulose: kinetic and heat transfer modeling. *Cellulose* **2017**, *24*, 1579-1595, doi:10.1007/s10570-017-1200-6.
138. Isaac, A.; de Paula, J.; Viana, C.M.; Henriques, A.B.; Malachias, A.; Montoro, L.A. From nano- to micrometer scale: the role of microwave-assisted acid and alkali pretreatments in the sugarcane biomass structure. *Biotechnol Biofuels* **2018**, *11*, 73, doi:10.1186/s13068-018-1071-6.
139. Shen, D.; Ye, J.; Xiao, R.; Zhang, H. TG-MS analysis for thermal decomposition of cellulose under different atmospheres. *Carbohydr Polym* **2013**, *98*, 514-521, doi:10.1016/j.carbpol.2013.06.031.
140. Uetani, K.; Hatori, K. Thermal conductivity analysis and applications of nanocellulose materials. *Science and Technology of Advanced Materials* **2017**, *18*, 877-892, doi:10.1080/14686996.2017.1390692.
141. Diaz, J.A.; Ye, Z.; Wu, X.; Moore, A.L.; Moon, R.J.; Martini, A.; Boday, D.J.; Youngblood, J.P. Thermal Conductivity in Nanostructured Films: From Single Cellulose Nanocrystals to Bulk Films. *Biomacromolecules* **2014**, *15*, 4096-4101, doi:10.1021/bm501131a.
142. Wang, J.; Kasuya, K.; Koga, H.; Nogi, M.; Uetani, K. Thermal Conductivity Analysis of Chitin and Deacetylated-Chitin Nanofiber Films under Dry Conditions. *Nanomaterials (Basel)* **2021**, *11*, doi:10.3390/nano11030658.
143. Gaidukovs, S.; Zukulis, E.; Bochkov, I.; Vaivodiss, R.; Gaidukova, G. Enhanced mechanical, conductivity, and dielectric characteristics of ethylene vinyl acetate copolymer composite filled with carbon nanotubes. *Journal of Thermoplastic Composite Materials* **2018**, *31*, 1161-1180, doi:10.1177/0892705717734603.
144. Bertasius, P.; Macutkevic, J.; Banys, J.; Gaidukovs, S.; Barkane, A.; Vaivodiss, R. Synergy effects in dielectric and thermal properties of layered ethylene vinyl acetate composites with carbon and Fe3O4 nanoparticles. *Journal of Applied Polymer Science* **2020**, *137*, 48814, doi:https://doi.org/10.1002/app.48814.
145. Kontturi, K.S.; Lee, K.-Y.; Jones, M.P.; Sampson, W.W.; Bismarck, A.; Kontturi, E. Influence of biological origin on the tensile properties of cellulose nanopapers. *Cellulose* **2021**, *28*, 6619-6628, doi:10.1007/s10570-021-03935-2.
146. Zhong, L.-X.; Peng, X.-W.; Yang, D.; Cao, X.-F.; Sun, R.-C. Long-Chain Anhydride Modification: A New Strategy for Preparing Xylan Films. *Journal of Agricultural and Food Chemistry* **2013**, *61*, 655-661, doi:10.1021/jf304818f.

147. Desai, R.L.; Shields, J.A. Photochemical degradation of cellulose material. *Die Makromolekulare Chemie* **1969**, *122*, 134-144, doi:https://doi.org/10.1002/macp.1969.021220111.
148. Łojewski, T.; Miśkowiec, P.; Missori, M.; Lubańska, A.; Proniewicz, L.M.; Łojewska, J. FTIR and UV/vis as methods for evaluation of oxidative degradation of model paper: DFT approach for carbonyl vibrations. *Carbohydrate Polymers* **2010**, *82*, 370-375, doi:https://doi.org/10.1016/j.carbpol.2010.04.087.
149. Zięba-Palus, J.; Trzcińska, B.; Wesełucha-Birczyńska, A.; Moskal, P.; Sacharz, J. The sequence of changes observed during degradation process of paper by the use of UV/VIS and FTIR spectrometry with application of the PCA and 2D correlation method for forensic purposes. *Journal of Molecular Structure* **2020**, *1205*, 127651, doi:https://doi.org/10.1016/j.molstruc.2019.127651.
150. Gao, Y.; Lipton, A.S.; Wittmer, Y.; Murray, D.T.; Mortimer, J.C. A grass-specific cellulose–xylan interaction dominates in sorghum secondary cell walls. *Nature Communications* **2020**, *11*, 6081, doi:10.1038/s41467-020-19837-z.
151. Sarosi, O.P.; Bischof, R.H.; Potthast, A. Tailoring Pulp Cellulose with Electron Beam Irradiation: Effects of Lignin and Hemicellulose. *ACS Sustainable Chemistry & Engineering* **2020**, *8*, 7235-7243, doi:10.1021/acssuschemeng.0c02165.
152. Lin, Y.; King, J.Y.; Karlen, S.D.; Ralph, J. Using 2D NMR spectroscopy to assess effects of UV radiation on cell wall chemistry during litter decomposition. *Biogeochemistry* **2015**, *125*, 427-436, doi:10.1007/s10533-015-0132-1.
153. Budischowsky, D.; Zwirchmayr, N.S.; Hosoya, T.; Bacher, M.; Hettegger, H.; Potthast, A.; Rosenau, T. Degradation of cellulosic key chromophores by ozone: a mechanistic and kinetic study. *Cellulose* **2021**, *28*, 6051-6071, doi:10.1007/s10570-021-03909-4.
154. Abral, H.; Ariksa, J.; Mahardika, M.; Handayani, D.; Aminah, I.; Sandrawati, N.; Sugiarti, E.; Muslimin, A.N.; Rosanti, S.D. Effect of heat treatment on thermal resistance, transparency and antimicrobial activity of sonicated ginger cellulose film. *Carbohydrate Polymers* **2020**, *240*, 116287, doi:https://doi.org/10.1016/j.carbpol.2020.116287.
155. Pishnamazi, M.; Hafizi, H.; Shirazian, S.; Culebras, M.; Walker, G.M.; Collins, M.N. Design of Controlled Release System for Paracetamol Based on Modified Lignin. *Polymers* **2019**, *11*, 1059.
156. Liu, J.; Chinga-Carrasco, G.; Cheng, F.; Xu, W.; Willför, S.; Syverud, K.; Xu, C. Hemicellulose-reinforced nanocellulose hydrogels for wound healing application. *Cellulose* **2016**, *23*, 3129-3143, doi:10.1007/s10570-016-1038-3.
157. Stevanic, J.S.; Bergström, E.M.; Gatenholm, P.; Berglund, L.; Salmén, L. Arabinoxylan/nanofibrillated cellulose composite films. *Journal of Materials Science* **2012**, *47*, 6724-6732, doi:10.1007/s10853-012-6615-8.
158. Jankowska, A.; Rybak, K.; Nowacka, M.; Boruszewski, P. Insight of Weathering Processes Based on Monitoring Surface Characteristic of Tropical Wood Species. *Coatings* **2020**, *10*, 877.
159. Volkmer, T.; Noël, M.; Arnold, M.; Strautmann, J. Analysis of lignin degradation on wood surfaces to create a UV-protecting cellulose rich layer. *International Wood Products Journal* **2016**, *7*, 156-164, doi:10.1080/20426445.2016.1200826.
160. Cadena, E.M.; Vidal, T.; Torres, A.L. Influence of the hexenuronic acid content on refining and ageing in eucalyptus TCF pulp. *Bioresource Technology* **2010**, *101*, 3554-3560, doi:https://doi.org/10.1016/j.biortech.2009.11.105.

161. Cirule, D.; Kuka, E.; Kevers, M.; Andersone, I.; Andersons, B. Photodegradation of Unmodified and Thermally Modified Wood Due to Indoor Lighting. *Forests* **2021**, *12*, doi:10.3390/f12081060.
162. Cogulet, A.; Blanchet, P.; Landry, V. Wood degradation under UV irradiation: A lignin characterization. *Journal of Photochemistry and Photobiology B: Biology* **2016**, *158*, 184-191, doi:https://doi.org/10.1016/j.jphotobiol.2016.02.030.
163. Ksibi, M.; Ben Amor, S.; Cherif, S.; Elaloui, E.; Houas, A.; Elaloui, M. Photodegradation of lignin from black liquor using a UV/TiO2 system. *Journal of Photochemistry and Photobiology A: Chemistry* **2003**, *154*, 211-218, doi:https://doi.org/10.1016/S1010-6030(02)00316-7.
164. Chaochanchaikul, K.; Jayaraman, K.; Rosarpitak, V.; Sombatsompop, P.D.N. INFLUENCE OF LIGNIN CONTENT ON PHOTODEGRADATION IN WOOD/HDPE COMPOSITES UNDER UV WEATHERING. *2011* **2011**, *7*, 18.
165. Mosca Conte, A.; Pulci, O.; Knapik, A.; Bagniuk, J.; Del Sole, R.; Lojewska, J.; Missori, M. Role of Cellulose Oxidation in the Yellowing of Ancient Paper. *Physical Review Letters* **2012**, *108*, 158301, doi:10.1103/PhysRevLett.108.158301.
166. Ahn, K.; Zaccaron, S.; Zwirchmayr, N.S.; Hettegger, H.; Hofinger, A.; Bacher, M.; Henniges, U.; Hosoya, T.; Potthast, A.; Rosenau, T. Yellowing and brightness reversion of celluloses: CO or COOH, who is the culprit? *Cellulose* **2019**, *26*, 429-444, doi:10.1007/s10570-018-2200-x.
167. Dupont, A.-L.; Egasse, C.; Morin, A.; Vasseur, F. Comprehensive characterisation of cellulose- and lignocellulose-degradation products in aged papers: Capillary zone electrophoresis of low-molar mass organic acids, carbohydrates, and aromatic lignin derivatives. *Carbohydrate Polymers* **2007**, *68*, 1-16, doi:https://doi.org/10.1016/j.carbpol.2006.07.005.
168. Sadeghifar, H.; Ragauskas, A. Lignin as a UV Light Blocker—A Review. *Polymers* **2020**, *12*, 1134.
169. Liu, Y.; Hu, T.; Wu, Z.; Zeng, G.; Huang, D.; Shen, Y.; He, X.; Lai, M.; He, Y. Study on biodegradation process of lignin by FTIR and DSC. *Environmental Science and Pollution Research* **2014**, *21*, 14004-14013, doi:10.1007/s11356-014-3342-5.
170. Ebringerová, A.; Novotná, Z.; Kačuráková, M.; Machová, E. Chemical modification of beechwood xylan with p-carboxybenzyl bromide. *Journal of Applied Polymer Science* **1996**, *62*, 1043-1047, doi:https://doi.org/10.1002/(SICI)1097-4628(19961114)62:7<1043::AID-APP10>3.0.CO;2-7.
171. Benítez, A.J.; Walther, A. Cellulose nanofibril nanopapers and bioinspired nanocomposites: a review to understand the mechanical property space. *Journal of Materials Chemistry A* **2017**, *5*, 16003-16024, doi:10.1039/C7TA02006F.
172. Srinivas, K.; Pandey, K.K. Photodegradation of thermally modified wood. *Journal of Photochemistry and Photobiology B: Biology* **2012**, *117*, 140-145, doi:https://doi.org/10.1016/j.jphotobiol.2012.09.013.
173. Abidi, N.; Cabrales, L.; Haigler, C.H. Changes in the cell wall and cellulose content of developing cotton fibers investigated by FTIR spectroscopy. *Carbohydrate Polymers* **2014**, *100*, 9-16, doi:https://doi.org/10.1016/j.carbpol.2013.01.074.
174. Beluns, S.; Gaidukovs, S.; Platnieks, O.; Gaidukova, G.; Mierina, I.; Grase, L.; Starkova, O.; Brazdausks, P.; Thakur, V.K. From Wood and Hemp Biomass Wastes to Sustainable Nanocellulose Foams. *Industrial Crops and Products* **2021**, *170*, 113780, doi:https://doi.org/10.1016/j.indcrop.2021.113780.
175. Rana, R.; Langenfeld-Heyser, R.; Finkeldey, R.; Polle, A. FTIR spectroscopy, chemical and histochemical characterisation of wood and lignin of five tropical timber

wood species of the family of Dipterocarpaceae. *Wood Science and Technology* **2010**, *44*, 225-242, doi:10.1007/s00226-009-0281-2.
176. Österberg, M.; Sipponen, M.H.; Mattos, B.D.; Rojas, O.J. Spherical lignin particles: a review on their sustainability and applications. *Green Chemistry* **2020**, *22*, 2712-2733, doi:10.1039/d0gc00096e.
177. Aguirre-Loredo, R.Y.; Rodríguez-Hernández, A.I.; Morales-Sánchez, E.; Gómez-Aldapa, C.A.; Velazquez, G. Effect of equilibrium moisture content on barrier, mechanical and thermal properties of chitosan films. *Food Chemistry* **2016**, *196*, 560-566, doi:https://doi.org/10.1016/j.foodchem.2015.09.065.
178. Cazón, P.; Velázquez, G.; Vázquez, M. Regenerated cellulose films combined with glycerol and polyvinyl alcohol: Effect of moisture content on the physical properties. *Food Hydrocolloids* **2020**, *103*, 105657, doi:https://doi.org/10.1016/j.foodhyd.2020.105657.
179. Guo, X.; Wu, Y.; Xie, X. Water vapor sorption properties of cellulose nanocrystals and nanofibers using dynamic vapor sorption apparatus. *Scientific Reports* **2017**, *7*, 14207, doi:10.1038/s41598-017-14664-7.
180. Cazón, P.; Velázquez, G.; Vázquez, M. Bacterial cellulose films: Evaluation of the water interaction. *Food Packaging and Shelf Life* **2020**, *25*, 100526, doi:https://doi.org/10.1016/j.fpsl.2020.100526.
181. Awad, S.A.; Mahini, S.S.; Tucker, S.J.; Fellows, C.M. Evaluation of the performance of microcrystalline cellulose in retarding degradation of two epoxy resin systems. *International Journal of Polymer Analysis and Characterization* **2019**, *24*, 150-168, doi:10.1080/1023666X.2018.1562597.
182. Dufresne, A. Nanocellulose Processing Properties and Potential Applications. *Current Forestry Reports* **2019**, *5*, 76-89, doi:10.1007/s40725-019-00088-1.
183. Nascimento, E.S.; Barros, M.O.; Cerqueira, M.A.; Lima, H.L.; Borges, M.d.F.; Pastrana, L.M.; Gama, F.M.; Rosa, M.F.; Azeredo, H.M.C.; Gonçalves, C. All-cellulose nanocomposite films based on bacterial cellulose nanofibrils and nanocrystals. *Food Packaging and Shelf Life* **2021**, *29*, 100715, doi:https://doi.org/10.1016/j.fpsl.2021.100715.
184. Xiong, R.; Han, Y.; Wang, Y.; Zhang, W.; Zhang, X.; Lu, C. Flexible, highly transparent and iridescent all-cellulose hybrid nanopaper with enhanced mechanical strength and writable surface. *Carbohydrate Polymers* **2014**, *113*, 264-271, doi:https://doi.org/10.1016/j.carbpol.2014.06.069.
185. Stepan, A.M.; Ansari, F.; Berglund, L.; Gatenholm, P. Nanofibrillated cellulose reinforced acetylated arabinoxylan films. *Composites Science and Technology* **2014**, *98*, 72-78, doi:https://doi.org/10.1016/j.compscitech.2014.04.010.
186. Santucci, B.S.; Bras, J.; Belgacem, M.N.; Curvelo, A.A.d.S.; Pimenta, M.T.B. Evaluation of the effects of chemical composition and refining treatments on the properties of nanofibrillated cellulose films from sugarcane bagasse. *Industrial Crops and Products* **2016**, *91*, 238-248, doi:https://doi.org/10.1016/j.indcrop.2016.07.017.
187. Branca, C.; Di Blasi, C. Kinetic assessment of the thermal decomposition of hemp fiber and the impact of pretreatments. *Journal of Thermal Analysis and Calorimetry* **2022**, doi:10.1007/s10973-022-11663-3.
188. Soares, S.; Ricardo, N.M.P.S.; Heatley, F.; Rodrigues, E. Low temperature thermal degradation of cellulosic insulating paper in air and transformer oil. *Polymer International* **2001**, *50*, 303-308, doi:https://doi.org/10.1002/pi.625.
189. Wang, X.; Partlow, B.; Liu, J.; Zheng, Z.; Su, B.; Wang, Y.; Kaplan, D.L. Injectable silk-polyethylene glycol hydrogels. *Acta Biomaterialia* **2015**, *12*, 51-61, doi:https://doi.org/10.1016/j.actbio.2014.10.027.

190. Lin, C.-C.; Anseth, K.S. PEG Hydrogels for the Controlled Release of Biomolecules in Regenerative Medicine. *Pharmaceutical Research* **2009**, *26*, 631-643, doi:10.1007/s11095-008-9801-2.
191. Shi, J.; Yu, L.; Ding, J. PEG-based thermosensitive and biodegradable hydrogels. *Acta Biomaterialia* **2021**, *128*, 42-59, doi:https://doi.org/10.1016/j.actbio.2021.04.009.
192. Stojkov, G.; Niyazov, Z.; Picchioni, F.; Bose, R.K. Relationship between Structure and Rheology of Hydrogels for Various Applications. *Gels* **2021**, *7*, 255.
193. Winter, H.H.; Morganelli, P.; Chambon, F. Stoichiometry effects on rheology of model polyurethanes at the gel point. *Macromolecules* **1988**, *21*, 532-535, doi:10.1021/ma00180a048.
194. Kudahettige-Nilsson, R.L.; Ullsten, H.; Henriksson, G. Plastic composites made from glycerol, citric acid, and forest components. *BioResources* **2019**, *13*, 6600-6612, doi:10.15376/biores.13.3. 6600-6612.
195. Li, J.; Liu, Y.; Sun, B.; Zhang, R. Improving the wet strength of hemicelluloses based composite films by citric acid crosslinking. *Journal of Wood Chemistry and Technology* **2021**, *41*, 1-9, doi:10.1080/02773813.2020.1847147.
196. Oh, S.Y.; Yoo, D.I.; Shin, Y.; Seo, G. FTIR analysis of cellulose treated with sodium hydroxide and carbon dioxide. *Carbohydrate Research* **2005**, *340*, 417-428, doi:https://doi.org/10.1016/j.carres.2004.11.027.
197. Terpáková, E.; Kidalová, L.; Eštoková, A.; Čigášová, J.; Števulová, N. Chemical Modification of Hemp Shives and their Characterization. *Procedia Engineering* **2012**, *42*, 931-941, doi:https://doi.org/10.1016/j.proeng.2012.07.486.
198. Beh, C.Y.; Cheng, E.M.; Mohd Nasir, N.F.; Abdul Majid, M.S.; Khor, S.F.; Mohd Jamir, M.R.; Mohd Tarmizi, E.Z.; Lee, K.Y. Dielectric Properties of Hydrothermally Modified Potato, Corn, and Rice Starch. *Agriculture* **2022**, *12*, 783.
199. Hasanin, M.; Labeeb, A.M. Dielectric properties of nicotinic acid/methyl cellulose composite via "green" method for anti-static charge applications. *Materials Science and Engineering: B* **2021**, *263*, 114797, doi:https://doi.org/10.1016/j.mseb.2020.114797.
200. Ning, X.; Feng, H.; Zhang, H.; Liu, P.; Xiang, Z.; Peng, Z. Dielectric properties of multi-layer epoxy resinimpregnated crepe paper composites. *IEEE Transactions on Dielectrics and Electrical Insulation* **2015**, *22*, 161-168, doi:10.1109/TDEI.2014.004526.
201. Kargarzadeh, H.; Ahmad, I.; Abdullah, I.; Dufresne, A.; Zainudin, S.Y.; Sheltami, R.M. Effects of hydrolysis conditions on the morphology, crystallinity, and thermal stability of cellulose nanocrystals extracted from kenaf bast fibers. *Cellulose* **2012**, *19*, 855-866, doi:10.1007/s10570-012-9684-6.
202. Foster, E.J.; Moon, R.J.; Agarwal, U.P.; Bortner, M.J.; Bras, J.; Camarero-Espinosa, S.; Chan, K.J.; Clift, M.J.D.; Cranston, E.D.; Eichhorn, S.J.; et al. Current characterization methods for cellulose nanomaterials. *Chemical Society Reviews* **2018**, *47*, 2609-2679, doi:10.1039/C6CS00895J.
203. Maurer, H.W. Chapter 18 - Starch in the Paper Industry. In *Starch (Third Edition)*, BeMiller, J., Whistler, R., Eds.; Academic Press: San Diego, 2009; pp. 657-713.
204. Zhong, L.; Fu, S.; Peng, X.; Zhan, H.; Sun, R. Colloidal stability of negatively charged cellulose nanocrystalline in aqueous systems. *Carbohydrate Polymers* **2012**, *90*, 644-649, doi:10.1016/j.carbpol.2012.05.091.
205. Rahbar Shamskar, K.; Heidari, H.; Rashidi, A. Preparation and evaluation of nanocrystalline cellulose aerogels from raw cotton and cotton stalk. *Industrial Crops and Products* **2016**, *93*, 203-211, doi:10.1016/j.indcrop.2016.01.044.

206. Tian, C.; Yi, J.; Wu, Y.; Wu, Q.; Qing, Y.; Wang, L. Preparation of highly charged cellulose nanofibrils using high-pressure homogenization coupled with strong acid hydrolysis pretreatments. *Carbohydrate Polymers* **2016**, *136*, 485-492, doi:10.1016/j.carbpol.2015.09.055.
207. Sanchez, R.; Espinosa, E.; Dominguez-Robles, J.; Loaiza, J.M.; Rodriguez, A. Isolation and characterization of lignocellulose nanofibers from different wheat straw pulps. *International Journal of Biological Macromolecules* **2016**, *92*, 1025-1033, doi:10.1016/j.ijbiomac.2016.08.019.
208. Chen, W.; Yu, H.; Liu, Y.; Chen, P.; Zhang, M.; Hai, Y. Individualization of cellulose nanofibers from wood using high-intensity ultrasonication combined with chemical pretreatments. *Carbohydrate Polymers* **2011**, *83*, 1804-1811, doi:10.1016/j.carbpol.2010.10.040.
209. Chen, W.; Li, Q.; Wang, Y.; Yi, X.; Zeng, J.; Yu, H.; Liu, Y.; Li, J. Comparative study of aerogels obtained from differently prepared nanocellulose fibers. *ChemSusChem* **2014**, *7*, 154-161, doi:10.1002/cssc.201300950.
210. Pacaphol, K.; Aht-Ong, D. Preparation of hemp nanofibers from agricultural waste by mechanical defibrillation in water. *Journal of Cleaner Production* **2017**, *142*, 1283-1295, doi:10.1016/j.jclepro.2016.09.008.
211. Santmarti, A.; Lee, K.-Y. Crystallinity and Thermal Stability of Nanocellulose. 2018.
212. Platnieks, O.; Gaidukovs, S.; Barkane, A.; Sereda, A.; Gaidukova, G.; Grase, L.; Thakur, V.K.; Filipova, I.; Fridrihsone, V.; Skute, M.; et al. Bio-based poly(butylene succinate)/microcrystalline cellulose/nanofibrillated cellulose-based sustainable polymer composites: Thermo-mechanical and biodegradation studies. *Polymers* **2020**, *12*, 1-20, doi:10.3390/polym12071472.
213. Atiqah, M.S.N.; Gopakumar, D.A.; F, A.T.O.; Pottathara, Y.B.; Rizal, S.; Aprilia, N.A.S.; Hermawan, D.; Paridah, M.T.T.; Thomas, S.; H, P.S.A. Extraction of Cellulose Nanofibers via Eco-friendly Supercritical Carbon Dioxide Treatment Followed by Mild Acid Hydrolysis and the Fabrication of Cellulose Nanopapers. *Polymers (Basel)* **2019**, *11*, doi:10.3390/polym11111813.
214. Rege, A.; Schestakow, M.; Karadagli, I.; Ratke, L.; Itskov, M. Micro-mechanical modelling of cellulose aerogels from molten salt hydrates. *Soft Matter* **2016**, *12*, 7079-7088, doi:10.1039/c6sm01460g.
215. Han, J.; Yue, Y.; Wu, Q.; Huang, C.; Pan, H.; Zhan, X.; Mei, C.; Xu, X. Effects of nanocellulose on the structure and properties of poly(vinyl alcohol)-borax hybrid foams. *Cellulose* **2017**, *24*, 4433-4448, doi:10.1007/s10570-017-1409-4.
216. Gupta, P.; Singh, B.; Agrawal, A.K.; Maji, P.K. Low density and high strength nanofibrillated cellulose aerogel for thermal insulation application. *Materials & Design* **2018**, *158*, 224-236, doi:10.1016/j.matdes.2018.08.031.
217. Apostolopoulou-Kalkavoura, V.; Munier, P.; Bergström, L. Thermally Insulating Nanocellulose-Based Materials. *Advanced Materials n/a*, 2001839, doi:https://doi.org/10.1002/adma.202001839.
218. Long, L.Y.; Weng, Y.X.; Wang, Y.Z. Cellulose Aerogels: Synthesis, Applications, and Prospects. *Polymers (Basel)* **2018**, *10*, doi:10.3390/polym10060623.
219. Pietrak, K.; Wiśniewski, T.S. A review of models for effective thermal conductivity of composite materials. *Journal of Power Technologies* **2014**, 14-24%V 95.
220. Andersons, J.; Kirpluks, M.; Cabulis, P.; Kalnins, K.; Cabulis, U. Bio-based rigid high-density polyurethane foams as a structural thermal break material. *Construction and Building Materials* **2020**, *260*, 120471, doi:https://doi.org/10.1016/j.conbuildmat.2020.120471.

221. Smith, D.S.; Alzina, A.; Bourret, J.; Nait-Ali, B.; Pennec, F.; Tessier-Doyen, N.; Otsu, K.; Matsubara, H.; Elser, P.; Gonzenbach, U.T. Thermal conductivity of porous materials. *Journal of Materials Research* **2013**, *28*, 2260-2272, doi:10.1557/jmr.2013.179.
222. Obori, M.; Suh, D.; Yamasaki, S.; Kodama, T.; Saito, T.; Isogai, A.; Shiomi, J. Parametric Model to Analyze the Components of the Thermal Conductivity of a Cellulose-Nanofibril Aerogel. *Physical Review Applied* **2019**, *11*, 024044, doi:10.1103/PhysRevApplied.11.024044.
223. Dan, D.; Zhang, H.; Tao, W. Effective structure of aerogels and decomposed contributions of its thermal conductivity. *Applied Thermal Engineering* **2014**, *72*, 2-9.
224. Zeng, S.O.; Hunt, A.; Greif, R. Geometric structure and thermal conductivity of porous medium silica aerogel. *Journal of Heat Transfer* **1995**, Medium: X; Size: pp. 1055-1058.
225. Jia, Z.; Wang, Z.; Hwang, D.; Wang, L. Prediction of the Effective Thermal Conductivity of Hollow Sphere Foams. *ACS Applied Energy Materials* **2018**, *1*, 1146-1157, doi:10.1021/acsaem.7b00264.
226. Javier-Astete, R.; Jimenez-Davalos, J.; Zolla, G. Determination of hemicellulose, cellulose, holocellulose and lignin content using FTIR in Calycophyllum spruceanum (Benth.) K. Schum. and Guazuma crinita Lam. *PLOS ONE* **2021**, *16*, e0256559, doi:10.1371/journal.pone.0256559.
227. Beluns, S.; Platnieks, O.; Gaidukovs, S.; Starkova, O.; Sabalina, A.; Grase, L.; Thakur, V.K.; Gaidukova, G. Lignin and Xylan as interface engineering additives for improved environmental durability of sustainable cellulose nanopapers. *International Journal of Molecular Sciences* **2021**, *22*, doi:10.3390/ijms222312939.
228. Chen, Z.; Hu, T.Q.; Jang, H.F.; Grant, E. Modification of xylan in alkaline treated bleached hardwood kraft pulps as classified by attenuated total-internal-reflection (ATR) FTIR spectroscopy. *Carbohydrate Polymers* **2015**, *127*, 418-426, doi:https://doi.org/10.1016/j.carbpol.2015.03.084.
229. Derkacheva, O.; Sukhov, D. Investigation of Lignins by FTIR Spectroscopy. *Macromolecular Symposia* **2008**, *265*, 61-68, doi:https://doi.org/10.1002/masy.200850507.
230. Beluns, S.; Gaidukovs, S.; Platnieks, O.; Grase, L.; Gaidukova, G.; Thakur, V.K. Sustainable hemp-based bioplastics with tunable properties via reversible thermal crosslinking of cellulose. *International Journal of Biological Macromolecules* **2023**, *242*, 125055, doi:https://doi.org/10.1016/j.ijbiomac.2023.125055.
231. Ali, Z.M.; Gibson, L.J. The structure and mechanics of nanofibrillar cellulose foams. *Soft Matter* **2013**, *9*, 1580-1588, doi:10.1039/C2SM27197D.
232. Lavoine, N.; Bergström, L. Nanocellulose-based foams and aerogels: processing, properties, and applications. *Journal of Materials Chemistry A* **2017**, *5*, 16105-16117, doi:10.1039/c7ta02807e.
233. Liu, H.; Du, H.; Zheng, T.; Liu, K.; Ji, X.; Xu, T.; Zhang, X.; Si, C. Cellulose based composite foams and aerogels for advanced energy storage devices. *Chemical Engineering Journal* **2021**, *426*, 130817, doi:https://doi.org/10.1016/j.cej.2021.130817.
234. Sun, Y.; Chu, Y.; Wu, W.; Xiao, H. Nanocellulose-based lightweight porous materials: A review. *Carbohydrate Polymers* **2021**, *255*, 117489, doi:https://doi.org/10.1016/j.carbpol.2020.117489.
235. Wang, M.; Anoshkin, I.V.; Nasibulin, A.G.; Korhonen, J.T.; Seitsonen, J.; Pere, J.; Kauppinen, E.I.; Ras, R.H.A.; Ikkala, O. Modifying Native Nanocellulose Aerogels with Carbon Nanotubes for Mechanoresponsive Conductivity and Pressure Sensing.

Advanced Materials **2013**, *25*, 2428-2432, doi:https://doi.org/10.1002/adma.201300256.
236. Groult, S.; Budtova, T. Tuning structure and properties of pectin aerogels. *European Polymer Journal* **2018**, *108*, 250-261, doi:https://doi.org/10.1016/j.eurpolymj.2018.08.048.
237. Ferreira, E.S.; Rezende, C.A.; Cranston, E.D. Fundamentals of cellulose lightweight materials: bio-based assemblies with tailored properties. *Green Chemistry* **2021**, *23*, 3542-3568, doi:10.1039/D1GC00326G.
238. Schiavoni, S.; D'Alessandro, F.; Bianchi, F.; Asdrubali, F. Insulation materials for the building sector: A review and comparative analysis. *Renewable and Sustainable Energy Reviews* **2016**, *62*, 988-1011, doi:https://doi.org/10.1016/j.rser.2016.05.045.
239. Abu-Jdayil, B.; Mourad, A.-H.; Hittini, W.; Hassan, M.; Hameedi, S. Traditional, state-of-the-art and renewable thermal building insulation materials: An overview. *Construction and Building Materials* **2019**, *214*, 709-735, doi:https://doi.org/10.1016/j.conbuildmat.2019.04.102.
240. Kumar, D.; Alam, M.; Zou, P.X.W.; Sanjayan, J.G.; Memon, R.A. Comparative analysis of building insulation material properties and performance. *Renewable and Sustainable Energy Reviews* **2020**, *131*, 110038, doi:https://doi.org/10.1016/j.rser.2020.110038.

SUPPLEMENTARY

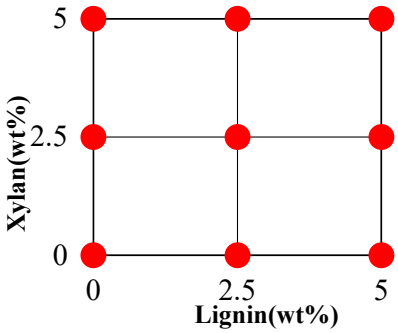

Full-factorial design (FFD) points

Design parameters and experimental results

Run	Design parameters		Responses		
	Lignin (wt%)	Xylan (wt%)	Specific modulus (MPa*cm^3/g)	Specific strength (MPa*cm^3/g)	Strain (%)
1	0	0	2471	60	2.9
2	0	2.5	4462	79	3.0
3	0	5	4122	74	2.4
4	2.5	0	4904	37	1.0
5	2.5	2.5	3283	49	1.6
6	2.5	5	1975	20	1.2
7	5	0	1900	18	1.1
8	5	2.5	2538	25	0.9
9	5	5	1684	25	1.6

The experimental data obtained in testing were used to construct the second-order polynomial regression equation using the program EdaOpt. Specific modulus, specific stress and strain were analyzed, and it is found that adjusted R2 values equal 0.565, 0.926, and 0.933, respectively. The relationships between the design variables $x_i = (X_1, X_2)$ and the corresponding behaviour functions Y_i are given as follows:

Specific modulus:

$$Y_{SM} = 3273+277\cdot X_1+555\cdot X_2-84\cdot X_1\cdot X_1-94\cdot X_2\cdot X_2-75\cdot X_1\cdot X_2, \quad (1)$$

Specific strength:

$$Y_{SS} = 64.63-18.19\cdot X_1+10.75\cdot X_2+1.83\cdot X_1\cdot X_1 -1.98\cdot X_2\cdot X_2-0.247\cdot X_1\cdot X_2, \quad (2)$$

Strain:

$$Y_S = 2.939-0.987\cdot X_1+0.02\cdot X_2+0.1147\cdot X_1\cdot X_1 -0.0213\cdot X_2\cdot X_2+0.04\cdot X_1\cdot X_2, \quad (3)$$

where X_1 and X_2 are the weight contents of the Lignin and Xylan, respectively.

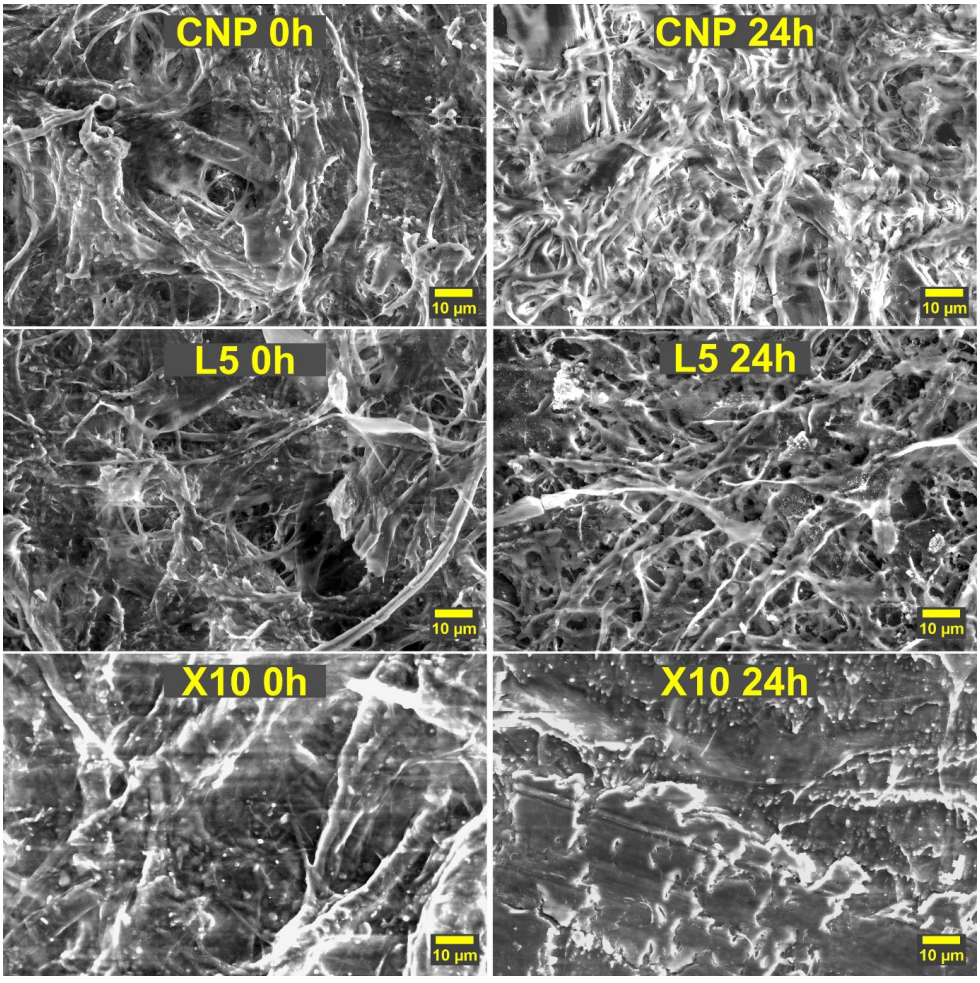

SEM micrographs showing the surface of selected NP compositions before and after UV aging, at a magnification of 1000x.

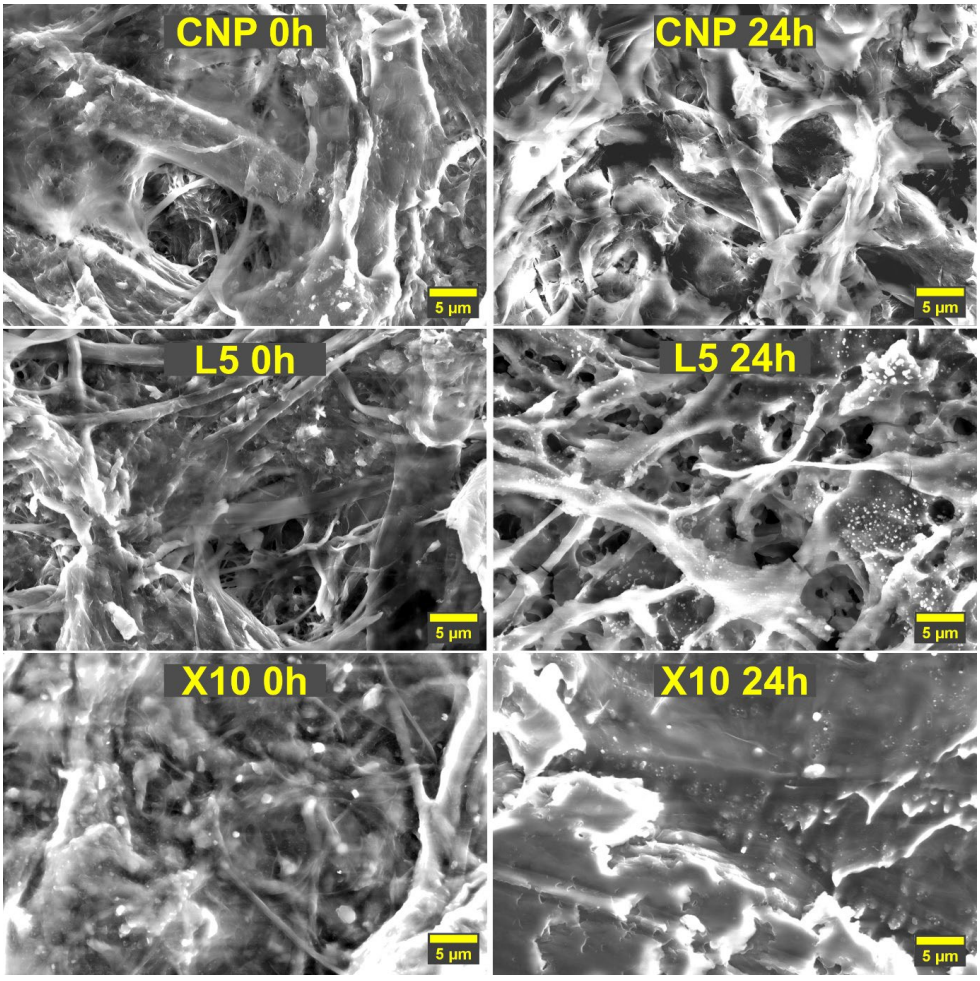

SEM micrographs showing the surface of selected NP compositions before and after UV aging, at a magnification of 2500x.

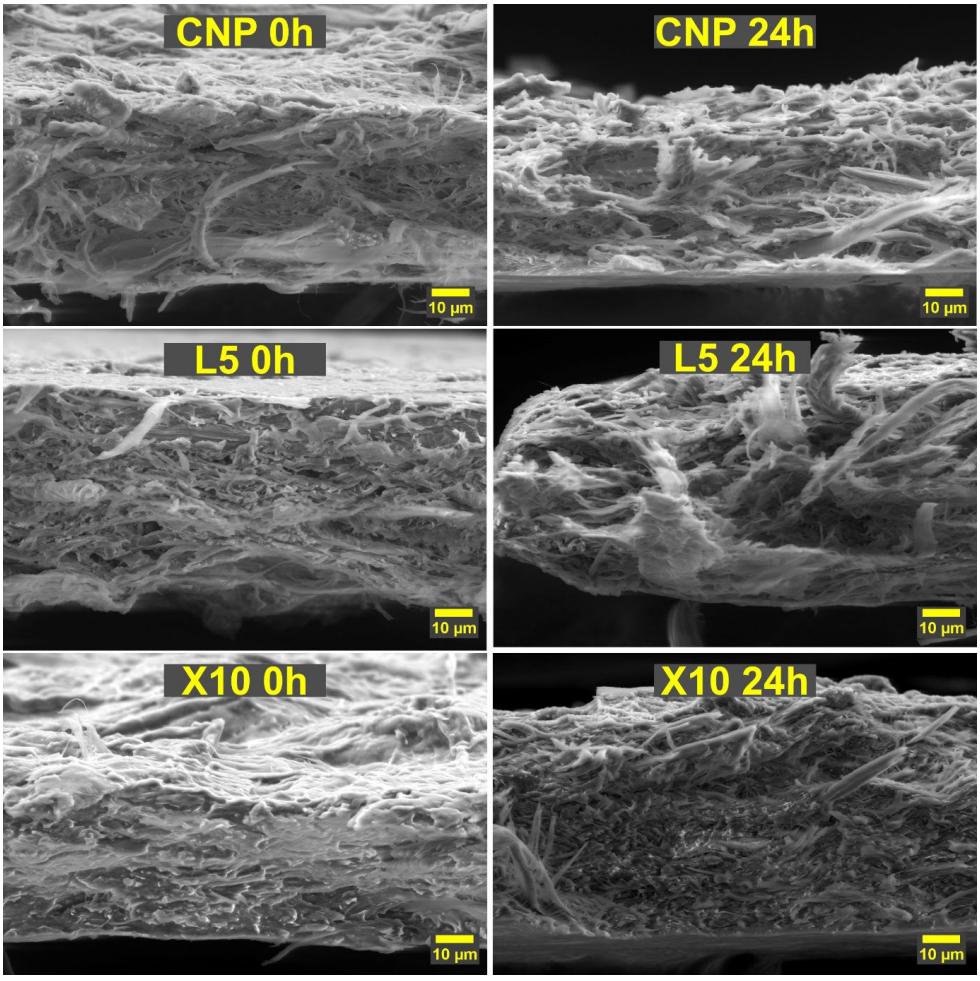

SEM micrographs showing the cross-section of selected NP compositions before and after UV aging, at a magnification of 1000x.

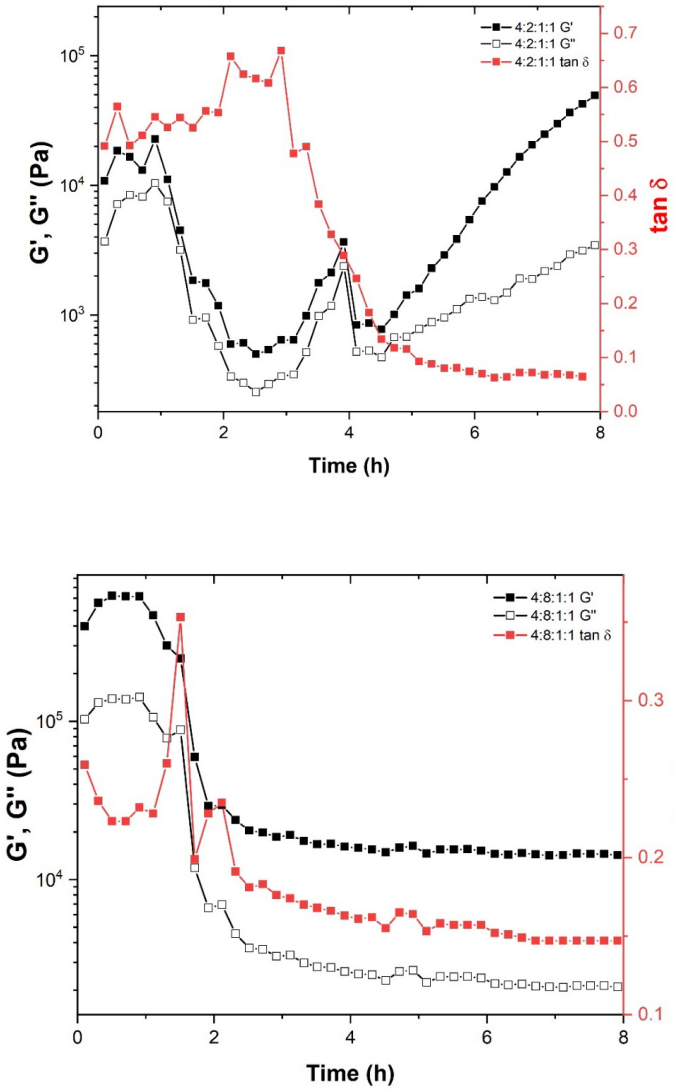

Rheological parameters G', G'', and tan δ for 4:2:1:1 and 4:8:1:1 impregnated mixtures

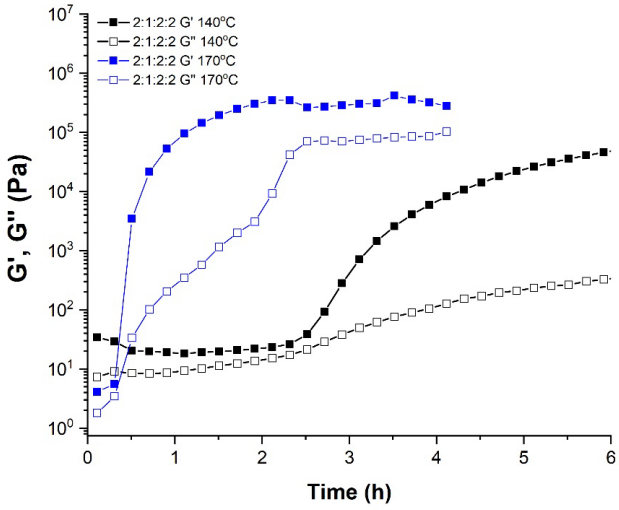

Rheological parameters G', G'' for 2:1:2:2 at 140 and 170 °C.

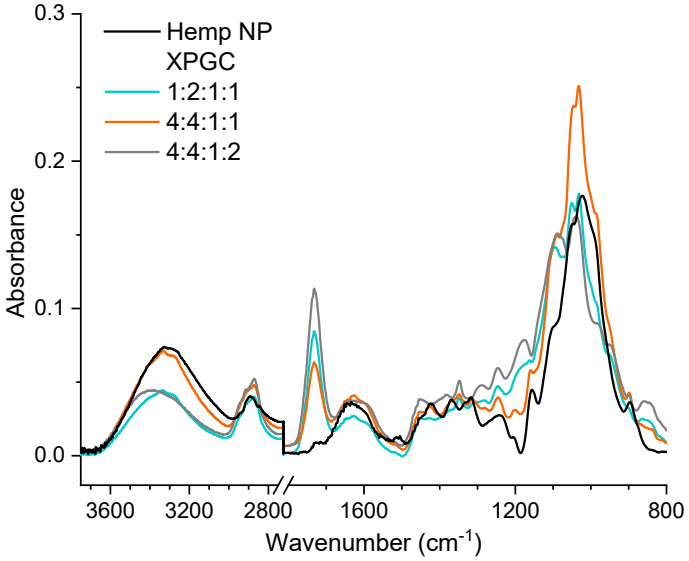

FTIR spectra of hemp paper and bioplastics: 1:2:1:1, 4:4:1:1, 4:4:1:2.

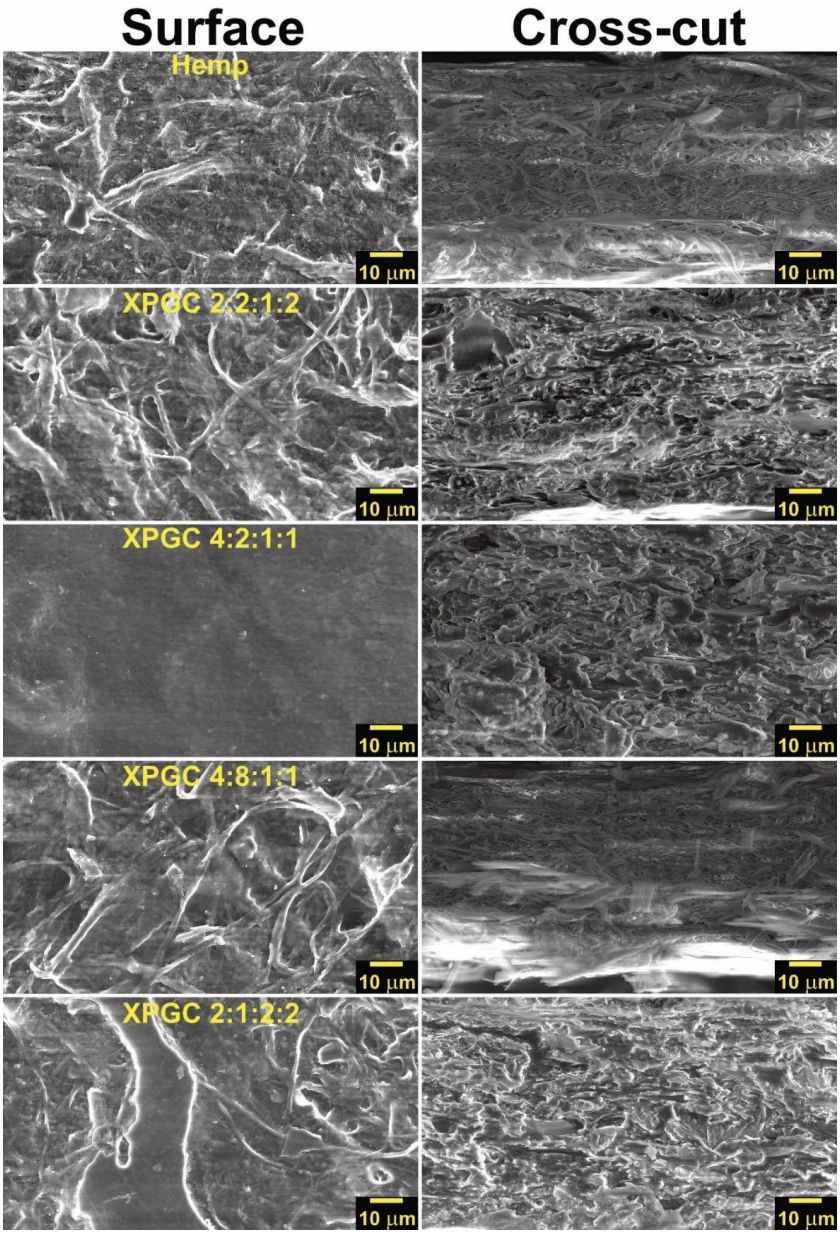

SEM surface and cross-cut micrographs of hemp paper and selected bioplastics shown at 1000x magnification.

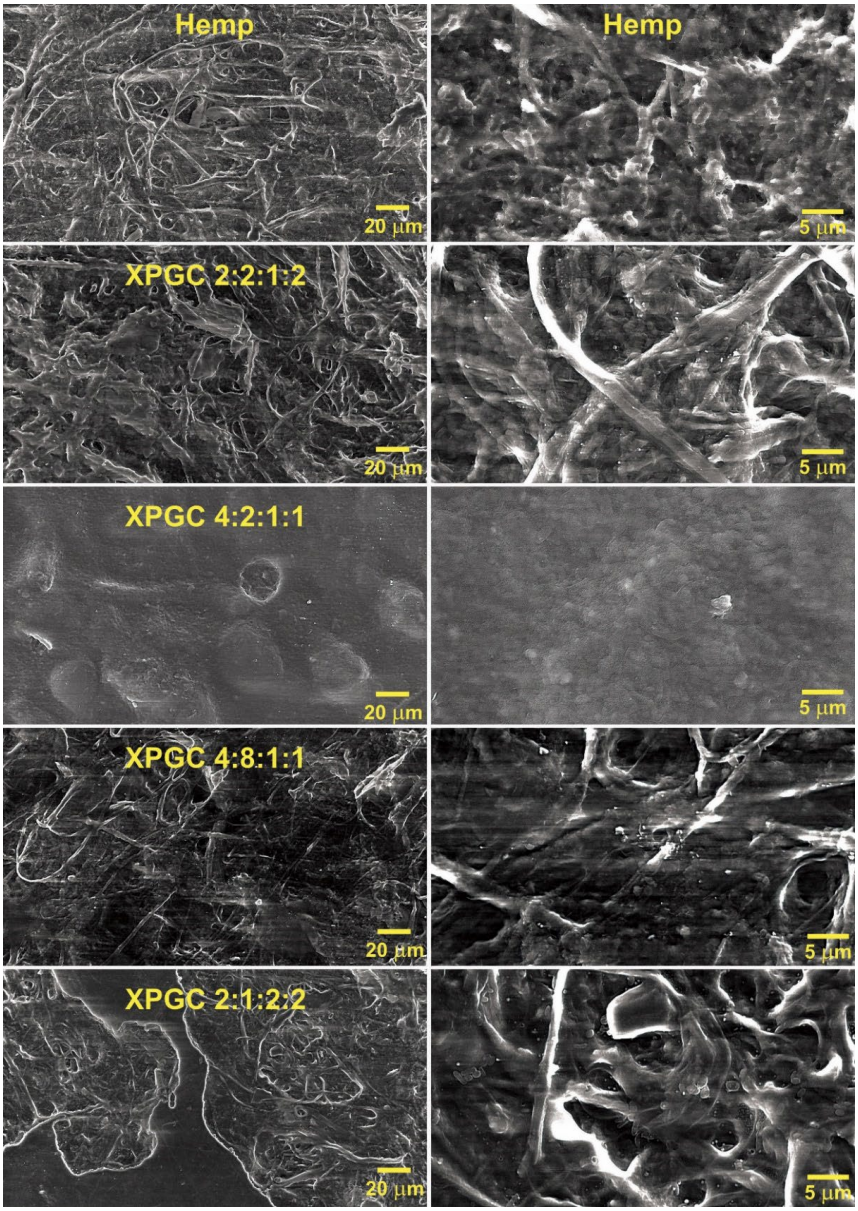

SEM micrographs of hemp paper and selected bioplastic surfaces shown at 500x and 2500x magnifications.

Summary of all prepared foam compositions and the quantities of each modifier

Sample	NFC susp. (g)	Xylan solution (g)	Lignin solution (g)	Pectin (g)	Glycerol (g)	CA (g)
Hemp	100	-	-	-	-	-
H-CA0.5	100	-	-	-	-	0.5
H-CA1	100	-	-	-	-	1
H-CA2.5	100	-	-	-	-	2.5
H-CA5	100	-	-	-	-	5
WM	100	11.8	32	-	-	-
WM-CA0.5	100	11.8	32	-	-	0.5
WM-CA1	100	11.8	32	-	-	1
WM-CA2.5	100	11.8	32	-	-	2.5
WM-CA5	100	11.8	32	-	-	5
H-P0.5-CA0.5	100	-	-	0.5	-	0.5
H-P0.25-CA1	100	-	-	0.25	-	1
H-P0.5-CA1	100	-	-	0.5	-	1
H-P1-CA1	100	-	-	1	-	1
WM-P0.25-CA1	100	11.8	32	0.25	-	1
WM-P0.5-CA1	100	11.8	32	0.5	-	1
WM-P1-CA1	100	11.8	32	1	-	1
H-G0.5-CA1	100	-	-	-	0.5	1
H-G1-CA1	100	-	-	-	1	1
H-G2-CA1	100	-	-	-	2	1
WM-G0.5-CA1	100	11.8	32	-	0.5	1
WM-G1-CA1	100	11.8	32	-	1	1
WM-G2-CA1	100	11.8	32	-	2	1
H-P0.5-G1-CA1	100	-	-	0.5	1	1
H-P0.5-G2-CA1	100	-	-	0.5	2	1
WM-P0.5-G1-CA1	100	11.8	32	0.5	1	1
WM-P0.5-G2-CA1	100	11.8	32	0.5	2	1

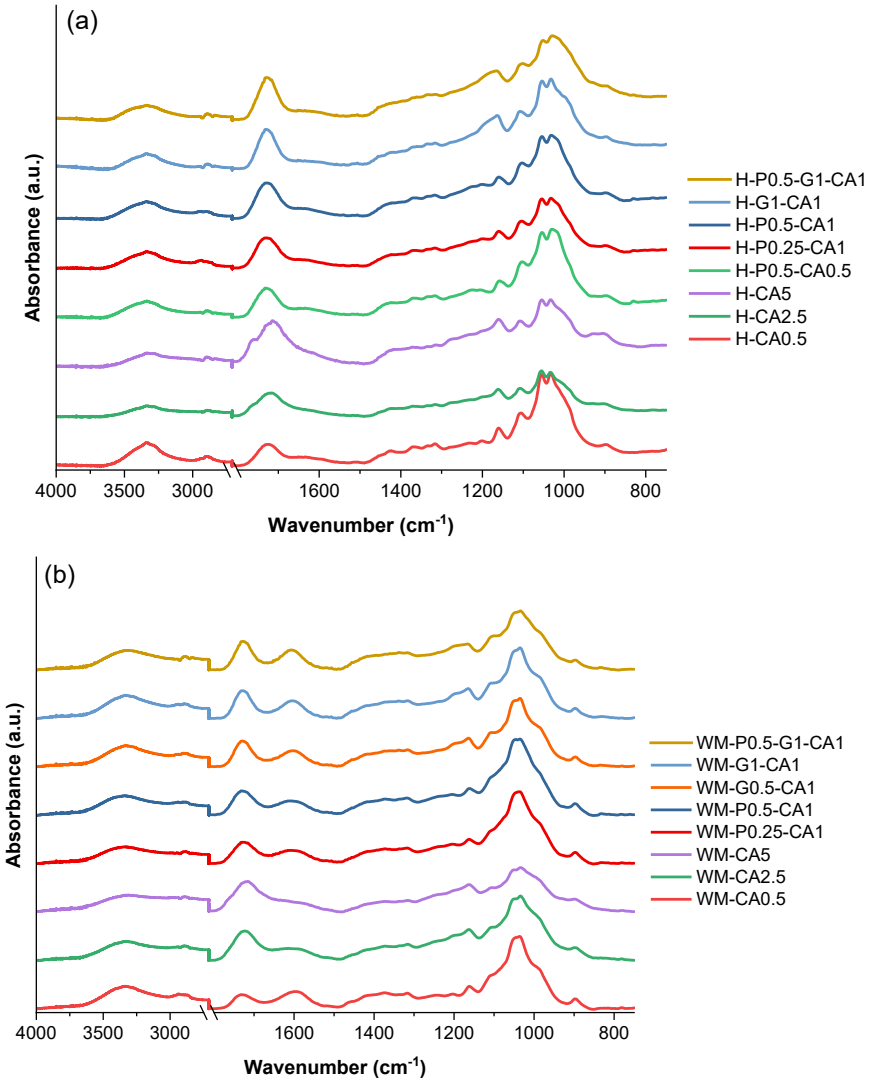

FTIR spectra of all remaining samples for (a) Hemp foams and (b) WM foams.

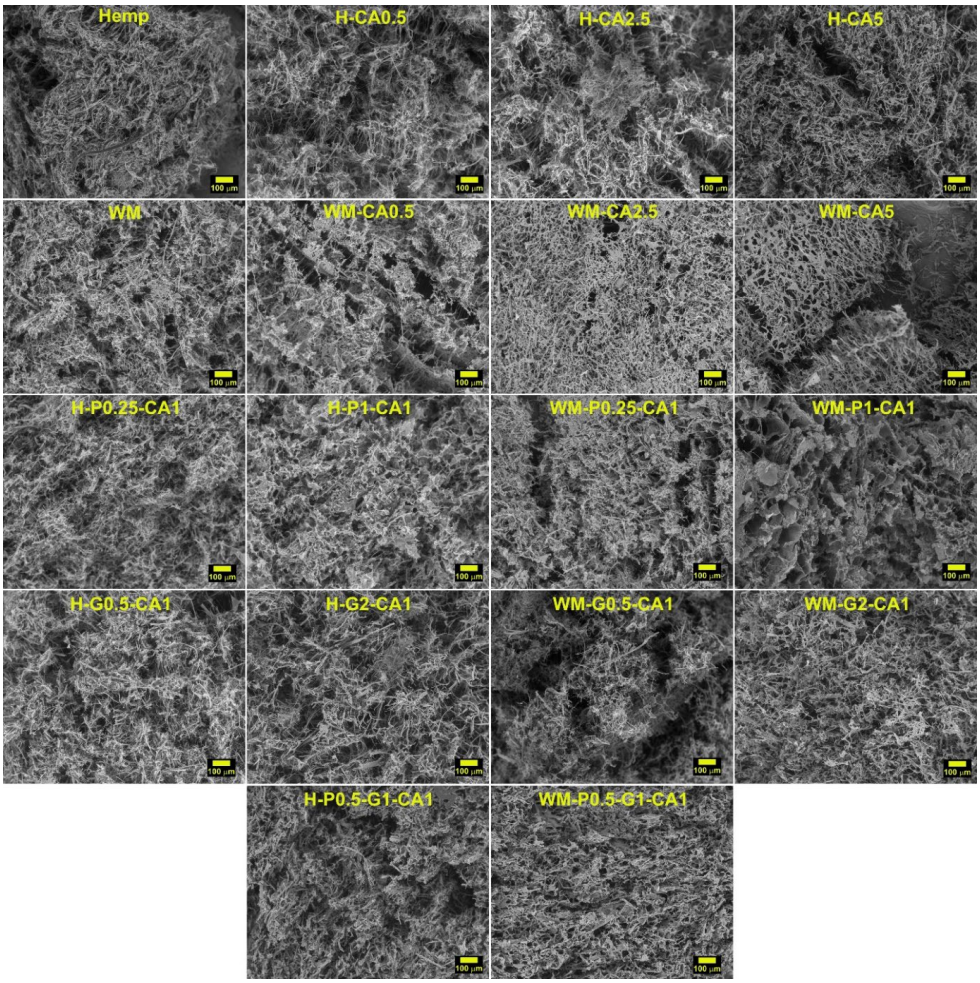

SEM micrographs of selected foam samples shown at 100x magnification.

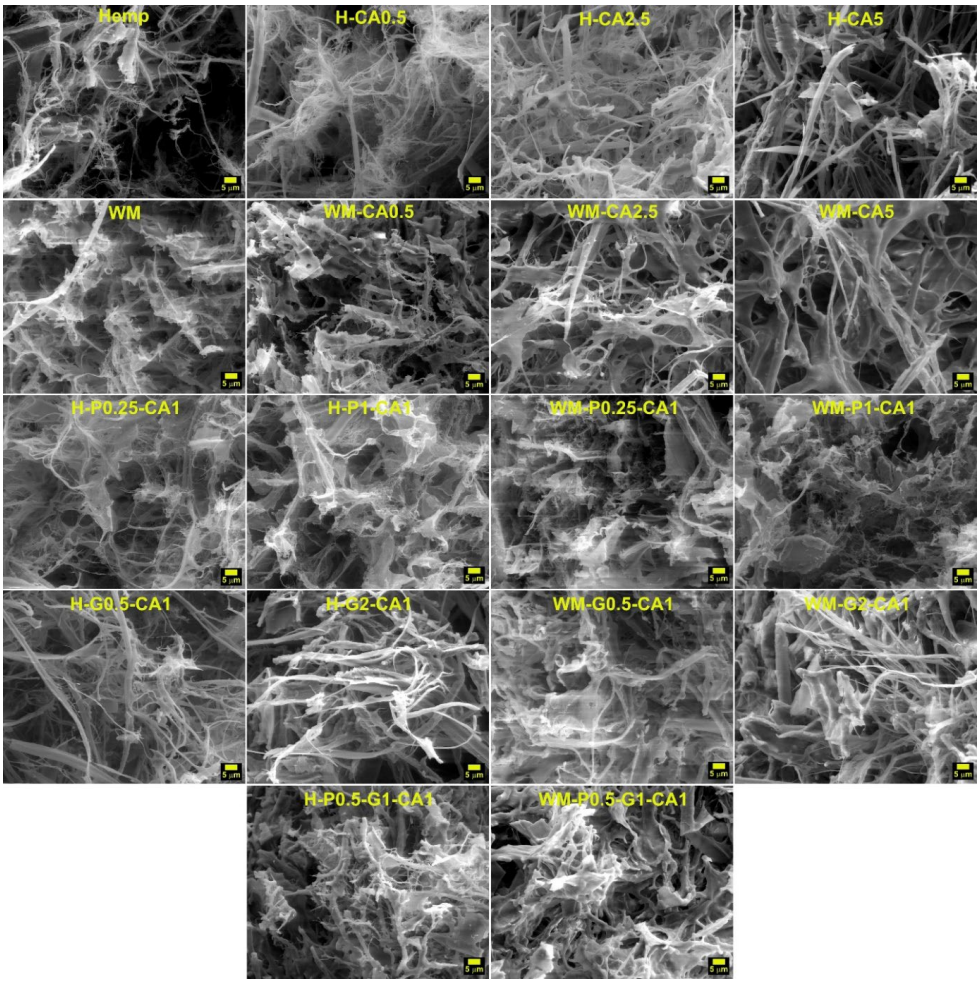

SEM micrographs of selected foam samples shown at 1000x magnification.

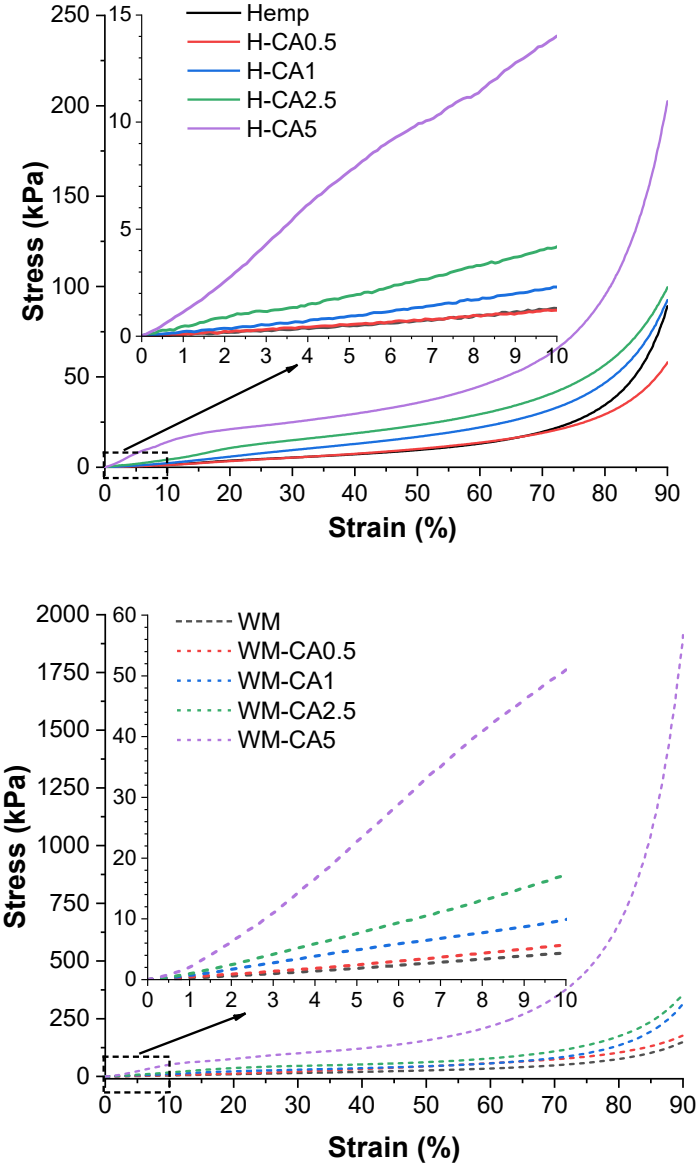

Compressive stress–strain curves of H- an WM- foams.

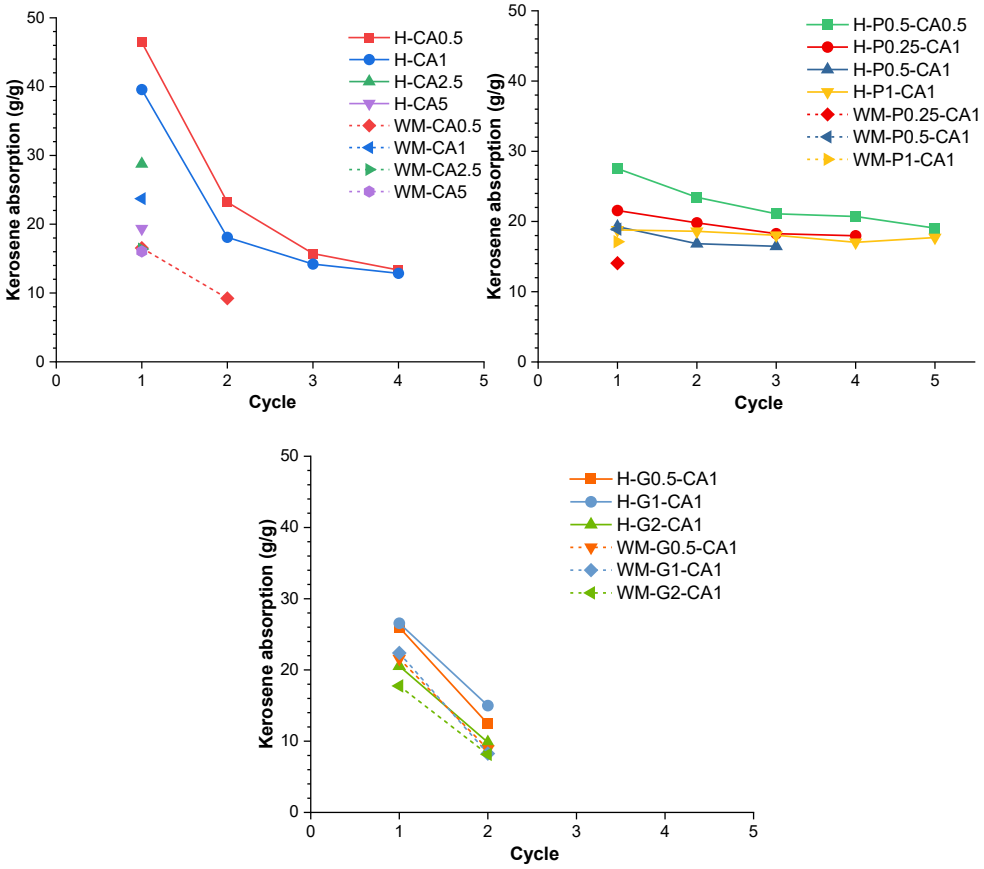

Foam recovery capabilities and cycle performance in kerosene.

Sergejs Beļuns was born in 1992 in Valmiera. He obtained a Bachelor's degree in Chemical Technology (2015) and a Master's degree in Materials Science (2017) from Riga Technical University (RTU). He was a technologist at "Polipaks" Ltd. Since 2020, he has been a scientific assistant and researcher at Riga Technical University. Currently, he is a researcher at the Institute of Chemistry and Chemical Technology. His scientific interests are related to the extraction and research of cellulosic bioplastics.